REPORT DOCUMENTATION PAGE

Form Approved OMB NO. 0704-0188

The public reporting burden for this collection of information is estimated to average 1 hour per response, including the time for reviewing instructions, searching existing data sources, gathering and maintaining the data needed, and completing and reviewing the collection of information. Send comments regarding this burden estimate or any other aspect of this collection of information, including suggesstions for reducing this burden, to Washington Headquarters Services, Directorate for Information Operations and Reports, 1215 Jefferson Davis Highway, Suite 1204, Arlington VA, 22202-4302. Respondents should be aware that notwithstanding any other provision of law, no person shall be subject to any oenalty for failing to comply with a collection of information if it does not display a currently valid OMB control number.
PLEASE DO NOT RETURN YOUR FORM TO THE ABOVE ADDRESS.

1. REPORT DATE (DD-MM-YYYY)	2. REPORT TYPE	3. DATES COVERED (From - To)
16-10-2015	Book Chapter	-

4. TITLE AND SUBTITLE
Principles of THz Generation, Chapter 2 in "Semiconductor Terahertz Technology: Devices and Systems at Room-Temperature Operation"

5a. CONTRACT NUMBER
W911NF-12-1-0496

5b. GRANT NUMBER

5c. PROGRAM ELEMENT NUMBER
611102

6. AUTHORS
Sascha Preu, Gottfried H. Dohler, Stefan Malzer, Andreas Stohr, Vitaly Rymanov, Thorsten Gobel, Elliott R. Brown, Michael Feiginov, Ramon Gonzalo, Miguel Beruete, and Miguel Navarro-Cia

5d. PROJECT NUMBER

5e. TASK NUMBER

5f. WORK UNIT NUMBER

7. PERFORMING ORGANIZATION NAMES AND ADDRESSES
Wright State University
Wright State University
3640 Colonel Glenn Highway
Dayton, OH 45435 -0001

8. PERFORMING ORGANIZATION REPORT NUMBER

9. SPONSORING/MONITORING AGENCY NAME(S) AND ADDRESS (ES)
U.S. Army Research Office
P.O. Box 12211
Research Triangle Park, NC 27709-2211

10. SPONSOR/MONITOR'S ACRONYM(S)
ARO

11. SPONSOR/MONITOR'S REPORT NUMBER(S)
62602-EL.30

12. DISTRIBUTION AVAILIBILITY STATEMENT
Approved for public release; distribution is unlimited.

13. SUPPLEMENTARY NOTES
The views, opinions and/or findings contained in this report are those of the author(s) and should not contrued as an official Department of the Army position, policy or decision, unless so designated by other documentation.

14. ABSTRACT
The THz frequency range (100 GHz-10 THz) is situated between microwaves and infrared optics. For a long time, it was called the “THz gap”, since there were no efficient sources and detectors available in contrast to the neighbouring microwave and optical domains. In the mean time, a multitude of means to generate THz radiation has been developed in order to close this gap. For highest THz power levels, i.e. tens of Watt level average power and tens of J level pulse energies, factory hall sized free electron lasers and synchrotrons have been constructed. A heavily

15. SUBJECT TERMS
ultrafast photoconductive devices, photoconductive switches, photomixers, pin-diode, UTC pin diode, GaAs, InGaAs, erbium doping

16. SECURITY CLASSIFICATION OF: a. REPORT	b. ABSTRACT	c. THIS PAGE	17. LIMITATION OF ABSTRACT	15. NUMBER OF PAGES	19a. NAME OF RESPONSIBLE PERSON
UU	UU	UU	UU		Elliott Brown
					19b. TELEPHONE NUMBER 937-775-4903

Standard Form 298 (Rev 8/98)
Prescribed by ANSI Std. Z39.18

Report Title

Principles of THz Generation, Chapter 2 in "Semiconductor Terahertz Technology: Devices and Systems at Room-Temperature Operation"

ABSTRACT

The THz frequency range (100 GHz-10 THz) is situated between microwaves and infrared optics. For a long time, it was called the “THz gap”, since there were no efficient sources and detectors available in contrast to the neighbouring microwave and optical domains. In the mean time, a multitude of means to generate THz radiation has been developed in order to close this gap. For highest THz power levels, i.e. tens of Watt level average power and tens of J level pulse energies, factory hall sized free electron lasers and synchrotrons have been constructed. A heavily accelerated, relativistic electron beam is guided into an undulator, a structure where the electron is deflected back and forth by alternating magnetic fields. The acceleration of the relativistic electrons perpendicular to their main direction of propagation results in dipole radiation along the propagation axis. In free electron lasers, the undulator is usually situated inside a THz cavity, The cavity field acts back on the electron beam, resulting in microbunching, i.e. dicing the electron beam into packets. Constructive interference of all electron packets occurs, resulting in a laser-like behaviour.

Chapter 2

Principles of THz Generation

S. Preu[1], G.H. Döhler[1], S. Malzer[1], A.Stöhr[2], T.Göbel[3], E. R. Brown[4], M. Feiginov[5], R. Gonzalo[6],M. Beruete[6], M. Navarro-Cía[6]

[1]Friedrich-Alexander Erlangen-Nürnberg University, Erlangen, Germany
[2]Duisburg University , Duisburg, Germany
[3]Heinrich Hertz Institute, Berlin, Germany
[4]Wright State University, Dayton, Ohio, USA
[5]Tokyo Institute of Technology, Japan
[6]Universidad Pública de Navarra, Navarra, Spain

to appear in *Semiconductor Terahertz Technology: Devices and Systems for Room Temperature Operation,* ed. by G. Carpintero, L.E. Garcia Munoz, H.H. Hartnagel, and S. Preu (John Wiley & Sons, Ltd., Chichester, PO19 8SQ, England)

2.1. Overview

The THz frequency range (100 GHz-10 THz) is situated between microwaves and infrared optics. For a long time, it was called the “THz gap”, since there were no efficient sources and detectors available in contrast to the neighbouring microwave and optical domains. In the mean time, a multitude of means to generate THz radiation has been developed in order to close this gap. For highest THz power levels, i.e. tens of Watt level average power and tens of μJ level pulse energies [1]-[3], factory hall sized free electron lasers and synchrotrons have been constructed. A heavily accelerated, relativistic electron beam is guided into an undulator, a structure where the electron is deflected back and forth by alternating magnetic fields. The acceleration of the relativistic electrons perpendicular to their main direction of propagation results in dipole radiation along the propagation axis. In free electron lasers, the undulator is usually situated inside a THz cavity [4],[5]. The cavity field acts back on the electron beam, resulting in microbunching, i.e. dicing the electron beam into packets. Constructive interference of all electron packets occurs, resulting in a laser-like behaviour.

Another source is the backward wave oscillator (BWO). It could be considered as the small brother of a synchrotron. It consists of a vacuum tube that houses an electron source, a Wien filter and a slow wave circuit (instead of an undulator). At resonance, a wave is built up in the slow wave circuit that propagates in the opposite direction of the electron beam, hence the name “backward wave” oscillator. In contrast to FELs, BWOs are table top sources. They provide power levels in the ange of mW (at 1 THz) to 100 mW (at ~100 GHz) [6].

True THz lasers are gas lasers, p-Germanium (p-Ge) lasers and quantum cascade lasers. Gas lasers use polar molecules as laser medium. The rotation spectra of basically all polar molecules (methanol, e.g.) are situated in the THz range and therefore suited as THz laser levels. The gas cell, set up within a THz cavity, is usually pumped with an infra-red laser, in most cases a CO_2 laser [7].

Only the THz wavelength that is in resonance with the cavity is amplified. Average power levels in the mW range can easily be achieved with record continuous-wave (CW) levels above 1 W [8]. However, the frequency is limited to the molecule-specific resonance frequencies. The p-Ge laser consists of p-type Germanium mounted in a crossed E and B-field. The laser transistions are either transitions from light to heavy hole valence subbands or transitions between cyclotron resonances [9],[10]. The laser cavity is the crystal itself or an external cavity [11]. So far, p-Ge lasers have to be operated in a cryogenic environment. Quantum cascade lasers (QCL) consist of a superlattice of quantum wells which is electrically biased [12]. Each superlattice period consists of several quantum wells of different width and barrier thickness. The upper and lower laser levels are extended over several suitably designed wells. Strong coupling through a narrow barrier allows for filling the upper laser level. In order to achieve population inversion, fast depletion of the lower level is ensured by resonant LO phonon assisted transitions to lower states and strong coupling to the neighboring “ground state” through a narrow barrier. This ground state represents the injector for the next period of the “quantum cascade” structure, which comprises of the order of $N \approx 100$ periods. Ideally, a single electron produces a THz photon for each sequence in the cascade. As the *spontaneous* radiative transitions between upper and lower laser level are competing with by orders of magnitude more efficient non-radiating phonon-assisted transitions, the dark current density in QCLs is high. With sophisticated design, it has become possible to achieve very high THz photon densities in high-Q laser cavities, such that ultimately the stimulated laser transitions largely outnumber the nonradiative processes. Although the threshold currents are high, the quantum efficiency above threshold becomes high and CW power levels in the tens of mW are available in the upper part of the THz range [13]. However, the tunability is limited by the linewidth of the THz resonator (usually the QCL chip itself), and it is very challenging to operate a QCL below 1 THz [14]. Both p-Ge lasers and QCLs require cryogenic operation. This often hinders commercial applications.

Another very important optical method of THz generation is non-linear frequency conversion [15]. Many materials show non-linear components of the electric susceptibility, χ. The polarization, *P(t)*, of a crystal caused by incident light with field strength *E(t)* is given by

$$P(t) = \varepsilon_0 \left(\chi^{(1)} E(t) + \chi^{(2)} (E(t))^2 + \chi^{(3)} (E(t))^3 + \ldots \right), \qquad (2.1)$$

where *E(t)* is the sum of all incident electric fields. The order of magnitude of the *non-linear* components (i.e. $\chi^{(n)}$ with n>1) strongly depends on the crystallographic structure of the material. For THz generation, the second order non-linearity, $\chi^{(2)}$, is most commonly used. For two incident lasers that slightly differ in frequency, this term contains a component of the difference frequency. *P(t)* then oscillates and emits photons at the difference frequency that can easily be chosen to be in the THz range. Since $P^{(2)}(t) \sim (E(t))^2$, high fields are required for efficient generation. Therefore, mostly pulsed laser sources are used, with a few CW examples also demonstrated. It also works for a single to few THz cycle pulses, since the pulses contain a broad frequency spectrum. The optical laser signal and the THz signal have to co-propagate through some length, $l \sim 0.5$ mm, of the non-linear crystal. The THz refractive index and the optical refractive index have to be matched in order to assure propagation at the same speed of light (“phase-matching”). Due to the Manley-Rowe criterion (simply speaking, one pair of optical photons can only generate one THz photon), $\chi^{(2)}$ THz generation is very inefficient the further the THz frequency and the optical frequencies are apart (if secondary photons are recycled, however, efficiencies above the Manley-Rowe limit are possible). Typical power efficiency values for THz generation with NIR lasers are in the range of 10^{-5} [15]. However, high available power of state of the art pulsed laser systems, high THz peak power (50 kW in ref. [16]), the large frequency coverage, and room temperature operation make non-linear THz generation very attractive for a large share of applications.

A detailed description of all these approaches is beyond the scope of this book. This chapter will therefore focus only on THz generation by photomixing and by electronic means.

Much alike non-linear THz generation, photomixers down-convert optical photons to THz photons. In contrast to polarization of a crystal, where a pair of optical photons generates *one THz photon*, a pair of optical photons generates *one electron-hole pair* in a semiconductor. Each electron-hole pair can emit *many THz photons*. Therefore, THz generation via photogeneated electron hole pairs is typically much more efficient than non-linear generation, particularly at the lower end of the THz spectrum. This approach works well at room temperature and under ambient conditions, and offers an extremely large tuning range. These sources can be operated with a single few cycle pulsed laser (broadband operation), two pulsed lasers with pulse widths much longer than the inverse THz frequency (quasi-continuous-wave operation), and in the continuous-wave (CW) mode (requiring two CW lasers). They are very versatile and are used in a manifold of applications. In this chapter, we will develop the theoretical framework, the limitations, and provide various realizations of photomixers.

In the second part of this chapter, we will discuss the fundamentals of electronic generation of THz radiation in Section 2.5. This includes electronic high frequency oscillators such as negative resistance devices (resonant tunnelling diodes, and Esaki diodes) and electronic up-conversion of microwave radiation to the THz domain using Schottky diodes and hetero-barrier varactors. Since microwave circuits offer high power levels and high efficiencies, electronic THz generation is very successful and offers a large amount of applications. Such applications range from astronomic applications on satellites to table-top applications in the laboratory.

2.2. THz Generation by Photomixers and Photoconductors

2.2.1. Principle of Operation

For simplicity, we start with continuous-wave (CW) or quasi-continuous-wave photomixing. The formalisms are simpler to understand since all equations have to be derived for a single THz frequency only. However, most results will be valid and applicable for pulsed operation as well. A photomixer consists of a semiconductor that is excited with a pair of lasers with powers P_1 and P_2, and frequencies $\upsilon_{1,2} = \bar{\upsilon} \pm \upsilon_{THz}/2$, i.e. they differ in frequency by the THz frequency. The frequency of the lasers must be sufficiently high in order to generate electron-hole pairs in the semiconductor by absorption, that is $\upsilon_{1,2} > E_G / h$, where E_G is the band gap energy of the semiconductor (E_G = 1.42 eV for GaAs, e.g.) and h is the Planck constant. The lasers with electric field strengths $E_{1,0} \sim \sqrt{P_1}$ and $E_{2,0} \sim \sqrt{P_2}$, are heterodyned, resulting in a total optical field strength of

$$\vec{E}(t) = \vec{E}_1(t) + \vec{E}_2(t) = \vec{E}_{1,0} e^{i(\bar{\omega}+\omega_{THz}/2)t} + \vec{E}_{2,0} e^{i(\bar{\omega}-\omega_{THz}/2)t - i\varphi}, \qquad (2.2)$$

where $\omega_i=2\pi\nu_i$ are angular frequencies, and φ is the relative phase. The optical intensity is

$$I_L(t) \sim \left|\vec{E}(t)\right|^2 = E_{1,0}^2 + E_{2,0}^2 + 2\left|\vec{E}_{1,0} \circ \vec{E}_{2,0}\right| \cos(\omega_{THz} t + \varphi), \qquad (2.3)$$

as illustrated in *Fig.2.1 a* and *b*. Expressing eq. (2.3) in terms of power yields

$$P_L(t) = P_1 + P_2 + 2\sqrt{P_1 P_2}\cos\beta \cdot \cos(\omega_{THz} t + \varphi), \qquad (2.4)$$

where β is the angle between the electric fields (polarizations) of the lasers. An *ideal* semiconductor device (i.e. all light is absorbed, no losses) will generate a photocurrent

$$I_{Ph}^{id}(t) = \frac{eP_L(t)}{h\overline{\upsilon}} = \frac{e(P_1 + P_2)}{h\overline{\upsilon}} + 2\frac{e\sqrt{P_1 P_2}}{h\overline{\upsilon}}\cos\beta \cdot \cos(\omega_{THz} t + \varphi), \qquad (2.5)$$

with a DC component of $I_{DC}^{id} = e(P_1 + P_2)/h\overline{\upsilon}$ and an AC amplitude of $I_{THz}^{id} = 2e\sqrt{P_1 P_2}\cos\beta / h\overline{\upsilon}$. The AC current is maximized for $P_1=P_2=P_L=1/2P_{tot}$ and

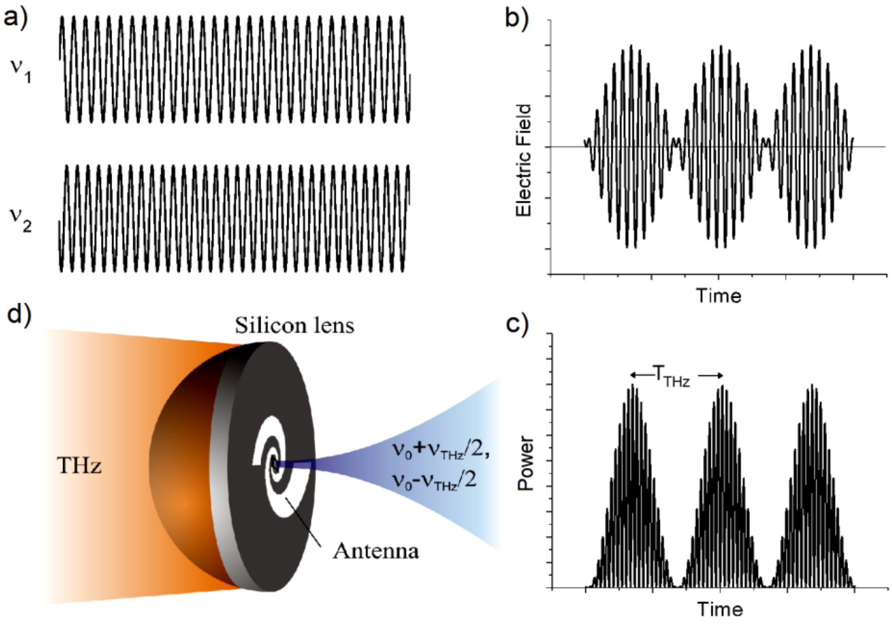

Fig.2.1: Schematic of the photomixing process. a) Two lasers are heterodyned; b) Resulting electric field. c) Resulting power modulation with a beat node at the difference frequency; d) The heterodyned lasers are focused on a photomixer. It is connected to an antenna to radiate the THz signal. A silicon lens assists to couple out the THz beam to free space.

$\beta=0$, i.e. the two lasers have identical power and polarization, yielding $I_{THz}^{id} = eP_{tot}/h\overline{\upsilon} = I_{DC}^{id} = I^{id}$, where $P_{tot}=2P_L$ is the total laser power. The total current reads

$$I_{Ph}^{id}(t) = I^{id}[1 + \cos(\omega_{THz} t + \varphi)]. \qquad (2.6)$$

The AC current is usually fed into some kind of antenna with radiation resistance R_A and an (ideal) THz power of

$$P_{THz} = \frac{1}{2} R_A \left(I_{THz}^{id}\right)^2 = \frac{1}{2} R_A \left(\frac{e}{h\overline{\upsilon}}\right)^2 P_{tot}^2 \qquad (2.7)$$

is radiated.

To summarize, two lasers beams that differ in frequency by the THz frequency are absorbed by a semiconductor device. The device produces an AC current at the difference frequency of the lasers, namely the THz frequency. This current is fed into an antenna for THz emission. On a first glance, this seems to be a complicated scheme. However, the photomixing concept has several outstanding advantages:

- It is very simple to tune a laser by 1 THz (see Chapter 7 for details). For 1550 nm (800 nm) lasers, this corresponds to a wavelength offset of 8 nm (2.2 nm). Most lasers are tunable by several nm to tens of nm, so photomixers are inherently tunable over an extremely wide range. This is particularly important for spectroscopic applications.
- The linewidth of the THz radiation from a CW photomixer is determined by the linewidth of the lasers. Typical values are a few MHz to a few tens of MHz. This is sufficient for most applications. Long cavity lasers can offer linewidths in the 100 kHz range. For obtaining even narrower linewidths, it is also possible to stabilize the lasers [17].
- The interaction length of the laser beam with the semiconductor is short compared to the THz wavelength. In contrast to non-linear mixing, there are no phase matching problems.
- Most importantly, photomixers can be operated at room temperature, but are not limited to that.

For pulsed operation, the device absorbs a single, short optical pulse. By using some kind of radiating structure, such as an antenna, the photocurrent yields THz radiation. The emitted THz field is proportional to the *first time derivative* of the photocurrent,

$$E_{THz}(t) \sim \frac{\partial I_{Ph}(t)}{\partial t} \tag{2.8}$$

In order to obtain the frequency spectrum of the emitted signal, the THz field has to be Fourier transformed, yielding

$$E_{THz}(\omega) \sim FT\left[\frac{\partial I_{Ph}(t)}{\partial t}\right] = i\omega I_{Ph}(\omega), \tag{2.9}$$

where $I_{Ph}(\omega)$ is the spectrum of the photocurrent. In the ideal case, the photocurrent spectrum is proportional to the optical pulse spectrum. According to the Fourier theorem, the spectral width, $\Delta\omega$, is inversely proportional to the temporal width (current pulse duration), $\Delta\tau$, i.e. $\Delta\omega\Delta\tau = 0.5$. Therefore, the optical pulse duration must be (much) shorter than the period of the maximum THz frequency to be obtained. In contrast to the CW case, the relation between photocurrent and optical power is more complicated: The photocurrent density at time t of a carrier density generated at time t' is given by $j_{Ph}(t,t') = en(t')\mathrm{v}(t-t')$, with the carrier velocity $\mathrm{v}(t-t')$. When an optical photon is absorbed close to the band edge, it generates an electron-hole pair that is at rest. The carriers are subsequently accelerated for instance by an applied DC bias. Thus, not only the carrier concentration (generation rate $\partial n(t)/\partial t \sim P_L(t)$) but also the carrier velocity is time dependent. The THz pulse is thus temporally broader than the optical pulse and depends on the details of the carrier transport in the semiconductor. These broadening mechanisms will be discussed in the next section.

2.2.2 Basic Concepts and Design Rules

There exist two kinds of photomixers: *p-i-n* diode based mixers and *photoconductive* mixers. In order to develop the limiting factors of photomixers at high THz frequencies, we will start with p-i-n diodes and discuss photoconductive mixers subsequently.

2.2.2.1 P-i-n diode based photomixers

At DC and at low and intermediate RF frequencies, p-i-n diodes are implemented to generate photocurrent from incident light. For instance, p-i-n diodes are used in solar cells and also as receivers in communication electronics, where they act as optical to RF converters. A p-i-n diode consists of a p-doped semiconductor, followed by an intrinsic (undoped) part (i) and an n-doped semiconductor. For moderately n/p-doped samples, an electric field of strength $E_i = E_G / d_i$ builds up in the intrinsic layer of length d_i, where E_G is the band gap of the semiconductor. Electron-hole pairs generated in the i-region are efficiently separated by the built-in field. In order to suppress slow contributions due to diffusion of photogenerated electrons, from the field-free p-layer into the i-layer and the corresponding contributions due to holes generated in the field-free n-layer, the band gap of the doping layers is increased to energies exceeding the photon energy, by adding aluminum to GaAs or to $In_{0.53}Ga_{0.47}As$, e.g.. These "double-hetero" (DH) p-i-n diodes with carrier generation restricted to the i-region (see Fig. 2.1) can also be used at THz frequencies. Although each absorbed photon fully contributes an elementary charge e to the photocurrent, there are several mechanisms that limit the efficiency of the device. First, the semiconductor surface will reflect some of the laser power. This reflection (R) can be minimized by an anti-reflection coating. Second, not all optical power is absorbed within the i-layer. A real device has a finite absorption length (typically 1 µm) for an absorption coefficient α in the range of 10^4 cm^{-1}. In particular, typical materials used for 800 nm (GaAs) and 1550 nm ($In_{0.53}Ga_{0.47}As$), exhibit an absorbance $A = 1 - \exp(-\alpha d_i) = 67\%\ (55\%)$ for a 1 µm absorption length and an absorption coefficient (close to the band edge) of 1.1x10^4 cm^{-1} (0.8x10^4 cm^{-1}) . The

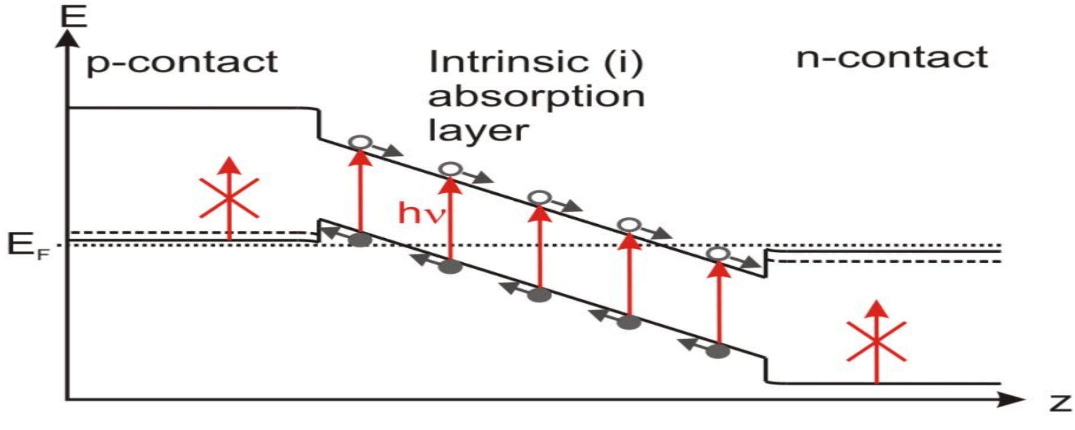

Fig. 2.2: Double hetero p-i-n diode structure as used in RF electronics or solar cells. The vertical arrows indicate the photon energy, hν. Optically generated holes move towards the p-contact, electrons to the n-contact. Due to the larger band gap, absorption in the contact layers is not possible.

reduction of both the AC and DC photocurrent with respect to the ideal photocurrent is summarized in the external quantum efficiency,

$$\eta_{ext}^{I} = (1-R)\cdot[1-\exp(-\alpha d_i)]\,. \tag{2.10}$$

Since the THz power is proportional to the square of the photocurrent, the external THz quantum efficiency is

$$\eta_{ext} = (1-R)^2\cdot[1-\exp(-\alpha d_i)]^2\,. \tag{2.11}$$

At high frequencies, two further effects reduce the AC current amplitude: Any electronic device has a certain capacitance. In the case of a p-i-n diode, the capacitance is simply that of a plate capacitor with a plate spacing of d_i, the intrinsic layer thickness:

$$C_{pin} = \varepsilon_0\varepsilon_r\frac{A}{d_i}\,, \tag{2.12}$$

where A is the cross section of the diode. This capacitance is parallel to the radiation resistance, R_A, of the antenna as illustrated in Fig. 2.3. At high frequencies, the antenna is shorted by the capacitance, reducing the power delivered to the antenna according to

$$\eta_{RC} = \frac{1}{1+(2\pi R_A C_{pin}\upsilon_{THz})^2}\,. \tag{2.13}$$

This roll-off is called the ***RC roll-off***. At high frequencies, the THz power decreases as υ^{-2}, the 3 dB frequency (i.e. the frequency where the THz power is reduced by a factor of two) is $\upsilon_{3dB}^{RC} = (2\pi R_A C_{pin})^{-1}$.

Another roll-off is attributed to the carrier transport inside the diode. Carriers that are generated at different times cause displacement currents while being transported to the respective n- or p-contact. These currents interfere. We will discuss two extreme cases

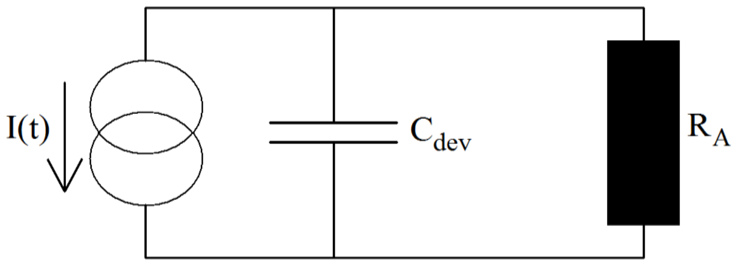

Fig. 2.3: Simplified equivalent circuit of a THz emitter. The device capacitance, C_{dev}=C_{pin} is parallel to the radiation resistance of the antenna, R_A. Real devices may further feature a finite conductance parallel to the current source.

of diodes, namely a diode with a strongly confined absorption region and a diode with homogeneous absorption along the intrinsic layer. For a diode where a narrow absorption region is confined close to the p-contact, hole contributions are negligible since they remain stationary, and only electrons are transported. For simplicity, we assume for now that electrons are instantaneously accelerated to the saturation velocity, v_{sat}, and then transported at that constant velocity. This is a reasonable approximation for diodes operated at high transport fields. More realistic cases will be treated later. The displacement current is

$$I(t) = \frac{1}{\tau_{tr}}\int_0^{\tau_{tr}} I(t,\tau')d\tau'\,, \tag{2.14}$$

where $\tau_{tr} = v_{sat}/d_i$ is the transport time of the carriers and $I(t,\tau') = I^{id}\{\cos[\omega(t-\tau')]+1\}$ is according to eq. (2.6) the current at time t that has been generated at time τ'. Integration yields

$$I(t) = I^{id}\left[1+\cos\left(\omega t - \frac{\omega\tau_{tr}}{2}\right)\cdot \mathrm{sinc}\frac{\omega\tau_{tr}}{2}\right], \tag{2.15}$$

where sinc x = (sin x)/x. The AC *current* amplitude is thus reduced by sinc$(\omega\tau_{tr}/2)$, whereas the DC amplitude remains the same. The 3 dB frequency of the THz *power*, P_{THz}~I^2, is given by $\mathrm{sinc}^2(\omega\tau_{tr}/2) = 0.5$. This yields a 3 dB frequency of $\upsilon^{tr}_{3dB} = 0.44/\tau_{tr}$. The reduction of the THz power with increasing frequency due to the transport of the carriers is called ***transit-time roll-off***. At higher frequencies, the THz power rolls off quickly. The nodes are attributed to our simplifying assumptions of identical carrier velocity and the same transit-time for all carriers. This is, of course, an unrealistic case for real diodes. The envelope function of the roll-off can be estimated by

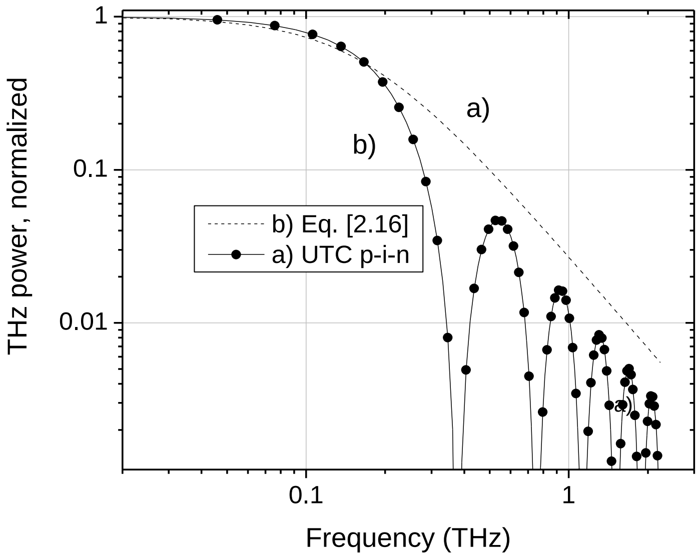

Fig. 2.4: (a) Approximate roll-off according to eq. (2.16). (b) THz power vs. frequency for a more realistic diode with a narrow absorption region close to the p-contact where carriers are quickly accelerated to the saturation velocity, v_{sat}, and then transported across the intrinsic layer with v_{sat} as calculated in ref. [18]. The nodes are due to neglecting the required acceleration period of the carriers and due to the narrow absorption region. Below the 3 dB frequency, eq. [2.16] reproduces the roll-off well. Above, the envelope shows the same power law dependence. The exact frequency dependence, however, depend on the details of the carrier transport [18].

$$\eta_{tr} \approx \frac{1}{1+(2\tau_{tr}\upsilon_{THz})^2}\,. \tag{2.16}$$

This envelope is illustrated in Fig. 2.4. A saturation velocity of ~10^7 cm/s (GaAs) and a transport length of 300 nm yield a 3 dB frequency of only 147 GHz. The THz power at higher frequencies will be strongly reduced. The envelope function decreases as υ^{-2} , similar to the RC roll-off. Obviously, the 3 dB frequency must be increased for efficient devices. One way would be to reduce the transport length. According to eq. (2.12), however, this increases the capacitance and therefore increases the effect of the RC roll-off. Our example of d_i = 300 nm yields for a fairly small device of 8 x 8 µm², an antenna with a radiation resistance of 70 Ω, and ε_r = 13 an RC 3 dB frequency of only 93 GHz. Such a device is already strongly RC-limited at THz frequencies and thicker intrinsic layers are required, opposing the transit-time limitation. Reducing the device cross section may be an alternative. In this case, the power density within the device will increase for a given optical power, which, in turn, limits the maximum current due to thermal and electrical issues. Since the THz power is proportional to the square of the photocurrent, smaller cross sections strongly reduce the maximum THz power. Thermal limitation will be discussed in detail in Section 2.3.1 of this chapter.

The transit-time performance can be improved without affecting the RC-time by optimizing the charge carrier transport within the diode. If the (average) velocity of the carriers can be increased, the same intrinsic layer length results in shorter transit-times and, hence, higher transit-time 3 dB frequencies. This requires a closer look on high-field transport in semiconductors on a short-time scale. In Fig. 2.5 a), the band structure of GaAs, a typical semiconductor with “direct band gap” at the Γ-point, E_Γ, is shown. Apart from the Γ-valley there are additional minima in the conduction band at the L-and the X-points of the Brillouin zone. As they are higher in energy by several 100 meV, the L- and X-valleys are normally not occupied by electrons and, hence, don’t contribute to transport. The absorption of photons with energy $h\nu$ larger than the band gap E_g results in the generation of electrons in the Γ-valley, (and of holes at the top of the corresponding valence bands). Due to the very small effective mass ($m_{eff}=0.067m_0$ for GaAs, e.g.) the accelation a of electrons by electric fields F, $a = eF/m_\Gamma$, is very efficient. For electrons at the bottom of the Γ-valley, there exist no efficient mechanisms for scattering.

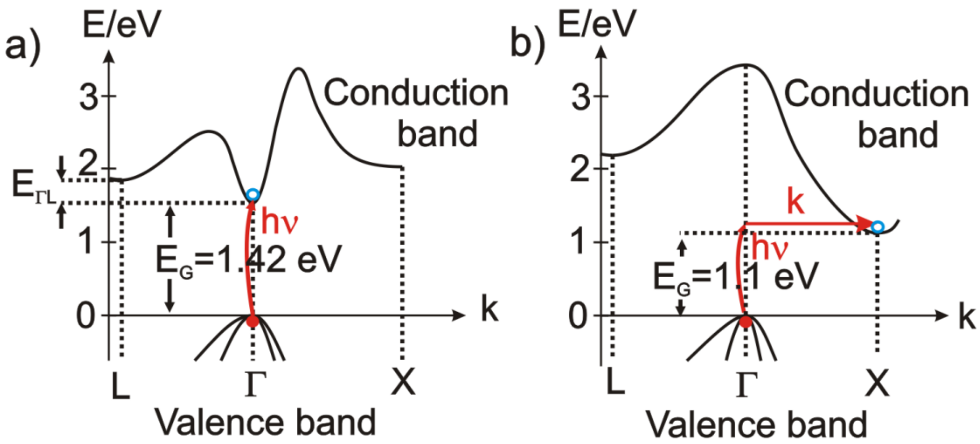

Fig. 2.5: Bandstructure GaAs (a) vs Silicon (b)

Therefore, they are “quasi-ballistically” accelerated, i.e. their velocity increases with time according to $v = at = \frac{eE}{m^*}t$. This quasi-ballistic motion persists until the electrons reach the energy of the side valley, $E_{\Gamma L}$. Here, extremely efficient intervalley phonon scattering from the Γ- into the L- side valley sets in. The effective masses in these valleys (reflecting the much smaller curvature of the band near the respective conduction band minima) is much larger. Further, very efficient phonon scattering between various side valleys randomizes their direction of motion, limiting the (average) drift velocity to the nearly field-independent saturation velocity $v_{sat} \approx 10^7$cm/s. Particularly InGaAs-based devices benefit from ballistic effects since the inter-valley energy of InGaAs of $E_{\Gamma L}$ = 0.46eV [19],[20],[21] is more than 50% higher than that of GaAs ($E_{\Gamma L}$= 0.29 eV [19],[21],[22]) and the effective mass in the Γ-valley is smaller (m_{eff} = 0.04 m_0). For InGaAs, the maximum ballistic velocity, $v_{bal} \approx 2x10^8$cm/s ($\approx 10^8$cm/s in GaAs) is about ten times higher than the saturation velocity, v_{sat}. Results of Monte-Carlo simulations of the transient velocity v*(t)* of an ensemble of electrons generated at $t = 0$ for InGaAs are depicted in Fig. 2.6 for different electric fields. With increasing field, the "velocity overshoot" approaches the maximum ballistic velocity. The left panel of Fig. 2.6 (b), depicting the distance covered by an electron within the time t, is particularly instructive. At a field of 20 kV/cm the electron travels over a distance of about 250 nm within less than 300 fs. At a field of 40 kV/cm the ballistic transport turns into propagation with saturation velocity already at about 150 fs and it takes several ps (!) before the electron will have covered the same distance of 250 nm. With increasing field the situation becomes even worse.

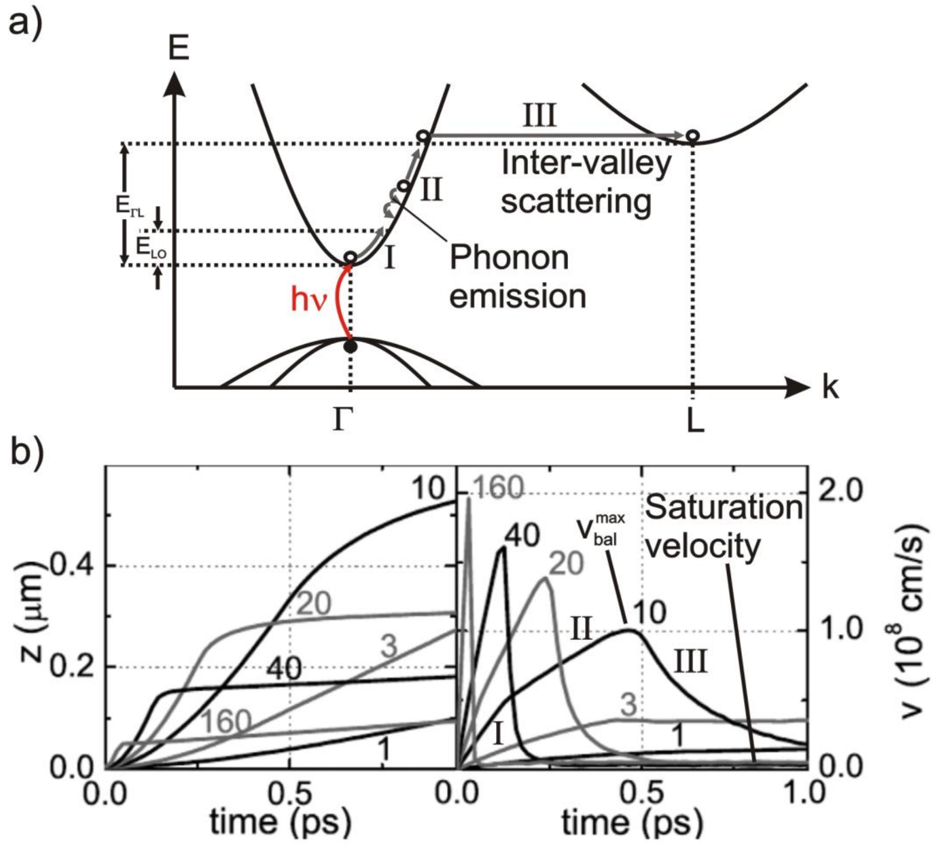

Fig. 2.6: a) Illustration of the electron transport in InGaAs (energy axis not to scale); in region I the electrons are accelerated with a=eE/m*. In region II, the electrons have surpassed a kinetic energy of E_{LO}. LO phonon emission results in a somewhat reduced acceleration of the electrons. III: The electrons reached the inter valley energy $E_{\Gamma L}$. Scattering in one of the 6 equivalent L-valleys strongly reduces the average velocity of the electron ensemble. b) Monte-Carlo simulation of the covered distance and the electron velocity for InGaAs for electric field strengths form 1 to 160 kV/cm. The regions I-III are indicated for the accelerating field of 10 kV/cm.

In semiconductors with an indirect band gap, like silicon (Si), the bandstructure in momentum space is illustrated in Fig. 2.5 b). X valleys are situated at the bandgap energy above the top of the valence bands, whereas the Γ-valley is found at higher energies. Therefore, the electrons always occupy these valleys, exhibiting a rather large effective mass, high scattering rates and, hence, much lower mobilities (μ < 1400 cm^2/Vs for Si) compared with direct gap semiconductors. The short-time high-field transport exhibits no velocity overshoot. The high-field drift velocities do not exceed the value $v = \mu E$ at any time. For Si, e.g. the stationary velocity is < 10^7cm/s, even at 100 kV/cm. Apart from the unfavourable transport properties, indirect bandgap semiconductors exhibit very low absorption coefficients near the bandgap as absorption takes place only via second order phonon-assisted processes. For these reasons, the “standard semiconductor” Si is practically not used for THz photomixing, all work focuses on (direct gap) III/V semiconductors.

Unfortunately, holes do not show any remarkable velocity overshoot. If electrons are quasi-ballistically transported, holes are much slower. There is a great benefit to generate holes close to or in the p-contact such that their transport length remains short. This is achieved by implementing a semiconductor with a band gap $E_G < h\upsilon$ at the p-contact where absorption and carrier generation can take place, followed with another, intrinsic semiconductor with $E_G > h\upsilon$ such that no carriers are generated there. The latter is called the *transport region* or *transport layer*. Since only electrons are transported, such devices are called *Uni-Travelling-Carrier (UTC)* photodiodes. A typical band structure is illustrated in Fig. 2.7. Another way to restrict the hole transport to a small fraction of the intrinsic layer is just modifying the intrinsic layer of a DH – p-i-n diode (see Fig. 2.2) by a gradually increasing Al-content towards the n-layer.

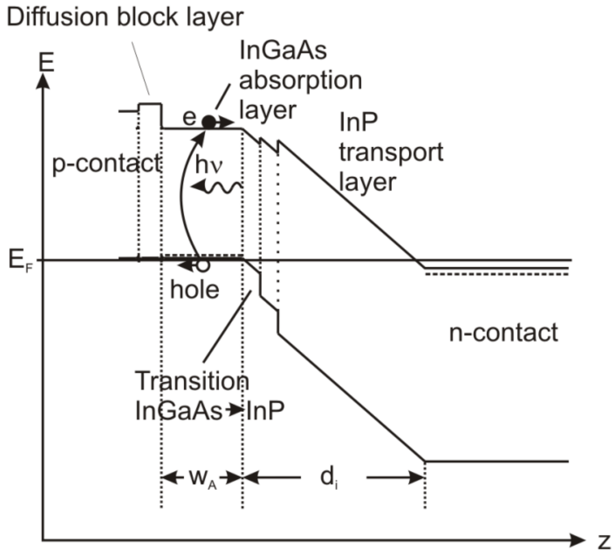

Fig. 2.7: Typical band structure of a Uni-Travelling-Carrier (UTC) photomixer. Photons are absorbed in the InGaAs absorption region and generate electron-hole pairs. The electrons are transported across the InP transport layer to the n-contact, Holes drift to the p-contact.

In order to get the optimum transport field, i.e. the field in the intrinsic layer where the electrons are transported ballistically as far as possible (see Fig. 2.6), a small external DC bias can be applied to the diode. Since quasi-ballistic electrons can reach peak velocities that are about a factor of 10 higher than the saturation velocity, their average velocity is up to a factor of 3-4 higher. For our example with an intrinsic layer length of 300 nm, this yields a transit-time 3 dB frequency of about 0.75 THz and increases the THz power at high frequencies by a factor of 25 according to eq. [2.16]. The RC roll-off can be improved by using smaller devices (which will ultimately limit the maximum photocurrent) or by using a series connection of p-i-n diodes as realized by the n-i-pn-i-p superlattice photomixer concept [23]. Various layouts of p-i-n diode based photomixers will be discussed in Section 2.4.

2.2.2.2 Photoconductive mixers

The second type of photomixers is the photoconductive mixer. It consists of a highly resistive semiconductor that is covered with metal contact electrodes as illustrated in Fig. 2.8. The heterodyned laser beams are absorbed by the semiconductor in the electrode gap, leading to the generation of electron-hole pairs. Since there is no built-in field as in p-i-n diodes, an external DC bias is required in order to separate the carriers and generate a photocurrent. Typical bias levels range from a few Volts to ~100 V, depending on the electrode gap, w_G.

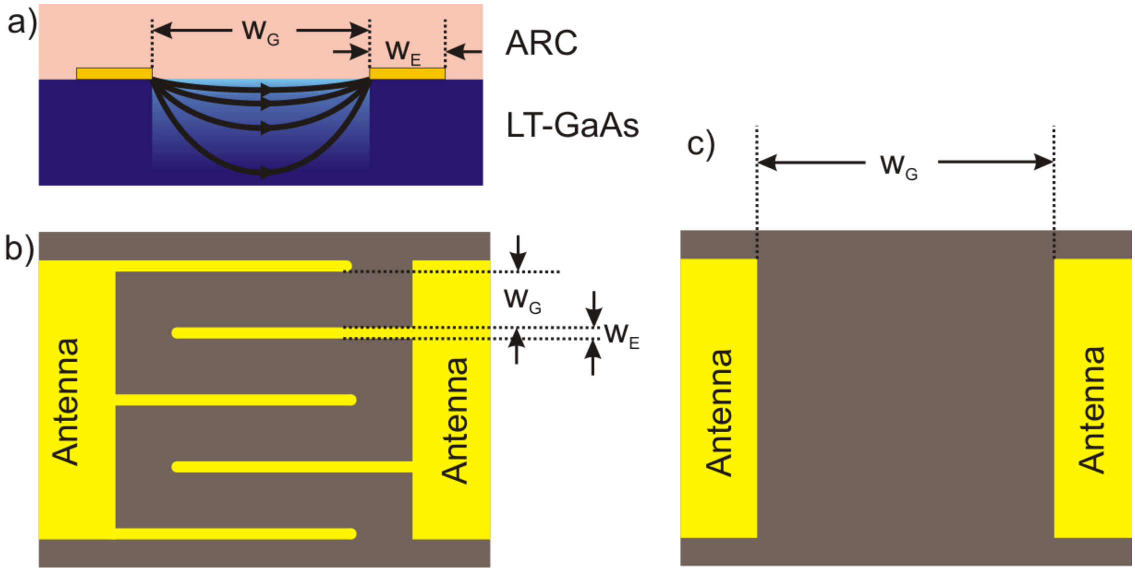

Fig. 2.8: a) Cross section of a photoconductor. The electric DC fields, due to biasing the electrodes, are indicated by the bowed lines. The gradient illustrates the amount of photo-generated carriers in the gap (logarithmic scale; bright: many carriers, dark:few carriers). b) Top view of a photoconductive mixer with fingers for CW operation. c) Fingerless gap for pulsed operation.

Fig. 2.8 a) shows the side view of the electrode structure. The electric field in the gap is inhomogeneous. The field lines become longer the deeper we look in the photoconductive material. The highest field strengths are at the surface in the vicinity of the electrodes. In addition, the electron-hole generation rate is highest at the surface. The absorption follows Lambert-Beer's law according to eq. (2.10). Typical values of the absorption coefficient of 11 000 cm^{-1} (GaAs at 840 nm wavelength) yield a *1/e* penetration depth of 0.9 µm. This value is roughly the required thickness of the photoconductive material for high absorption. The thickness of the active photoconductive layer and the inhomogeneity of the absorption may be reduced by growing a Bragg reflector below the photoconductor. Often, an anti-reflection coating (a transparent dielectric layer of width $d=\lambda_0/(4n)$, where $n \approx \sqrt{n_{sc}}$ is the refractive index of the dielectric) is applied on top of the electrode structure in order to reduce reflection and to passivate the structure. The latter is very important since both carrier generation and electric fields are highest at the surface. The generated heat can lead to oxidation and finally to the destruction of the device.

In most cases, an antenna is connected to the electrodes in order to emit THz radiation. Similar to p-i-n diode based photomixers, photoconductors also show an RC roll-off towards high frequencies. The capacitance of a finger-like electrode structure as illustrated in Fig. 2.8 a) is [20]

$$C = \frac{K(k)}{K(k')} \cdot \frac{\varepsilon_0(1+\varepsilon_r)}{w_e + w_g} A, \qquad (2.17)$$

with $k = \tan^2(\pi w_e / [4(w_e + w_g]), k' = \sqrt{1-k^2}$, and $K(k) = \int_0^{\pi/2} \frac{d\theta}{\sqrt{1-k^2 \sin^2\theta}}$ is the complete elliptic function of the first kind, w_g is the gap width, w_e is the electrode width, and A is the total (square) active area. In order to assure efficient coupling of the lasers, the diameter of the electrode structure must be of the same order as the laser beam diameter. Typical values are 10 x 10 μm². An electrode width of w_e = 0.2 μm and an electrode gap of 1.8 μm, requires 5 electrodes in order to cover 10 μm. This yields a capacitance of 1.7 fF. For an antenna with 72 Ω, the RC 3 dB frequency is 1.3 THz. We see that much smaller electrode gaps are not beneficial for RC-roll-off free operation below 1 THz. Further, the area covered by the metal electrodes cannot be optically excited. Smaller gaps at a fixed, finite electrode width therefore reduce the optically active area.

<u>(a) CW operation</u>

Similar to p-i-n diodes, the transport of carriers also results in a roll-off. For continuous-wave operation, the semiconductor is always populated with optically generated carriers. In p-i-n diodes, transport lengths of a few 100 nm already result in a transit-time 3 dB frequency below 1 THz. Typical gaps of (continuous-wave operated) photoconductors, however, are in the range of 2 μm. In order to speed up the carrier transport, high biases have to be applied to the electrodes. For a close-to break-down field of ~300 kV/cm for GaAs at the surface, a maximum bias of 60 V can be applied for a 2 μm electrode gap. For high quality GaAs with a mobility of μ = 8 000 cm²/(Vs), carriers can easily reach the saturation velocity of ~ 10^7 cm/s at such accelerating fields. This results in a transport time of τ_{tr}~16 ps where the time for accelerating the carrier was even neglected. Velocity overshooting effects can be neglected at these time scales since they only play a role in the first few 100 nm of the transport and require lower fields. For intrinsic GaAs, the transit-time 3 dB frequency is only $\nu_{3dB}^{tr} = 1/2\tau_{tr}$ =31 GHz. Such a low value would result in a severe roll-off at THz frequencies since most carriers would need too much time to cross the electrode gap. Therefore, (continuous-wave) photomixers use materials with a short carrier lifetime, where carriers are trapped (and subsequently recombine with their counterparts) on their way to the electrode and do not contribute to the displacement current any more. In order to calculate the displacement current, we assume transport at the (constant) saturation velocity without any velocity overshoot (which does not play any role in short lifetime material). We further simplify the transport by assuming a transport length of the electrode gap since most electrons are generated close to the surface. The number of charges are generated at time *t'* within a time interval $\Delta t'$ by the beating of the lasers is $\Delta N(t') = \eta_I^{ext} I^{id} [1+\cos(\omega_{THz} t')]\ \Delta t'$, according to eq. 2.6. They undergo exponential damping due to fast trapping and recombination within τ_{rec}. At a time $t > t'$, only $\Delta N(t')\ \exp(-[t-t']/\tau_{rec})$ carriers have survived. In order to calculate the displacement current, all remaining carriers (i.e. are not trapped) have to be considered to contribute to the current. The displacement current *density* is given by $j=en\mathrm{v}_{dr}$, where v_{dr} is the drift velocity, and $en=N/V$ is the charge density per volume. The volume is spanned by the gap width, w_G, along the x direction, the *1/e* penetration depth of the laser, z_0, and the length of the electrode, y_0, yielding $V=z_0 y_0 w_G$. The area $A= z_0 y_0$ is the cross section of the current, $I=jA$. At time t, the current generated in the former time interval $[t', t'+\Delta t']$ the generated current is $\Delta I(t,t') = \Delta N(t')\ v_{dr}/w_g \exp(-[t-t']/\tau_{rec})$. The term $w_g/\mathrm{v}_{dr} = \tau_{tr}$ is the transport-time of the carriers. The displacement current at time t is

$$I(t) = \frac{1}{\tau_{tr}} \int_{t-t'=0}^{t-t'=\tau_{tr}} \eta_{ext}^{I} I^{Id} [1+\cos(\omega_{THz} t')] \exp(-[t-t']/\tau_{rec}) dt' , \tag{2.18}$$

where *t-t'* is the transport time of a carrier after its generation. Since most of the carriers should be trapped on their way to the contact, we can assume that the transport time is much larger than the trapping/recombination time, $\tau_{tr} >> \tau_{rec}$, and therefore we can shift the upper integration boundary towards infinity with marginal error. For the same reason, we can also ignore the dependence of the transit-time with respect to the place of generation of the carriers with respect to the electrodes. Substituting $t\text{-}t' = \tau$ and integrating eq. (2.18) yields

$$I(t) = \eta_{ext}^{I} I^{id} \frac{\tau_{rec}}{\tau_{tr}} \left[\frac{\sin(\omega_{THz} t - \varphi)}{\sqrt{1+(\omega_{THz}\tau_{rec})^2}} + 1 \right] , \tag{2.19}$$

with $\varphi = \arctan(\omega_{THz}\tau_{rec})$. We see that both the time-dependent (AC) and the DC part of the current are damped due to trapping by a factor of $g = \tau_{rec}/\tau_{tr}$. Although this quantity is usually (much!) smaller than 1, it is called the ***photoconductive gain***. The time dependent (AC) current is further reduced by a factor of $\left(\sqrt{1+(\omega_{THz}\tau_{rec})^2}\right)$. Since the THz power is $P \sim I^2$, the power is reduced at high frequencies by

$$\eta_{LT} = \frac{1}{1+(2\pi\upsilon_{THz}\tau_{rec})^2} , \tag{2.20}$$

where we replaced $\omega_{THz} = 2\pi\nu_{THz}$. Mathematically, this ***life-time roll-off*** has the same form as the transit time roll-off for p-i-n diodes in eq. (2.16), however, with a 3 dB frequency of $\upsilon_{3dB}^{LT} = 1/(2\pi\tau_{rec})$ that is formally a factor of π smaller than the transit-time 3 dB frequency. Compared to an ideal device, the emitted THz power of a photoconductor is reduced by

$$\eta_{PC} = \frac{g^2}{1+(2\pi\upsilon_{THz}\tau_{rec})^2} . \tag{2.21}$$

In order to obtain a flat frequency response of the device, short life-times, τ_{rec}, are required. However, it should not be too small since the photoconductive gain is also proportional to the life-time (the latter becomes important when we discuss thermal limitation of a photoconductor in Section 2.3.1). A low life-time reduces the mobility of the carriers, requiring higher fields in order to accelerate them. Particularly for CW operation, engineering of the carrier lifetime of the photoconductive material is of key importance for efficient operation. For a flat frequency response up to 1 THz, a life-time of 160 fs is required. Examples of materials with such a short carrier life-time will be given in Section 2.3. Optimum values for both life-time and electrode gap for photoconductors have been calculated in ref. [24] for both a typical resonant antenna and a typical broadband antenna.

(b) Pulsed operation

For pulsed operation, a short life-time is not so crucial for the photoconductor (or Auston switch, named after David Auston who first used photoconductors for generation of THz pulses). According to eq. (2.9), the (ideal) THz spectrum is proportional to the spectral width of the photocurrent. Even if the decay of the current is slow (i.e. on the time scale of 20 ps as for the case of intrinsic GaAs), the turn-on can be fast, providing high frequency components in the Fourier spectrum. Further, the material can relax on long time scales between two subsequent pulses - in contrast to the CW case where carriers are continuously generated.

In order to derive the emitted THz spectrum under pulsed operation, the details of the photocurrent generation have to be investigated. The generated field by a radiating structure (such as an antenna or by any current) is proportional to the time-derivative of the current [25],[26],[27]. The photocurrent density at time *t* resulting from a carrier density, $n(\vec{r},t,t')$ at position $\vec{r}$, generated at time *t'* at depth *z* with respect to the surface is given by

$$\partial\vec{j}_{Ph}(\vec{r},t,t') = e\vec{v}(\vec{r},t-t')\ \partial n(\vec{r},t,t')\,, \tag{2.22}$$

where $\vec{v}(\vec{r},t-t')$ is the velocity of the carriers at time *t*. The photoconductor may feature a short carrier life-time, yielding $n(\vec{r},t,t') = n_0(\vec{r},t')\exp(-[t-t']/\tau_{rec})$ as for the CW case. For the total current, holes and electrons have to be considered. Since the formulas are the same for both carrier types, we will restrict our treatment to electrons only. However, holes feature a larger effective mass and do not show any velocity overshoot, resulting in smaller values for $\vec{v}(\vec{r},t-t')$. Consequently, the contribution of hole currents is usually smaller. Further, we will for now only treat the small-signal limit, neglecting any saturation effects which will be treated later in Section 3.2. The electron-hole generation *rate* is proportional the optical power,

$$\frac{\partial n_0(\vec{r},t')}{\partial t'} = \alpha\frac{P_L(\vec{r},t')}{h\overline{\upsilon}A} = \alpha\frac{\Phi_L(\vec{r},t')}{h\overline{\upsilon}}\,, \tag{2.23}$$

where *A* is the device cross section where the optical power, $P_L(\vec{r},t-\tau) = \exp(-\alpha z)P_{L,0}(x,y,t-\tau)$, is distributed, and α is the absorption coefficient of the photoconductor. $\Phi_L(\vec{r},t') = P_L(\vec{r},t')/A$ is the optical intensity. Substituting eq. [2.23] into eq. [2.21] and integrating over the photoconductor cross section yields for the local current

$$I_{Ph}(x,t) = \int\int_{t-t'=0}^{t-t'=\tau_{tr}(x)} e\alpha\frac{\Phi_L(\vec{r},t')}{h\overline{\upsilon}}\exp(-[t-t']/\tau_{rec})v_T(\vec{r},t-t')dt'\ dz\ dy\,, \tag{2.24}$$

Where $v_T(\vec{r},t-t')$ is the surface-tangential component of the velocity. In order to get the total displacement current, we have to summarize over all components generated at all coordinates *x*.

$$I_{Ph}(t) = \frac{1}{w_G}\int_0^{w_G} I_{Ph}(x,t)dx \tag{2.25}$$

The same formula applies to the field generated by holes. The two contributions have to be summed up in order to provide the total field.

Since the carrier velocity depends on both the field strength of the accelerating DC field (see Fig. 2.6 a)) and the carrier dynamics in the semiconductor (ballistic acceleration vs. transport at the saturation velocity), eq. (2.25) can only be solved analytically by making a few simplifying assumptions. We are only interested in the temporal evolution. The majority of the carriers will be generated close to the surface. The fields at small penetration depths are very similar, resulting in little spatial variation of the carrier velocities. Since the electric field is proportional to the time derivative of the current, we are only interested in time-varying components. This means that either the pulse duration or the carrier life-time (or both) should be much shorter than the transit-time. We further assume a homogeneous illumination. Gaussian beams could also be considered. however, they make the derivations more complicated. Under these simplifying assumptions, the integrand does not possess any spatial dependence any more. The spatial integrals result in the total absorbed power. Dropping all other constants and substituting $t\text{-}t'=\tau$ yields

$$E_{THz}(t) \sim \frac{\partial}{\partial t}\int_0^{\tau_{tr}} P_L(t-\tau)e^{-\tau/\tau_{rec}}v(\tau)d\tau. \qquad (2.26)$$

In order to investigate the influence of the optical pulse width and the life-time of the carriers, we will now focus on a few important special cases. The first case is that of a photoconductor with a long life-time. The exponential damping due to the life-time can be neglected. The transit-time should be long compared to the pulse duration. The transport shall be non-ballistic providing $v(\tau)=v_{sat}=const$. The device is excited with a very short Gaussian pulse, $P_L(t)=P_0\exp(-t^2/\tau_{pls}^2)$, where τ_{pls} is the pulse duration. The THz-field becomes

$$E_{THz}(t) \sim \frac{\partial}{\partial t}\int_0^{\infty} P_L(t-\tau)v_{sat}d\tau \sim v_{sat}P_L(t)\,. \qquad (2.27)$$

The generated electric field is then simply proportional to the optical pulse, $E_{THz}(t) \sim P_0\exp(-t^2/\tau_{pls}^2)$ as illustrated in Fig. 2.9 a) with a power spectral density of

$$P_{THz}(\omega) \sim |E_{THz}(\omega)|^2 \sim v_{sat}^2 P_L^2(\omega), \qquad (2.28)$$

with $P_L(\omega)=P_0\ \exp(-\omega^2\tau_{pls}^2/4)$. This calculated field, however, is not the emitted THz field. It is strictly positive and therefore contains also a DC component which cannot be radiated. In addition, any kind of THz setup has a cut-off frequency: At lower frequencies, implemented antennas and apertures must become larger (of the order of the wavelength at least) which ultimately will hit experimental limits. Often, low frequency components may also be suppressed by the used detection technique due to a detector cut-off or similar. Therefore, low frequency components are always filtered. Removing the low frequency components results in a single cycle THz pulse as obtained in experiments. Its frequency spectrum is shown in Fig. 2.9 b). It is of Gaussian shape, dropping fast at frequencies above $\upsilon_{3dB}=\sqrt{\ln 2}/\left(\sqrt{2}\pi\tau_{pls}\right)$. Here, no RC roll-off was taken into account. Similar to CW operation, the RC roll-off will reduce the power at higher THz frequencies.

For most practical cases, the transit-time, τ_{tr}, is orders of magnitude longer than all other involved time scales. For the following cases, the upper integration boundary of eq. (2.25) will therefore be shifted to infinity and explicit dependencies on the transit time of the carriers will be neglected. By continuing the velocity, v(τ) towards negative values of τ by adding zeroes, i.e. setting $v^*(\tau)$=v$(\tau)\theta(\tau)$, where $\theta(\tau)$ represents the Heavyside step function, the lower integral boundary of eq. (2.25) can be set to -∞. With

$$h(\tau) = \exp(-\tau/\tau_{rec})\mathrm{v}(\tau)\theta(\tau) \tag{2.29}$$

eq. (2.25) becomes a convolution of the pulse shape and the function $h(\tau)$,

$$E_{THz}(t) \sim \frac{\partial}{\partial t}[P_L(t) * h(t)], \tag{2.30}$$

where "*" represents the convolution. If both functions are integrable, the Fourier transformation of eq. (2.26) yields the simple result [28]

$$E_{THz}(\omega) \sim i\omega P_L(\omega)H(\omega), \tag{2.31}$$

With the power spectrum of [28]

$$P_{THz}(\omega) \sim \omega^2 \,|\, P_L(\omega)\,|^2 \cdot |\, H(\omega)\,|^2, \tag{2.32}$$

i.e. the product of the power spectrum of the laser, the power spectrum of the carrier dynamics (represented by the function $H(\omega)$) and the term ω^2. The term $\sim\omega^2$ can be identified with the Hertzian dipole radiation resistance $R_A^H \sim \omega^2$ [29]. It needs to be replaced by the frequency dependence of the antenna radiation resistance if any is used.

Eq. (2.32) is a powerful tool in order to calculate the emitted spectra since it separates the influence of the pulse shape and the carrier dynamics. If the device shows an RC roll-off, it can simply be multiplied to Eq. (2.32).

We now focus on two further important cases by using Eq. (2.32): next, a photoconductive material with a short life-time, τ_{rec}<1 ps. Since scattering dominates the transport in a low life-time material, no velocity overshoot has yet been reported. Therefore, the carrier velocity can be assumed to be the saturation velocity, v (τ)=v_{sat}=*const*. For typical accelerating fields, the time required to accelerate the carriers is very short. Therefore, the carriers are assumed to be moving at the saturation velocity for the whole transport, neglecting slower velocities right after carrier generation. Furthermore, the short lifetime assures that the dependence of the point of generation does not play any dominant role and the transit-time can be set to infinity. This results in the integrable function $h(\tau) = \exp(-\tau/\tau_{rec})\mathrm{v}_{sat}\theta(\tau)$. The power spectrum is

$$|\, H(\omega)\,|^2 = \frac{\mathrm{v}_{sat}^2 \tau_{rec}{}^2}{1 + (\omega\tau_{rec})^2} \tag{2.33}$$

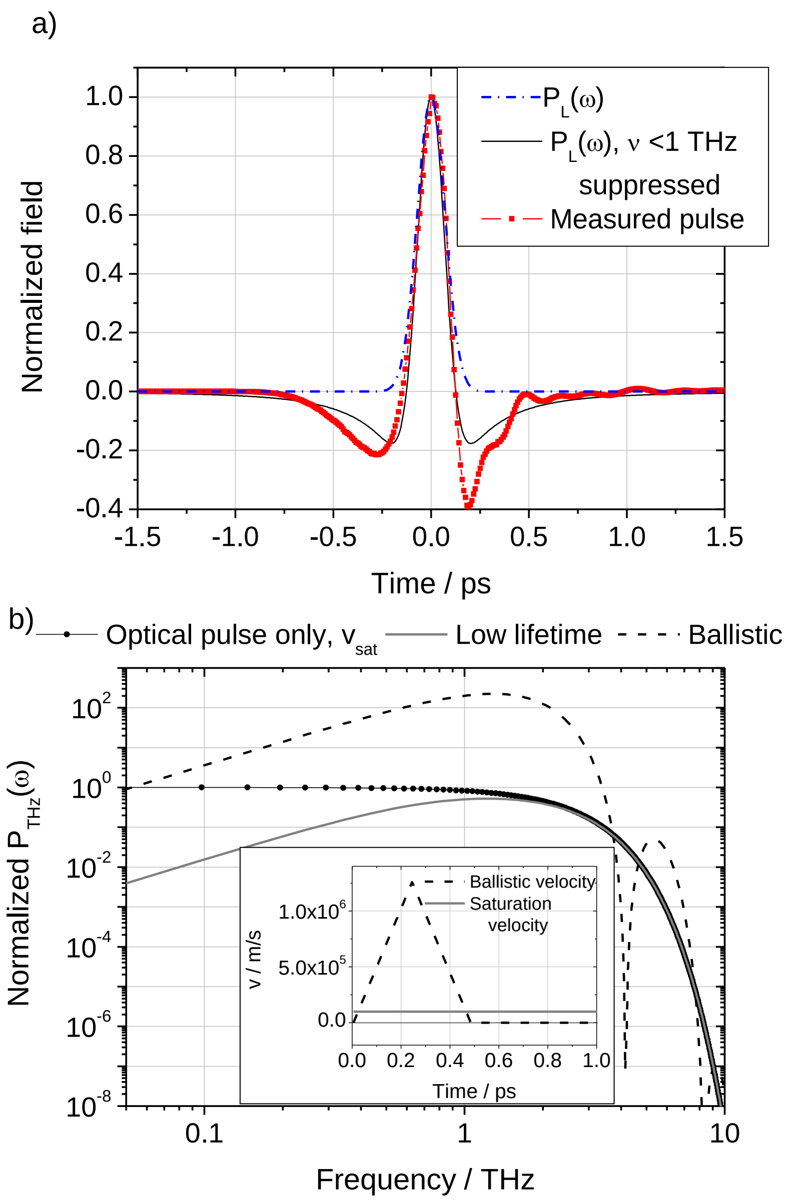

Fig. 2.9: a) Dashed line: Calculated field according to Eq. (2.28) for τ_{pls}=100 fs. Solid line: pulse resulting from the dashed line by suppressing frequency components below 1 THz as ~ω². Line with symbols: An experimentally obtained THz pulse with a comparable pulse duration. b) Fourier spectra of the fields: solid line with points according to Eq. (2.28) for semi-insulating (SI) GaAs. Grey solid line: Response of a material with short lifetime according to Eq.(2.34). Dashed line: Spectrum of a material with ballistic transport according to Eq. (2.36). Inset: Assumed velocity trace for ballistic and non-ballistic transport.

The function $|H(\omega)|$ can be identified as the effective dipole responsible for THz generation, namely the covered distance of separated electrons and holes, $l_D = v_{sat}\tau_{rec}$, and a transit-time roll-off.

The power spectrum according to Eq. (2.26) is

$$P_{THz}(\omega) \sim \frac{(\omega v_{sat}\tau_{rec})^2}{1+(\omega\tau_{rec})^2} P_L^2(\omega). \qquad (2.34)$$

It is also illustrated in Fig. 2.9. Note that the transit-time roll-off term in $|H(\omega)|$ does not prevent generation of high frequency components since $P_L(\omega)$ contains these frequencies. Above $\nu>(2\pi\tau_{rec})^{-1}$, the frequency dependencies of the prefactor in Eq. (2.34) cancel, resulting in $P_{THz}(\omega) \sim v_{sat}^2 P_L^2(\omega)$ as in the case of semi-insulating (SI) GaAs with transport at the saturation velocity.

The last case is that of a material with ballistic electron transport. Ballistic transport is not possible in a short lifetime material. Therefore, the lifetime must be long, the exponential term in Eq. (2.23) has to be dropped. The electron velocity distribution shown in Fig. 2.6) is quite complex. We approximate the onset of the transport by a ballistic acceleration of $a = e/mE_{DC}$, where E_{DC} is the accelerating field resulting from the DC bias to the structure. This acceleration will prevail until the electron reached enough energy to scatter into the side valley. This happens after a ballistic flight time of

$$\tau_{bal} = \sqrt{\frac{2m^* E_{\Gamma L}}{e^2 E_{DC}^2}} \qquad (2.35)$$

Eq. [2.35] was obtained by equating the inter-valley energy $E_{\Gamma L}$ to the kinetic energy of the electron. For simplicity, we assume that the deceleration due to scattering happens with an acceleration of $a' = -a$ until the electron is at rest. According to Fig. 2.6 b), right panel, this is a rather realistic assumption. Of course, in the experiment the electron density will not be at rest but rather traveling with the saturation velocity. Due to the time derivative and the Fourier transformation, transport at a constant saturation velocity does not play any role. For an optimum accelerating field of 20 kV/cm and an effective electron mass of $m^*=0.067m_0$, the acceleration is $a=5.25x10^{18}$ m/s²and the ballistic flight time is τ_{bal}=0.24 ps. The power spectral density of the carrier dynamics, $|H(\omega)|^2$ is then

$$|H(\omega)|^2 = \left(v_{bal}^{\max}\tau_{bal}\right)^2 \left(\mathrm{sinc}\frac{\omega\tau_{bal}}{2}\right)^4, \qquad (2.36)$$

where $v_{bal}^{\max} = a\tau_{bal}$ is the maximum ballistic velocity of the carriers. The power spectrum according to Eq. (2.28) generated by the electrons is shown in Fig. 2.9. Since holes do not show any remarkable velocity overshoot, their contribution will follow Eq. (2.25) and has to be summed up with the electron contribution.

The derived spectra are the idealized cases only. We neglected contributions of carriers that are further away from the surface. The accelerating fields are lower, such that lower frequency components will be generated. Further, any device specific roll-offs and the frequency dependence of the antennas will alter the generated spectra. The latter, however, can simply be multiplied to the respective spectra (Eqs. (2.28), (2.34), and (2.36)).

Comparing ballistic SI-GaAs (Eq. (2.36)) with non-ballistic low-temperature grown (LTG)-GaAs (Eq.(2.28)) shows that the emitted power is proportional to the square of product of the relevant transport time and the transport velocity, $d_{bal} = v_{bal}^{\max}\tau_{bal}$ for the case of ballistic transport and $d_{LT} = v_{sat}\tau_{rec}$ for a short life-time material. This is the length of the respective dipole that is responsible for THz generation. For the ballistic case, the dipole length can be as large as $d_{bal} = 300$ nm, whereas the dipole length for the short life-time material is only of the order of 20 nm (for a life-time of τ_{rec}=200 fs). For the specific example, SI-GaAs produces more than 200 times higher output power for the same biasing conditions and same electrode layout. In the next section, we will see that semi-insulating material has some draw backs in terms of damage threshold and biasing which levels the performance of both materials.

We note that Eq. (2.28) is so general that it can also be used to derive the frequency response of the material under CW operation for a Hertzian antenna and for p-i-n diodes as long as the respective transport kinetics are taken into account. The spectral answer of the CW photomixer becomes

$$P_{THz}(\omega) \sim r_A^H(\omega)\,|\,P_L(\omega)\,|^2 \cdot |\,H(\omega)\,|^2, \qquad (2.37)$$

where we used $r_A^H(\omega) \sim R_A^H(\omega)/l_D^2 = \omega^2/(6\pi\varepsilon_0\varepsilon_r c^3)$ for the radiation resistance of a Hertzian dipole normalized to its length. For CW lasers with a Gaussian linewidth, $\Delta\omega$, the optical power is $P_L(\omega) \approx P_0 \exp(-\omega^2/\Delta\omega^2)$. Typical values for the linewidth are in the few MHz range. The term $|H(\omega)|^2$ for all discussed transport mechanisms is spectrally much broader, i.e. in the range of THz. The generated THz power spectrum is therefore dominated by the spectral characteristics of the lasers, the actual carrier transport only plays a minor role. From a Physics picture, the non-harmonic components of the current interfere away, only the components at the difference frequency of the lasers survive.

2.2.2.3 Photoconductors as THz detectors

Photoconductors can also be used as THz detectors. When no bias is applied, optically generated electron-hole pairs just recombine without generation of a displacement current. If, however, an antenna is coupled to the electrodes in order to receive a THz signal, a bias at the THz frequency will be generated. This bias is proportional to the THz field strength. For a CW signal, the bias is $U_{THz}(t) \sim E_{THz}\cos(\omega_{THz}t + \varphi)$. If the electrode gap is excited with the same laser signal that was used to generate the THz signal, the carrier generation rate is modulated at the same THz frequency, $n(t) \sim P_L(t) = P_L(1 + \cos\omega_{THz}t)$. The carrier velocity is modulated by the received THz field as well, since $v(t) \sim \mu U_{THz}(t) \sim E_{THz}\cos(\omega_{THz}t + \varphi)$. The resulting current is proportional to the product of carrier velocity and carrier concentration, $I(t) \sim n(t)v(t) \sim \cos(\omega_{THz}t)\cos(\omega_{THz}t + \varphi)$ andthe device behaves like a homodyne mixer generating a DC component of

$$< I > \;\sim\; < U_{THz}(t)P_L(t) > \;\sim\; E_{THz}P_L\cos\varphi, \qquad (2.38)$$

where the brackets stand for the time average of the quantities. The phase, φ, is due to a finite delay (for instance by different optical path lengths, d, between the optical and the THz wave, i.e. $\varphi = k_{THz}d$. The photoconductor is therefore a homodyne mixer where both field amplitude and phase are detectable.

In a similar fashion, photoconductors can be used as detectors in pulsed systems. The optical pulse is used to scan the THz pulse by including a delay time, τ. The resulting DC signal is the convolution of the optical signal and the THz field,

$$I(\tau) \;\sim\; \int E_{THz}(t)P_L(\tau - t)dt\,. \qquad (2.39)$$

The optical pulse therefore “samples” the electric field THz strength. Its Fourier transform yields the THz power spectrum. This technique is frequently applied in Terahertz spectroscopy and is called “Time domain spectroscopy”. Often, the understanding of the detection mechanism is that the THz pulse is sampled with a much narrower, optical pulse, similar to electronic sampling. Eq. (2.25), however, shows that the THz field can have the same spectral shape and same temporal width as the optical beam. It is easy to show that the same Gaussian pulse shape of optical and THz beam, Eq. (2.35), results in a broadening of the detected signal *I(t)* by a factor of √2. Other typical pulse shapes like $\mathrm{sech}^2(t/\tau_{pls})$ result in similar factors. The measured signal appears temporally wider and spectrally narrower than the actual THz signal. On a first glance, this result may render spectroscopic data of TDS systems useless, since the measured spectrum differs from the spectrum of the actual THz signal. In spectroscopy, however, it is not the individual spectrum that is important but rather the ratio of the spectrum of a transmitted or reflected signal by a device under test, and the reference signal. The Fourier transform of Eq. (2.39) is

$$I(\omega) \sim E_{THz}(\omega) P_L(\omega) \tag{2.40}$$

The transmission (or alternatively, the reflection) coefficient for a transmitted (reflected) signal $I_M(\omega)$ and a reference signal $I_R(\omega)$ is

$$t(\omega) = \frac{I_M(\omega)}{I_R(\omega)} = \frac{E^M_{THz}(\omega)}{E^R_{THz}(\omega)}. \tag{2.41}$$

The dependence on the spectrum of the optical pulse (and other experimental parameters) simply cancels out. The time domain data result in the correct THz spectra, independent of the optical pulse spectrum.

2.2.3. Thermal Constraints

The THz power of photomixers increases with the square of the laser power, $P_{THz} \sim P_L^2$. Therefore, the highest possible laser power should be used, if reasonably large THz power is desired. This, however, leads to excessive heating with several unfavorable effects on the device performance. First, the increased phonon scattering rate at higher temperature reduces carrier mobility as well as ballistic benefits. The transit time increases and reduces the THz power at high frequencies, ($\upsilon_{THz} > \upsilon_{tr}^{3dB}$). Second, the device ages faster, since high temperatures allow for (exponentially) increased dopant and trap migration, finally leading to break-down of the device. To estimate the effects due thermal dissipation, we look at the thermal conductivity of a semiconductor, which can be approximated by [30]

$$\lambda_{th}(T) \approx \lambda_{th}(T_0) \cdot (T_0/T)^c. \tag{2.42}$$

For most semiconductors, the exponent c is larger than 1, resulting in a reduced thermal conduction at higher temperatures. As an example, *c=1.375* for InGaAs lattice matched to InP or *c=1.55* for InP. Further, the band gap shrinks with increased temperature, leading to a higher absorption coefficient, and increased optical power dissipation. Both effects may lead to thermal runaway of the device and, finally, its destruction. In this section, the maximum optical power and electric fields for safe device operation will be estimated. Furthermore, we will discuss device design issues in order to reduce thermal effects.

In the last section, the life-time roll-off for photoconductors was introduced in Eq. (2.19). An expansion of η_{PC} with respect to τ_{rec} yields $\eta_{PC} \sim (\tau_{rec})^2$ for $\upsilon < \upsilon_{3dB}^{LT}$ and $\eta_{PC} = \upsilon_{THz}^{-2}$ for $\upsilon >> \upsilon_{3dB}^{LT}$. So it seems that short lifetimes reduce the output power at low frequencies and are of no use at high frequencies. The picture changes when we take thermal limitation into account. Any photomixer experiences two heat sources: 1.) Current under an external bias results in Joule heating 2.) Absorbed laser power, which is not directly converted into current. Photoconductors with small gain, g, generate very little external current, $I_{ext}=gI_{id}$, where $I_{id}=eP_L/h\nu$ is the ideal photocurrent due to *absorbed* optical power. The Joule heat is $P_H^J \approx I_{ext}U_{DC} = gI_{id}U_{DC}$, with the external bias U_{DC}. Joule heating can be reduced by using small gain values in order to reduce the external current. This fact explains why materials with a short life-time are so successful in the THz range as compared to materials with a long lifetime: they can tolerate much higher optical power levels due to reduced Joule heating. For p-i-n diodes, Joule heating is less dramatic than for photoconductors, since little external bias, U_{DC}, is required during operation. Heating by absorbed laser power is more important. P-i-n diode-based photomixers are typically operated under reverse bias. Therefore, most of the optical power is transformed into heat since carriers emit phonons while relaxing to the band edge during transport to the respective contact. For photoconductors, just a small fraction of the laser power is extracted as current due to the low gain. In both cases, the heat produced by the laser is approximately given by the optical power, $P_H^L \approx P_L$. The total heat dissipated by the photomixer is given by [24]

$$P_H \approx P_L\left(1 + g\frac{e}{h\upsilon_L}U_{DC}\right), \tag{2.43}$$

Where g=1 for p-i-n diodes. A maximum temperature change of ΔT_{max}=120 K has been determined empirically for GaAs photoconductors before damage occurs [31]. Given that there is sufficient lateral heat spreading (i.e. a constant temperature in the cross section), heat is transported as

$$P_H = \Delta T_{max}\, \lambda A/d \tag{2.44}$$

In most cases, however,, the heat source due to absorption of the lasers can be identified as a thin disk (i.e. the absorbing semiconductor) on a thermal conductor (i.e. the substrate) [20]. This yields

$$P_H \approx \Delta T_{\max}\lambda\sqrt{\pi A}. \tag{2.45}$$

For GaAs with a thermal conductance of λ=0.43 W/cm K, a device cross section of A=50 μm² results in a maximum thermal power of P_H =65 mW according to Eq. (2.45).

Since $P_L<P_H$ this is also the maximum limit for the optical power. However, devices are illuminated with a laser that often features approximately Gaussian shape. The non-homogeneous optical power distribution may lead to a failure at (much) lower optical power levels. Typically, an absorbed optical power of the order of 50 mW for a photoconductor (A~50μm²) are considered to be safe for long term use in photoconductors. For UTC diodes, fabricated of mainly InP with a higher thermal

conductance of λ = 0.68 W/cm K, maximum current levels in the range of 100-150 kA/cm² have been reported [32],[33]. For the area of A=50 μm² as used in the above calculation these current densities correspond to an absorbed optical power in the range of 70 mW at 1550 nm (note that usually only a fraction of the optical power is absorbed in p-i-n diodes; the used laser powers are typically much higher than the presented value). Eq. (2.45) predicts 100 mW for InP if limitations by the mesa (Eq. (2.44)) are neglected. For long term use, the optical power must be smaller in order to prevent rapid degradation of the device. This implies very similar values for the maximum optical power for photoconductors and p-i-n diodes. In order to obtain the maximum THz power from the given limit of optical power, three equations have to be optimized simultaneously: RC-roll off, Eq. (2.13), transit-time (CW p-i-n diodes only, Eq. (2.16)) or life time roll-off (CW photoconductors only, eq. [2.20]), and thermal dissipation (summarized by Eq.(2.43)-(2.45)). These equations are not independent. The thermal transport depends either linearly on the device cross section, A ((Eq.2.44)), or on $\sqrt{A}$ (Eq. (2.45)). The RC-roll-off depends on the device cross section and the transport distance (intrinsic layer length, d_i, for p-i-n diodes and electrode gap, w_G, and number of electrodes for photoconductors). The transit-time or life-time depends on the transport distance and the recombination time of the semiconductor. For photoconductors, the thermal dissipation and the life-time roll-off further depend on the gain. The optimization has to be performed for a specific THz frequency, ν_{max}, since transport- and RC roll-off are frequency-dependent. Brown calculated the ideal parameters for photoconductors for both a resonant antenna with R_A=215 Ω and a broadband antenna with R_A=72 Ω in [24]. For operation at 1 THz with a broad band photomixer, the optimum parameters have been determined to w_G = 0.99 μm, τ_{rec}=0.3 ps, A = 73 μm², 8 electrodes (in total). A minimum finger width of 0.2 μm was assumed.

Strategies to improve heat transport from the active area are of key importance for improving the maximum power. This is particularly difficult for devices operated at 1550 nm. The absorption layer is typically made from $In_{0.53}Ga_{0.47}As$, a ternary compound with very low thermal conductance of 0.05 W/cmK [22]. InP, a standard substrate for telecom devices, features a 12 times higher thermal conductance of 0.68 W/cmK [22]. In UTC diodes, the layers with low thermal conductance are kept as small as possible. The n-contact, p-contact and the transport layer are InP layers. Only the absorption layer with a length in the range of 50-100 nm is InGaAs. GaAs-based devices benefit from a relatively high thermal conductance of 0.43 W/cmK [21] as compared to $In_{0.53}Ga_{0.47}As$. Incorporation of AlAs heat spreader layers [34] further improves the performance. Transfer onto a substrate with higher thermal conductance has also been demonstrated [35].

Thermal effects are one of the main constraints of CW systems. For pulsed systems, the thermal power is mainly generated during the pulse duration (typically much below τ_{pls}<1 ps). It scales with the average thermal power, $\bar{P}$, not the peak power, P_{pk}. Thermal limitations can therefore be mitigated by using lasers with low repetition rates, ν_{rep}, since $\bar{P} = P_{pk}\tau_{pls}\upsilon_{rep}$. Electrical limitations, as being discussed next, are more detrimental and challenging for pulsed systems.

2.2.4. Electrical Constraints

Besides thermal limitations, also the carrier transport and other electrical effects show a power-dependence. These effects play a particular role in pulsed operation where a high charge density is generated within the semiconductor but only a moderate average thermal power is dissipated. In order to get insight into the physical limits, some simplifying approximations are necessary in order to get analytical expressions. For exact values, simulations are required, taking the time evolution of the carrier transport into account. Since p-i-n diodes and photoconductors perform very different, the two cases will be treated separately.

2.2.4.1 P-i-n diodes

We will see soon that p-i-n diodes are typically used in CW systems only. Therefore, this section specifically focuses on CW operation. The main results, however, are also valid for pulsed excitation. In order to minimize the transit-time roll-off for CW generation, and to increase the effective dipole length for pulsed operation, carrier transport has to be optimized for operation in the THz range. This is especially the case for THz frequencies where transport at the saturation velocity already causes a roll-off, i.e. $\upsilon_{THz} > (2\tau_{tr}^{sat})^{-1} = v_{sat}/(2d_i)$. For all p-i-n diodes, there exists an optimum transport field since they benefit from ballistic transport: On the one hand, too low fields result in small carrier acceleration, $a = eE_T / m*$. It simply takes too long to accelerate the carriers. On the other hand, too high transport fields (>40 kV/cm, see Fig. 2.6) are detrimental for ballistic transport. For efficient operation, it is of key importance to maintain the ideal transport field throughout the whole structure. The ideal field can either be the built-in field of the diode, E_{bi}, or being fine-tuned with an additional external field, E_{ext}, via a DC bias. However, photo-carriers will alter the local fields within the diode. When optically generated carriers, ($n_{ph}(z)$ electrons and the same amount of holes, $h_{ph}(z)$) are separated in an electric field, $E_{DC}= E_{bi}+ E_{ext}$, they generate a field, E_{ph}, that opposes E_{DC}. According to the first Maxwell equation,

$$\frac{\partial}{\partial x} E_{ph}(z) = -\frac{e[n_{ph}(z) - h_{ph}(z))]}{\varepsilon_0 \varepsilon_r}. \tag{2.46}$$

Subsequently generated carriers experience a smaller acceleration of

$$a(z) = \pm \frac{e}{m*} \left[E_{DC} - E_{ph}(z)\right], \tag{2.47}$$

Where the “+” sign is for electrons and the “-” sign for holes. In the small signal limit of low optical powers (i.e. small n_{ph}(z), $h_{ph}(z)$), the screening field is much smaller than the original accelerating field, $|E_{ph}(z)| << |E_{DC}|$and the small perturbation of the carriers to the constant field E_{DC} can be neglected. For intermediate power levels, the perturbation by the photogenerated carriers can, at least partially, be compensated with an external DC bias as shown in Fig. 2.10 for a photocurrent density of $j=env$=20 kA/cm². A small deviation from the linear band profile is visible but the accelerating field strength is still sufficient throughout the structure. At high power levels, the optical generated carriers can create field kinks in the range of the built-in field, $E_{bi}=E_G/d_i$, *or even larger*. Therefore, the band profile gets strongly distorted, even regions of a flat band profile between the space charge accumulation can occur. In such situations, transport will be heavily restrained, leading to a saturation or even a decline of the THz power with increasing optical power.

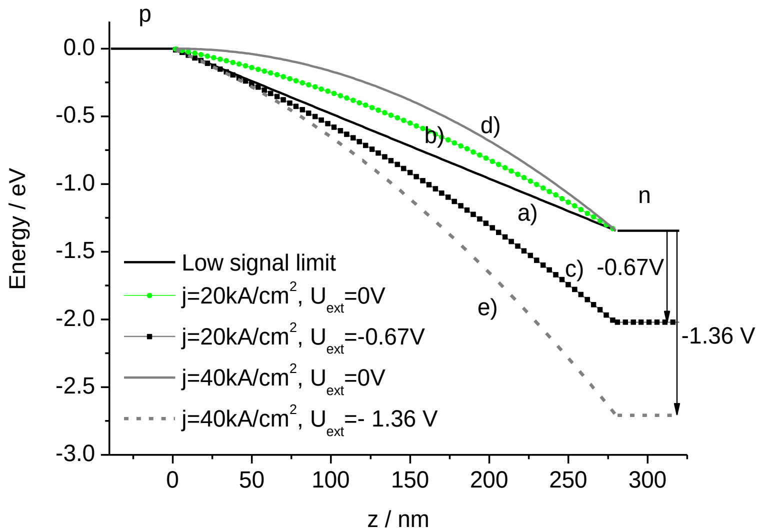

Fig. 2.10: a) Band profile of an ideal UTC p-i-n diode with d_i=280 nm in the small signal limit (black). The band profile is unperturbed and linear. b) Intermediate optical power level: The carriers are mildly screening the built-in field (grey, shown here for 20 kA/cm²), particularly at the p-side of the transport layer. A small external bias can restore the original field strength (dotted, c)). d) High power limit (approximate solution according to Eqs. (2.51) and (2.52), shown for *j*=40 kA/cm²). Without external bias, the carriers screen the built-in field so strongly that a region with very low accelerating fields is formed at the p-side of the intrinsic layer. In this limit, a self-consistent calculation would be required to calculate the exact band profile. A strong reverse bias has to be applied (e) to restore the transport field at the p-side of the intrinsic layer to its original value but the transport field is no longer homogeneous and shows strong warping.

We will estimate the critical current densities and the corresponding optical power where the strong screening sets with a few simplifying assumptions. For exact solutions, self-consistent calculations are required. This goes beyond the scope of this book.

From Fig. 2.6 we can extract that efficient ballistic transport can be maintained for fields within $E_{pin} = E_{bal}^{opt} \pm \Delta E_{bal} = E_{bal}^{opt} \pm 10$ kV/cm, where E_{bal}^{opt} is the optimum ballistic field. E_{bal}^{opt} is slightly dependent on the intrinsic layer length and on the material of the transport layer, with typical values around E_{bal}^{opt}=20 kV/cm. A variation of the electric field *within* the intrinsic layer cannot be compensated with an external bias since the external field just adds to the internal field. In order to allow for analytical solutions, the p-i-n diode is subject to the following assumptions:

- Absorption takes place in a very narrow area close to the p-contact (ideal UTC diode). Holes remain stationary and only electrons move.
- For CW operation, the carriers within one THz wave are assumed to be generated instantaneously i.e. the CW signal is approximated by a pulse train instead of a cosine shape. For pulsed operation, all carrier shall be generated at once (i.e. the pulse duration is much shorter than the transit-time).

For a device operated at the transit-time 3dB frequency where only a single electron bunch propagates, the electron density that has propagated to a distance *s(t)* after generation at time *t* is

$$n(z) = \frac{\bar{j}_{bal}^{\max}\tau_{tr}}{e}\,\delta(z - s(t))\,, \tag{2.48}$$

where $\bar{j}_{bal}^{\max}$ is the maximum current density for ballistic transport that will be derived in the following. Since holes are stationary, they do not produce any current. The induced field kink according to Eq. (2.46) is

$$\Delta E_{Ph}(z) = \frac{\bar{j}_{bal}^{\max}\tau_{tr}}{\varepsilon_0\varepsilon_r}\,. \tag{2.49}$$

For a device with a transit-time 3 dB frequency of $\upsilon_{tr}^{3dB} = 1/2\tau_{tr} = 1$ THz, and a maximum kink of $\Delta E_{Ph}(z) = 10$ kV/cm in order to achieve ballistic transport before and after the kink, the maximum current density for ε_r=13 is $\bar{j}_{bal}^{\max}$=23 kA/cm². For the 50 μm² device that was used for the estimates regarding the thermal limitations, the maximum current is 11.5 mA, and the *absorbed* optical power for operation at 1550 nm is 9.2 mW. For current densities above $\bar{j}_{bal}^{\max}$, only part of the transport region can be covered ballistically. This increases the transit-time of the carriers and reduces the transit-time 3 dB frequency. Since we assumed that all carriers of one THz wave are generated at once, this value represents only a lower limit. Continuous carrier generation will lead to slightly higher values.

For low frequencies, where transport at the saturation velocity is sufficient in order to achieve roll-off free operation, the THz power will still increase quadratically with the optical power. The screening can be compensated with an external bias as long as this bias does not exceed the break-down voltage of the semiconductor. The latter case is the ultimate power limit for the photomixer. The exact photo-induced screening of the field in the intrinsic layer strongly depends on the transport properties. The maximum current density will, however, certainly be higher than $\bar{j}_{bal}^{\max}$. In order to provide an analytical estimate for the maximum current density (optical power), we assume that the majority of the transport takes place with the saturation velocity, v_{sat}, and the device is operated above its transit-time 3 dB frequency under CW operation in the quasi steady state such that the time-dependent quantities can be replaced with their time-averages (indicated by bars). The following calculation is not valid for pulsed operation, since there is no steady state. The space charge that builds up during carrier propagation can relax slowly between the pulses, recovering the original, band diagram without photogenerated carriers. For the case of pulsed excitation, time dependent quantities would have to be used. Since p-i-n-diodes are typically used in CW experiments, we will restrict the discussion on the CW case and use again the case of an ideal UTC diode with a very narrow absorption region close to the p-contact. The average carrier density in the device is given by the continuity equation,

$$e\bar{n}(z) = \bar{j}/v_{sat} = const\,. \tag{2.50}$$

The average photo-generated bias at position z according to the first Maxwell equation is

$$\bar{U}_{Ph}(z) = -\iint \frac{en(z'')}{\varepsilon_0 \varepsilon_r} dz'' dz' = -\frac{nez^2}{2\mathrm{v}_{sat}\varepsilon_0\varepsilon_r} = -\frac{\bar{j}z^2}{2\mathrm{v}_{sat}\varepsilon_0\varepsilon_r}, \tag{2.51}$$

as illustrated in Fig. 2.10. For the boundary condition $j=const$ (Eq. (2.50)) an external bias has to be applied to compensate for the photo-voltage. We allow for a small additional external bias, U_{ext} for fine-tuning the field in the intrinsic layer in order to compensate the photo bias and to allow for a minimum transport field, E_{min}. The external DC bias becomes

$$U_{ext} = U_0 + \bar{U}_{Ph}(d_i) = U_0 - \frac{\bar{j}d_i^2}{2\mathrm{v}_{sat}\varepsilon_0\varepsilon_r}, \tag{2.52}$$

where U_0 is the bias at low optical powers. The total (average) field in the transport layer is

$$E_{tot}(z) = E_{bi} + E_0 - \frac{\partial}{\partial z}\bar{U}_{Ph}(z) = E_{bi} + E_0 + \frac{\bar{j}z}{\mathrm{v}_{sat}\varepsilon_0\varepsilon_r}, \tag{2.53}$$

with E_{bi} the built-in field and $E_0=U_0/d_i$. The field is lowest right at the p-contact, where the carriers are generated, and highest right at the n-contact, $z=d_i$. In order to sustain efficient carrier transport, the field inside the diode should not fall below a minimum value of E_{min}= 5 kV/cm. Below this value, carriers are too slowly accelerated and may not even reach the saturation velocity. By setting $E_{tot}(0)=E_{min}$, Eq. (2.53) yields $E_0= E_{min}-E_{bi}$ and

$$U_0 = d_i(E_{bi} - E_{\min}). \tag{2.54}$$

Note that typically U_0>0, i.e. in the small signal limit, even a small forward bias can be tolerated. On the other hand, the field must not exceed the break-down field of the semiconductor. For InP (InGaAs), the break-down field is E_B=500 kV/cm (200 kV/cm) [20]. By setting $E_{tot}(d_i)=E_B$ in Eq. (2.47) the maximum current is

$$\bar{j}_{Ph}^{\max}(E_{ext}) = \frac{\mathrm{v}_{sat}\varepsilon_0\varepsilon_r(E_B - E_{bi} - E_0)}{d_i} = \frac{\mathrm{v}_{sat}\varepsilon_0\varepsilon_r(E_B - E_{\min})}{d_i}. \tag{2.55}$$

For a device with an InP transport layer with an InGaAs absorption region with (safe) operation at E_B=200 kV/cm, a band gap energy of the transport layer of E_G=1.34 eV, ε_r=12.5, $\mathrm{v}_{sat} = 1.5 \cdot 10^7$ cm/s [19] and an intrinsic layer length of d_i = 280 nm the maximum current is $\bar{j}_{\max} =$ 115 kA/cm². This current density is 5 times higher than the maximum current density for ballistic transport. The assumption that the carriers mainly move with the saturation velocity is satisfied. If there is still a ballistic contribution, the maximum current can be somewhat higher since $\bar{j}_{\max} \sim \mathrm{v}_e$. Substituting U_{bal} from Eq. (2.54) and the maximum current for Eq. (2.55) into Eq. (2.52), the required external bias is U_{ext}=-1.6 V. These values are in excellent agreement with data found in the literature [32] where $\bar{j}_{\max} =$ 60-150 kA/cm² (area 13 μm², maximum current 8-20 mA) and a DC bias between -1.5 V and -2 V are reported. Eq. (2.55) shows that the maximum current scales with the inverse intrinsic layer length. Higher current densities can be achieved with shorter intrinsic layers without electrically destroying the device. This is also beneficial for the transit-time roll-off but deteriorates the RC optimization. However, the above approximations of using the average values are only valid if the device is operated far above the transit-time 3 dB frequency, requiring rather thick intrinsic layers. For operation below the transit-time limit, a rigorous simulation using the time-dependent quantities must be performed. Further cases of other types of p-i-n diodes have been calculated in [18].

In order to reduce the photo-induced field according to Eq. (2.53), the transport layer can be slightly n-doped. The positive space charge of the ionized donors results in a band bending opposite to that of the free electron space charge and less external bias is required to maintain the transport field in the intrinsic layer. An example is illustrated in Fig. 2.11.

For comparison of electrical to thermal limitations, we use the same geometry as in the last section. The maximum optical power for a 50 μm² device with an electrically limited current density of 115 kA/cm² is P_{Abs}=75 mW. This power level is similar to the maximum thermal power (38-80 mW have been estimated). CW operated p-i-n diodes with intrinsic layers in the range of 200-300 nm are therefore both electrically and thermally limited at the same time with little room for improvement. For pulsed operation, however, electrical limitations dominate the performance. Much shorter intrinsic layers would be required to achieve both electrically and thermally limited performance. However, this would degrade the RC roll-off drastically. Therefore, p-i-n diodes are mostly used in CW applications.

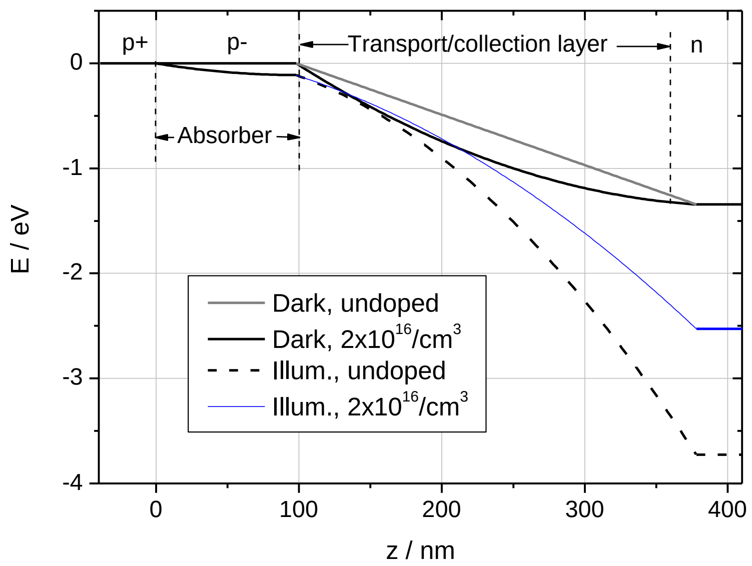

Fig. 2.11: Approximate conduction band diagram of a UTC diode with an absorber doping of $p^-=10^{17}$/cm³, and a transport layer doping of $n^-=2\text{x}10^{16}$ /cm³. The band diagram is depicted for an optically generated current density of 80 kA/cm². The curvature of the transport layer due to photo-generated carriers under strong illumination is much smaller as compared to the undoped case. The doping also substantially reduces the required DC bias for maintaining the transport field at the beginning of the transport layer (at the p^--layer). The self-biasing effect in the p^- region is also shown.

So far, we treated an idealized p-i-n diode with a very narrow absorption region (of width w_A), much narrower than the transport layer. In real devices, this is not practicable since the absorbed optical power (and, consequently, the photocurrent) would be very small according to Lambert-Beer's law (see Eq. (2.10)). As an example, even a 200 nm absorber layer with an absorption coefficient of α=8000 cm^{-1} (a typical value for InGaAs) absorbs a laser power of only $P_{abs}/P_L = 1-\exp(-\alpha w_a) = 14.8\%$, if no power was reflected. However, a 200 nm thick absorber layer cannot be considered as very narrow compared to a 280 nm transport layer. The thickness of the absorber must be thinner in order to prevent large hole transport lengths, which would deteriorate the transport performance of the device. A further problem is the structure of the absorber layer. As discussed in Section 2.3.1, in terms of thermal conduction, InP is preferable as compared to InGaAs. However, InP does not absorb 1550 nm light. InGaAs layers have to be used for the absorbing layer. Therefore, many THz p-i-n diodes consist of an InGaAs absorber layer with a length in the range of 50-120 nm, followed by an InP transport layer in the range of 200-300 nm [32],[36],[37]. A key challenge in sample growth is the transition from InGaAs to InP, particularly concerning the exchange the group V element (As, P). Smooth transitions (such as graded layers) are difficult to grow, therefore most diodes with InP transport layers consist of a sequence of 2-3 $InGaAs_yP_{1-y}$ layers. Each transition results in a step in the band edge that gives rise to carrier accumulation and scattering. In order to reduce the step in the conduction band, the transition layers are slightly n-doped [37] in most cases. Since the InGaAs absorber is at the p-side of the junction, the n-doping could result in formation of a junction with a large field drop right in the absorber layer instead of the transport layer. Therefore, the InGaAs absorber layer must be p$^-$-doped and the transition length should be kept short. The p$^-$-doping results in very low accelerating fields in the absorber layer (see Fig. 2.7). This deteriorates the transit-time performance since the electron transit time from their point of generation to the transport layer through the absorber layer can be very long if it is diffusion-dominated. For pure diffusion, the transit-time through the absorber layer is [38]

$$\tau_A^{diff} = \frac{w_A^2}{2D} + \frac{w_A}{\mathrm{v}_{th}}, \tag{2.56}$$

where $D=k_B T\mu_e/e$ is the diffusion constant and v_{th} is the electron thermal velocity. For an average drift length of w_A=50 nm (total absorber length 100 nm), the diffusion transit-time through the absorber is in the range of $\tau_A^{diff} \approx 0.5\,\mathrm{ps}$, depending on the doping level which alters the carrier mobility. The same accounts for holes. Fortunately, holes are much slower than electrons and generate a space charge field in the absorber layer similar to Eq. (2.51) and Eq. (2.53), but with opposite sign. The amplitude of the space charge field generated by stationary holes, however, is much smaller due to the p$^-$ doping of the absorber that is usually higher than the photogenerated carrier density. It is illustrated in Fig. 2.11. The small space charge field due to holes supports field-driven acceleration of the electrons in the p$^-$ -layer towards the transport layer. For high optical powers, the acceleration can be high enough to allow for drift-limited transport [38]. Still, the average transit-time through the InGaAs absorber layer, τ_A, increases the total transit-time, $\tau_{tr} = \tau_A + \tau_T$, where τ_T is the transit-time through the InP transport layer.

In order to mitigate the dilemma between increased absorption (requiring a long absorber) and small transit-time (requiring a short absorber), the propagation direction of the laser light can be adapted. So far, we considered direct illumination from the top. Several groups employ a waveguide design, where the absorption takes place along the p-i-n diode's lateral dimension [37],[39]. Narrower absorption regions can be used by elongated diodes, still achieving large optical responsivities in the range of 0.36 A/W [37] (the maximum responsivity at 1550 nm is $e/h\nu$=1.25 A/W).

2.2.4.2 Photoconductors

(a) Space charge screening

For a short lifetime material, carriers are trapped soon after their generation. The average distance an electron or hole can move with a drift velocity v_{Dr} before it is trapped is

$$l_D = v_{Dr}\tau_{rec}, \tag{2.57}$$

as illustrated in Fig. 2.12. The maximum drift velocity is the saturation velocity, v_{sat}. However, the mobilities for electrons in LTG GaAs are with values around 400 cm²/Vs much smaller than in undoped GaAs. At high optical fluences, the large amount of optically generated carriers can additionally result in increased carrier-carrier scattering reducing the mobility [40]. To accelerate electrons to the saturation velocity, fields in the range of 25 kV/cm are necessary in LTG-GaAs and it takes already tens of fs. In the following calculation, we will use $v_{Dr}=v_{sat}$. The results will only be upper limits for space charge effects. We will first treat the CW case.

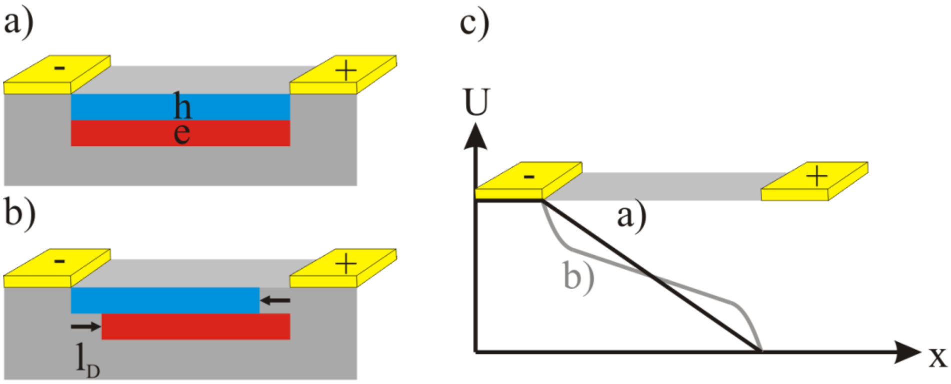

Fig.2.12: Illustration of the screening effect in photoconductors for a short pulse. a) Electron and hole distribution right after their generation. For better visibility, electron and hole clouds are vertically offset. b) The charge clouds can only move a length of l_D before they get trapped. Carriers at the contact are withdrawn. In the central part of the structure, there are both electrons and holes available. The carriers can quickly recombine without leaving any net charge. c) The external bias is mainly screened close to the contacts, lowering the effective transport field throughout most of the structure. The electric field (slope in c)) right at the contact is higher than the average transport field.

CW operation

A recombination time of τ_{rec}~200 fs and transport with v_{sat} results in a dipole length of l_D~ 20 nm. Electron and hole clouds are displaced as illustrated in Fig 2.12 b). The electric field in the gap is

$$E_{tot}(x) = \begin{cases} E_0 - \dfrac{en_0}{\varepsilon_0\varepsilon_r}x & for \quad 0 \le x < l_D \\ E_0 - \dfrac{en_0}{\varepsilon_0\varepsilon_r}l_D & for \quad l_D \le x < w_G - l_D \\ E_0 - \dfrac{en_0}{\varepsilon_0\varepsilon_r}(w_G - x) & for \quad w_G - l_D \le x < w_G \end{cases} \tag{2.58}$$

with E_0 the field right at the electrode. For CW, we assume that the carrier density, n_0, is the average space charge carrier density at the electrodes and is time-independent. The external bias source can deliver a constant average bias of U_{DC} to the electrodes, maintaining the average potential. The boundary conditions are therefore chosen such that $U_{tot} = \int_0^{w_G} E_{tot}(x)dx = U_{DC} = E_{DC} / w_G$, with E_{DC} the unperturbed field in the gap. This yields for the field at the electrodes $E_0 = E_{DC} + \frac{en_0}{\varepsilon_0\varepsilon_r}\frac{l_D}{w_G}(w_G - l_D) \approx E_{DC} + \frac{en_0}{\varepsilon_0\varepsilon_r}l_D$. The field in the gap center (Eq. (2.58), center) is reduced by screening due to photo-generated carriers to

$$E_{scr} = E_{DC} - \Delta E_{Ph} = E_{DC} - \frac{n_0 e}{\varepsilon_0\varepsilon_r}\frac{l_D^2}{w_G}, \tag{2.59}$$

The total screened bias at the electrodes is

$$\Delta U_{ph} = \frac{n_0 e l_D^2}{\varepsilon_0\varepsilon_r}. \tag{2.60}$$

For CW operation, it is necessary to clearly distinguish between trapping and recombination. Historically, the *trapping time* of carriers in photoconductors is termed the *recombination time*, τ_{rec},. Since the carrier is capturend, it does not contribute any more to the current andthe trapping time enters the life-time roll-off Eqs. (2.20) and (2.21). However, this does not necessarily mean that the carrier has already *recombined* with another carrier of opposite sign. Sufficiently far away from the electrodes, the photogenerated electron and hole densities are equal. Therefore, fast recombination due to alternate electron and hole capture by a sufficiently large number of deep traps is a very fast process. However, close to the electrodes within a drift length l_D the carriers of opposite sign are missing and the deep defects can no longer act as recombination centers but only as traps. Once a trap is occupied, it cannot trap more carriers of the same charge . But these carriers will remain trapped for very long times compared to the recombination time: thermal "detrapping" requires a thermal activation energy of about ½E_G to get back into the respective band. Relaxation or detrapping times, τ_{DT}, between 100 ps [41] and several ns have been reported [42]. Therefore, under CW conditions, nearly all the recombination centers within the drift length l_D from the electrodes will become charged traps with space charge density $-en_0$ and $+en_0$, respectively. The number of deep traps, n_0, can largely exceed the photogenerated electron/hole density created on the recombination time scale, i.e. $n_0 >> \alpha P_{abs} \tau_{rec}/(h\nu A)$. This justifies the initial assumption of a time-independent, averaged space charge carrier density, n_0. But the number of trapped charges, n_0, cannot exceed the number of trap states which is estimated to be in the range of $2\text{x}10^{18}$ /cm³ [43] roughly representing an upper limit to the space charge. This value, however, strongly depends on the growth and annealing conditions of the photoconductor and can vary within a wide range. A trap density of $2\text{x}10^{18}$ /cm³ leads to a reduction of the field strength of ΔE_{Ph}=5.5 kV/cm for a gap of 2 µm and l_D=20 nm, a screened bias of ΔU_{ph}=1.1 V, and an increase of the field at the electrode of $\Delta E_0 = E_0 - E_{DC}$=550 *kV/cm* which is in the range of the break-down field strength. In summary, bias field screening for CW excitation is small, but space charge effects can cause early break-down close to the electrodes due to drastic increase of the local field to values clearly above those derived from gap spacing and DC bias.

A calculation of the maximum number of optically generated carriers (and, therefore, the maximum optical power for CW generation) requires precise knowledge of the de-trapping time and may require a dynamic calculation. This calculation goes beyond the scope of this book.

Pulsed operation

Under pulsed operation the material can relax between pulses such that only the carriers generated in a single pulse contribute to the space charge. There is no accumulation due to long detrapping times, as long as the repetition rate of the laser is slower than the inverse detrapping time, τ_{DT}. The carrier generation and separation happens on the (sub-) ps time scale without formation of a constant, average space charge carrier density, n_0 at the electrodes. The external source that provides the bias, U_{DC}, will be too slow to react on the THz time. Various capacitances, inductances and resistances (including the device resistance) hinder supplying charges from the bias source that compensate photogenerated carriers on such a short time scale – in contrast to the CW case where it needed to supply an average bias only. It is therefore inappropriate to assume a constant potential of U_{DC} at the electrodes. It is more realistic to assume that the constant DC bias is screened by optically generated carriers, leading to a reduction of the electrode potential during the THz pulse. Therefore, Eqs. (2.58)-(2.60) need modifications and have to be calculated time-dependent. In order to get an estimate of the maximum screening effects, we assume an extremely short optical pulse and quick charge trapping in order to calculate the fields in the junction right after generation and trapping where screening effects are maximal. The electric field in the gap becomes

$$E_{tot}(x) = \begin{cases} E_{DC} - \dfrac{en_0}{\varepsilon_0 \varepsilon_r} x & for \quad 0 \le x < l_D \\ E_{DC} - \dfrac{en_0}{\varepsilon_0 \varepsilon_r} l_D & for \quad l_D \le x < w_G - l_D \\ E_{DC} - \dfrac{en_0}{\varepsilon_0 \varepsilon_r}(w_G - x) & for \quad w_G - l_D \le x < w_G \end{cases} \tag{2.61}$$

with $E_{DC} = U_{DC}/w_G$. Here, n_0 is the optically generated carrier density per pulse. The field in the gap center is reduced by screening due to photo-generated carriers by

$$\Delta E_{Ph} = \frac{n_0 e}{\varepsilon_0 \varepsilon_r} l_D \, , \tag{2.62}$$

The electrode potential is screened by

$$\Delta U_{ph} = \frac{n_0 e l_D}{\varepsilon_0 \varepsilon_r} (w_G - l_D) \, . \tag{2.63}$$

Comparing the screened field of Eq. (2.62) with that of p-i-n diodes (with $z=d_i$ and $j=en_0v_{sat}$) in Eq. (2.53) of $\Delta E_{ph} = \frac{n_0 e d_i}{\varepsilon_0 \varepsilon_r}$, the maximum screened field is a factor of d_i/l_D~10 smaller for photoconductors, where d_i is the transport length for p-i-n diodes. Most pulsed systems therefore use photoconductors instead of p-i-n diodes. Much higher carrier densities, n_0, are possible in pulsed operation before reaching any space charge limit. For the same values as above (l_D=20 nm , w_G=2 μm, n_0=2x10^{18} /cm³), however, the screened bias is ΔU_{ph}=110 V, i.e. a factor of $l_D/(w_G-l_D)$=100 larger than for the CW case. This value is larger than typical biases of 30-60 V used for a gap width of 2 μm. Therefore, saturation certainly occurs at such high carrier concentrations. But bias field screening saturation is a dynamic process: the space charge builds up on a time scale of τ_{rec}. This is the same time scale where THz radiation is efficiently emitted. In low field regions, carriers cannot reach the saturation velocity any more, resulting in a slower response and a reduced spectral width. Therefore, not only the THz amplitude will be altered by bias field screening but also the spectral shape. The change of the THz spectra requires simulations [44]. The maximum bias and break-down voltage, however, can be estimated by a quasi-static approach since trap de-screening takes much longer than trapping. The bias due to space charge and the space charge field are given by Eqs. (2.61) and (2.62). In contrast to CW operation, $n_0 = \alpha E_{pls} / (h\upsilon A)$ is the carrier concentration generated by one THz pulse. The external applied bias must compensate the space charge field in Eq. (2.62). For sustaining the transport in the gap, a minimum field of about 25 kV/cm is necessary. Nowhere in the gap, particularly close to the electrodes, the break-down voltage (500-1000 kV/cm for LTG-GaAs [24], [45]) must be exceeded. This leads to a maximum carrier density of

$$n_0^{\max} \approx \frac{\varepsilon_0 \varepsilon_r}{e l_D} (E_B - E_{\min}) \tag{2.64}$$

For τ_{rec}=200 fs, v_{sat}=10^7 cm/s, and E_B=1 MV/cm the maximum optical carrier density is n_0=3.6x10^{18} cm^{-3} (pulse energy for GaAs of 40 pJ (for A=50 μm², or fluences of 80 μJ/cm²). On the one hand, this calculation is fairly optimistic: Carriers are generated within a thickness of 1/α in the semiconductor. But the electrodes are planar. Carriers from the depth of the photoconductor have to drift towards the electrodes, increasing the local space charge density and reducing the maximum pulse energy. On the other hand, space charge screening will reduce the local field inside the gap, therefore reducing the carrier velocity and the dipole length, l_D. In turn, higher optical densities are allowed according to Eq. (2.64). The device saturates, the THz pulses become wider.Estimates on the trap state density are in the same order of magnitude (2x10^{18} /cm³ [43]). The photoconducting material will not be able to trap more charges, resulting in longer effective trap times and temporal broadening of the pulse. The calculated order of magnitude for saturation is in excellent agreement with experimental data [40],[43],[46].

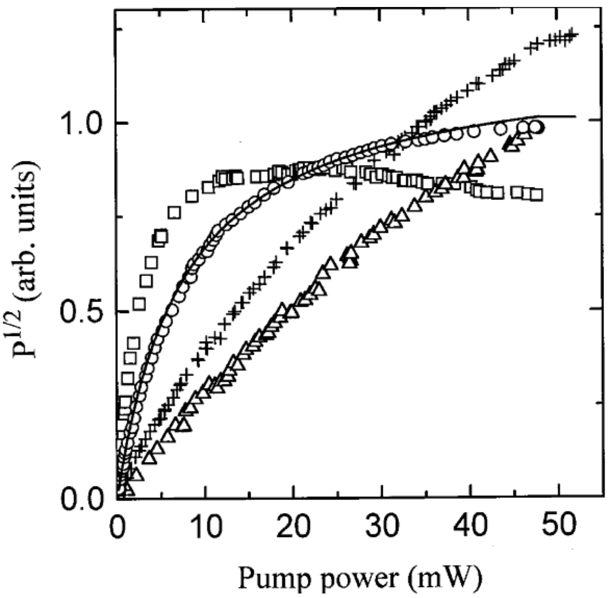

Fig. 2.13: Integrated powers for pulsed operation (ν_{rep}=82 MHz, τ_{pls}=80 fs) of an LTG-GaAs photomixer (A~100μm²) equipped with a dipole antenna (open circles) at E_{DC}=20 kV/cm, and a SI GaAs photomixer with the same antenna (open squares) at E_{DC}=36 kV/cm. The other graphs represent data with LTG GaAs using other types of antennas. A linear increase with the square root of the pump power represents the non-saturated regime. Despite the 80% higher bias, the SI GaAs saturates earlier (fluence~25 μJ/cm² compared to ~100 μJ/cm² for LTG-GaAs). Saturation occurs probably due to both bias screening and radiation field screening. Under similar biases and excitation conditions the order of magnitude of the emitted power was the same. [Request Copyright: Tani et al., Appl. Opt. 36, 7853 (1997)]

For a photoconductor without traps (such as SI GaAs), the carriers drift towards the contacts due to the applied DC bias. This is similar to a p-i-n dode with absorption throughout an intrinsic layer of length w_G. However, SI GaAs is very inefficient as CW source due to the extremely long transit-time, resulting in a severe roll-off, and the high electrical power consumption, resulting in early thermal break-down. In pulsed systems, SI GaAs has proven to be competitive to LTG GaAs. Thermal limitation is alleviated since practically no heat is generated between pulses where the device returns to its high resistive dark state. Due to a sharp onset of the current when the pulse illuminates the sample, a broadband spectrum is obtained as illustrated in Fig. 2.9. However, due to a lower break-down voltage of the order of 300 kV/cm as compared to 500-1000 kV/cm for LTG GaAs), the maximum bias voltage is lower. In addition, the carriers drift longer since they are not trapped, resulting in larger space charge effects. The devices saturate earlier than LTG GaAs devices. An early experimental comparison of SI GaAs to LTG GaAs from ref. [46] is shown in Fig. 2.13.

(b) Impedance matching and radiation field screening

If an antenna is used to emit the radiation resulting from the changes of the photocurrent generated by the device, the radiation impedance, $Z_A=R_A+iX_A$, and the impedance matching to the photoconductor determine the radiated power. The radiated THz power for CW operation is given by [24],[47]

$$P_{THz} = \frac{1}{2} I^2 \frac{G_A(\omega)}{\left(G_A(\omega)+G_P\right)^2 + \left(B_A(\omega)+\omega C\right)^2} \tag{2.65}$$

with $G_A(\omega) = \Re\left\{Z_A^{-1}(\omega)\right\}$ and $B_A(\omega) = \Im\left\{Z_A^{-1}(\omega)\right\}$, C is the capacitance and $G_P = I/U_{DC}$ is the conductance of the device. Note that the emitted THz power in Eq. (2.65) gets maximal for a fixed radiation resistance for $G_P \to 0$. For CW operation, the source resistance of p-i-n diodes can be in the range of the radiation resistance (typical values are between 27 Ω and 100 Ω for an antenna on a GaAs-air or InP-air interface) and impedance matching is possible [48]. The resistance of photoconductors is much higher than the radiation resistance of any practical antenna for CW operation. Typical dark resistances for GaAs-based devices are in the MΩ–GΩ range. Even with strong pumping, it is difficult to get the device resistance below ~1 kΩ, with very few exceptions (such as in ref. [49]). The conductance of the device under CW operation, $G_P << G_A(\omega)$, can be omitted in Eq. (2.65). For low and intermediate power levels, this remains the same for pulsed operation. For highest optical power levels, however, the conductance may become higher than the antenna admittance $G_A(\omega)$. This decreases the THz power according to Eq. (2.65). The antenna is short circuited by the device. However, Eq. (2.65) is difficult to use in pulsed operation in the limit of low device conductance: The frequency dependence of the excitation, $I(\omega)$~$P_L(\omega)$ is contained in the current. The device conductance $G_P(t)$ is time varying, e.g. by trapping of the carriers. Its Fourier transform shows also a frequency-dependence. A similar approach as in Eq. (2.32) could be used. In order to estimate the power level where G_P becomes comparable to the antenna admittance and a simplified approach can be used. For an exciting optical pulse that is much shorter than τ_{rec}, the instantaneous conductivity of a photoconductor right after absorption of the optical pulse is

$$G_P \approx e n_0 \mu \cdot \frac{N l_y}{\alpha w_G}, \tag{2.66}$$

for a finger structure with fingers of length l_y and N gaps of width w_G. α is the absorption coefficient, and

$$n_0 \approx \alpha \frac{E_{pls}/N}{h\upsilon w_G l_y} \tag{2.67}$$

with an absorbed pulse energy of E_{pls}. Substituting Eq. (2.67) into Eq. (2.66) yields

$$G_P \approx \mu \frac{e E_{pls}}{h\upsilon} \cdot \frac{1}{w_G^2}. \tag{2.68}$$

For an antenna with a frequency-independent radiation resistance of R_A=72 Ω (a self-complementary broadband antenna, e.g.), negligible reactance, X_A, a mobility of 400 cm²/Vs, $h\nu$=1.5 eV (830 nm,LTG GaAs) and a gap width of 2 µm, the instantaneous device resistance becomes equal to the radiation resistance of the antenna at an optical pulse energy of 2.1 pJ. This is more than an order of magnitude smaller than the laser power where bias field screening becomes apparent as derived in the previous section for a 50 µm² device. For SI GaAs, the mobility can be up to a factor of 20 higher than for LTG-GaAs, resulting in impedance matching at a pulse energy of only 0.1 pJ. Eq. (2.68) scales inversely quadratic with the gap width. It is therefore reasonable to use larger gaps for pulsed operation, in order to allow for higher optical powers and consequently higher THz powers. On the one hand, larger gaps reduce the photoconductive gain, $g=\tau_{rec}/\tau_{tr}$, which reduces the current fed to the antenna (Eq. (2.21)). On the other hand, larger gaps show less capacitance, improving the RC performance paticularly above 1 THz, compensating the smaller current. For a single gap of $w_G=l_y=7$ µm (area~50 µm²), impedance matching is achieved at 50 pJ absorbed energy for LTG GaAs (optical fluence of 100 µJ/cm²), corresponding to an optical carrier density of $n \approx 4.2 \cdot 10^{18}$/cm³. In this range, also trap saturation may influence the device performance in LTG-GaAs, since the trap density is estimated to be in the range of $2\text{x}10^{18}$ /cm³ [43]. The carrier density (pulse energy) for impedance matching does not represent a limit. At higher pulse energies, the device impedance will be lower than the antenna impedance right after absorption of the optical pulse. It will cross the point of impedance matching within the time scale of the recombination time, and become highly resistive again afterwards. Broadening of the pulse was reported [43] and a sub-linear increase of the emitted THz field with increasing fluence [40]. In many cases, τ_{rec} is in the same range as the pulse duration, τ_{pls}, such that many carriers are trapped before the optical pulse is over. The presented values are therefore underestimates.

At very high optical power levels where $G_P>>G_A$, it will not make sense to further increase the optical power, since the device will saturate. Eq. (2.65) becomes in this limit $P \approx \frac{1}{2} I^2 \frac{G_A(\omega)}{G_P^2} = \frac{1}{2} G_A(\omega) U_{DC}^2 \rightarrow 0$ since $G_A(0\ Hz)=0$ and U_{DC} possesses only the DC component. The frequency dependencies of current and conductance cancel, there is no noticeable AC modulation of the current fed into the antenna any more, and no power will be generated during the time where $G_P(t)>>G_A$. Note, however, that increasing the bias, U_{DC}, still quadratically increases the THz power (particularly during pulse times where $G_P(t) \leq G_A$). This is name-giving for the device: "photoconductive switch". The laser pulse modulates the resistance of the photoconductor from highly resistive to low-ohmic and therefore switches the current due to the external DC bias on and off.

A term that is more frequently used to describe the saturation with respect to increasing optical power is *radation field screening*. At high fluences, the emitted THz field can reach the same order of magnitude as the accelerating DC field, $E_{DC}=U_{DC}/w_G$, supplied to the electrodes. In the following, we will show that radiation field screening is indeed described by Eq. (2.65). For simplicity, we neglect reactances of both the antenna and the device and discuss only the 1D problem of carrier transport along the x-direction between the electrodes where all z-dependencies have been integrated. We further assume long electrodes without any y-dependence on fields and currents. Due to the induction law, the THz field reduces the accelerating field, [50],[51]

$$E_{loc}(x,t) = E_{DC} - \Delta E_{Ph}(x,t) - E_{THz}(x,t), \tag{2.69}$$

where $\Delta E_{Ph}(x,t)$ is the (time dependent) screened bias by charges in the photoconductor according to eq. (2.62), and $E_{THz}(x,t)$ is the radiated THz field that back-acts on the carriers. The bias field screening by $\Delta E_{Ph}(x,t)$ will be neglected since it was discussed in the last section. The radiated field is proportional to the time derivative of the 2D photocurrent density, $E_{THz}(x,t) \sim \partial / \partial t \;\; j^{(2D)}(x,t)$ (with $j^{(2D)}$ in units A/m due to z- integration). The current density is x-dependent since we have to calculate the total displacement current which is the sum of all currents generated within the device. The 2D current density can be understood as an effective surface current. In the frequency domain, this reads

$$E_{THz}(x,\omega) = \beta i\omega j^{(2D)}(x,\omega) \tag{2.70}$$

where β is a proportionality constant defined by the radiation resistance of the antenna, $Z_A(\omega) = U_{THz}(\omega) / I_{THz}(\omega) = \left|\int E_{THz}(x,\omega)dx\right| / \left|\int j^{(2D)}(x,\omega)dx\right| = i\beta\omega$, where $j_A^{(2D)}(x,\omega)$ is the surface current density generated by the device. The average 2D current density is related to the local accelerating field by $j^{(2D)}(x,\omega) = G_P(x,\omega)E_{loc}(x,\omega)$. The radiated field at the antenna in Eq. (2.70) can then be expressed in terms of the local field as

$$E_{THz}(x,\omega) = Z_A(\omega)G_P(x,\omega)E_{loc}(x,\omega) \tag{2.71}$$

Substituting the local field from Eq. (2.67) into Eq. (2.71) yields

$$E_{THz}(x,\omega) = \frac{Z_A(\omega)G_P(x,\omega)E_{DC}}{1+G_P(x,\omega)Z_A(\omega)} = \frac{Z_A(\omega)\, j_{id}^{(2D)}(x,\omega)}{1+G_P(x,\omega)Z_A(\omega)}, \tag{2.72}$$

with $G_P(x,\omega)E_{DC} = j_{id}^{(2D)}(x,\omega)$, the ideal current density generated by the device with $\int j_{id}^{(2D)}(x,\omega)dx = I(\omega)$. For a device conductance comparable to the inverse radiation resistance, the current fed into the antenna in order to generate THz radiation is reduced by the denominator in eq. [2.72]. Replacing the radiation resistance by the admittance, the THz field becomes

$$E_{THz}(x,\omega) = \frac{j_{id}^{(2D)}(x,\omega)}{G_A(\omega) + G_P(x,\omega)} \tag{2.73}$$

Using $P_{THz}(\omega) = \frac{1}{2} G_A(\omega) \left|\int E_{THz}(x,\omega)dx\right|^2$ and replacing the local conductance, $G_P(x,\omega)$, by the externally accessible value of the lumped element, $G_P(\omega)$, yields the impedance matching formula in Eq. (2.62), however, without imaginary parts since they were neglected in this calculation. These can easily be accommodated in Eq. (2.73) by replacing $G_P(x,\omega)$ and $G_A(\omega)$ by their respective complex quantities.

Eq. (2.72) is frequently used to describe radiation field screening for large area or large aperture emitters [25],[52] where the spatial dependence can be omitted for homogeneous illumination. In large aperture emitters, the carriers situated at a semiconductor-air interface directly emit the THz power into free space. The radiation resistance therefore has to be replaced by the wave impedance, $Z_0/(1+n)$, where n is the refractive index of the substrate. Further, the lumped element conductance must be replaced by the surface conductivity (i.e the conductivity integrated over depth, z), $\sigma^{(2D)}$, since the device cannot be considered as a lumped element but rather as an array of distributed emitters (see also Chapter 3 6.2). The current responsible for radiation reads [25]

$$j^{(2D)}(t) = \frac{\sigma^{(2D)}(t)E_{DC}}{1+\dfrac{\sigma^{(2D)}(t)Z_0}{1+n}} \tag{2.74}$$

The numerator is the ideal current density. Since the THz power is proportional to $P_{THz} \sim [j^{(2D)}(t)]^2$, radiation field screening reduces the THz power as $\eta_{RFS} = \left[1+\sigma^{(2D)}Z_0/(1+n)\right]^{-2}$.

From large area emitters based on SI GaAs, fluences in the range of ~1 μJ/cm² for accelerating fields of 2-2.5 kV/cm [52],[53] to about 10 μJ/cm² for 20 kV/cm [54] have been used at the onset of radiation field screening (i.e. sub-linear increase of the emitted THz field with increasing fluence). Higher DC accelerating fields allow for (linearly) higher saturation fluences since a higher radiated THz field is required for screening. From the presented values, each μJ/cm² requires at least 2 kV/cm of DC field in order to prevent radiation saturation of the field screening for GaAs. However, early data [40] suggest later saturation at fluences in the range of 80 μJ/cm² for a bias field of 4 kV/cm (extrapolated from Fig. 8 of ref. [40]).

For LTG GaAs, Loata et al. [51] found radiation field screening saturation of the device for optical fluences in the range of 50-100 μJ/cm² (n_0~few 10^{18} cm^{-3}) for an accelerating field of 20 kV/cm. It saturates at higher optical fluences than SI GaAs.

For pulsed operation, trap saturation, bias field screening, and impedance matching/radiation field screening are getting important at similar optical power levels for both low lifetime material and SI GaAs. It is often difficult to distinguish the different contributions.

2.2.5. Device Layouts of Photoconductive Devices

The development of THz photoconductive devices is mainly electrical engineering and materials science. For CW operation, the material must feature (a) a low carrier life-time in order to improve the transit-time performance, (b) a high dark resistance for reducing the DC electrical load, (c) a high break-down field in order to allow for high DC biases, and last but not least, (d) an acceptable carrier mobility. For pulsed operation, a low carrier lifetime (a) is not desperately necessary, however, it helps to increase the break-down field and the dark resistance. It is fairly simple to accomplish (a)-(c) for instance by destroying or damaging the semiconductor lattice, however, at cost of mobility (d). Materials with low mobility, μ, do not allow for transport at the saturation velocity, if $v=\mu E_{DC}<v_{sat}$ for the applied maximum DC field. This results in low photocurrents and little emitted THz power. Materials need to be engineered in order to optimize items (a)-(d) at the same time. Several examples for both 800 nm and 1550 nm operation are discussed below.

2.2.5.1 Photoconductors at 800 nm

Photoconductors based on GaAs are the work horses in many THz laboratories. GaAs can be grown with a very small amount of unintentional doping. Due to the sufficiently large band gap of 1.42 eV, there are practically no thermally generated carriers and the dark resistance is high. These photoconductors require laser wavelengths shorter than 870 nm. They are often excited with Ti:sapphire lasers, particularly for pulsed operation. CW systems often consist of distributed feed back (DFB) diodes that are amplified with (tapered) semiconductor optical amplifiers (SOAs). Typical optical power levels for CW operation are 50 mW. A difference frequency of 1 THz requires 2.4 nm wavelength offset at 800 nm center frequency. Typical DFB diodes can be tuned by more than 2.5 nm, and a tuning range of ~5 nm (~ 2.1 THz) can easily be achieved. In the GHz range, semi-insulating (SI) GaAs can be used for fast optical receivers [55]. In the THz range, however, intrinsic or semi-insulating GaAs features a very pronounced transport-time roll-off for CW operation due to the lack of trapping centers. Space charge saturation occurs at fairly low optical power levels (see eq. [2.59] and [2.60] for $l_D=w_G$) and the electrical power dissipation is high. The lower break-down voltages and the lack of traps lead to non-linearities in the IV characteristics at substantially lower biases as compared to materials with low carrier lifetime [46]. In pulsed operation, however, SI GaAs devices perform very well: The space charge limitations occur much earlier, but the THz power emitted by an electron-hole pair is much higher as described in Section 2.2.2.2 b), Fig. 2.9 and discussion thereof. Since thermal dissipation scales with the average power but THz power scales with the peak power, thermal limits are suppressed by a factor of $\nu_{rep}\tau_{pls}$. Therefore, pulsed SI GaAs devices perform similarly well as devices based on materials with a short life time [46]. In the following, however, we focus on low lifetime material since such materials can be used in both CW and pulsed applications.

(a) Low temperature grown GaAs (LTG-GaAs)

LTG-GaAs is typically fabricated by molecular beam epitaxy (MBE) at low growth temperatures (~ 200 °C) under As overpressure on SI GaAs. [24]. At this low temperature, up to 1.5 % excess arsenic is incorporated. After annealing at temperatures up to 500-580 °C the excess As is forming antisite defects, which act as deep (double) donors, or quasi-metallic clusters. A very low lifetime in the range of 100 fs [56] and a reasonable mobility around 400 cm²/Vs can be achieved. Carrier life times and resistance can be widely engineered by the growth temperature and the subsequent annealing temperature (Fig. 2.14).

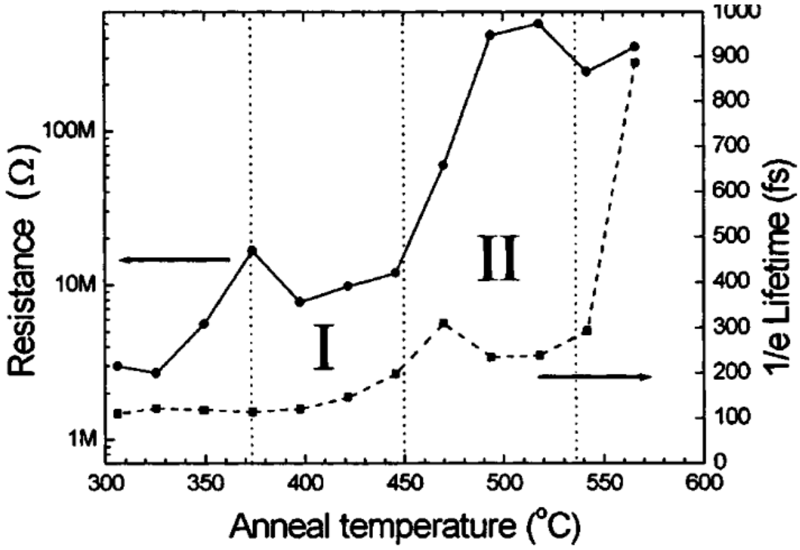

Fig. 2.14: Carrier life time of LTG-GaAs vs. annealing temperature. The growth was performed at 230±10 °C. At low annealing temperatures (region I and below), the material is dominated by defects, showing a comparatively low resistance but also a short life time. In region II, the lattice begins to relax; doping defects are reduced, increasing the resistance but the life-time remains on a similar level. Region II is ideal for producing photoconductive switches. Above region II, point defects are cured, the lattice constant relaxes towards that of the substrate. The annealing also reduces the trap state concentration, resulting in an increase of the life-time to ~ 1 ps or even more. [Pic from Paper: GregoryBaker2003; Copyright to be requested!]

Carrier trapping and scattering by the As clusters prevents any velocity overshoot. The IV characteristics remain linear. The break-down field is about 2-3 times higher than for SI GaAs. For operation at 800 nm, the absorption length is about 0.8 µm. A typical sample structure for CW operation is 1-2 µm thick and consists of two electrodes with 3-4 fingers each that are deposited on top of an LTG-GaAs layer (see Fig. 2.8). The finger width is in the range of 0.2 µm, the gap width, w_G~2 µm, depending on the design frequency. The area covered by the fingers is in the range of 100 µm² [24], resulting in an RC 3 dB frequency around 1.3 THz for a 72 Ω load. No mesa etching is required due to the high dark resistance in the GΩ/square range [24], since a noteworthy conductance only occurs in optically excited areas. Usually, an anti-reflection coating (ARC, thickness~280 nm for an SiO_2-film at 800 nm) is deposited on top of the active structure that also prevents oxidation of the semiconductor at high optical powers. In order to improve thermal conduction, often an AlAs heat spreader layer is deposited below the active material. A Bragg mirror, consisting of AlGaAs-AlAs λ/2 layers , can be grown underneath the active material to reflect the incoming laser and enhance the absorption [57]. This allows for thinner LTG-GaAs absorber layers. It also improves the electrical performance since the electric field applied by the finger electrodes is more homogeneous close to the surface. Several groups also reported improvement of the thermal management by sample transfer onto a highly thermal conductive material such as Sapphire or silicon [45],[49]. Industrial diamond and SiC have also been proposed as thermal substrates.

To the knowledge of the authors, the highest reported CW THz power in the low THz-frequency range is around 1.8 mW at 252 GHz [49]. A tunability range from <100 GHz to 3.8 THz with a single device has been reported [57] with still μW-level powers at 1 THz. LTG-GaAs based photoconductors have not only been used as antenna coupled devices but also as large area emitters (see Chapter 3.6.2) [45].

LT-GaAs photoconductors have to be operated with laser wavelengths shorter than 870 nm due to its band gap. Although absorption can also take place via the mid gap trap state [58] or by two photon processes (only in pulsed operation) [59], the absorption cross section is so low that very little has been reported with 1550 nm excitation.

(b) ErAs:GaAs at 800 nm

ErAs:GaAs is a promising alternative to LTG-GaAs. It consists of continuous growth of a superlattice sequence of GaAs-ErAs-GaAs with up to 2 ML ErAs [60] and a thickness for the GaAs layers in the range of 10-30 nm. Erbium tends to precipitate and form ErAs nanoparticles with a size in the range of ~2 nm [60] and a density in the range of $7x10^{12}$ cm^{-2} [61]. Bulk ErAs is a semi-metal with a Fermi energy slightly above the band gap center of GaAs. Due to quantization effects, small particles have been reported to show a transition from semi-metallic to semi-conducting [62]. In contrast to LTG-GaAs, ErAs:GaAs is grown at only slightly lower temperatures than standard GaAs, with typical values around 535°C-580°C [61], [63]. Due to the position of the Fermi energy in the band gap of GaAs, the ErAs particles act as very efficient trap centers. The trapping times mainly depend on the drift/diffusion time from the point of generation (by optical absorption) to the next ErAs particle. Higher particle density results in shorter trapping times, however, also in lower mobilities due to increased scattering. Trapping times in the range of τ_{rec}~120-250 fs [64],[65],[34] and a significantly higher mobility than LTG GaAs [24] have been reported. The incomplete surface coverage of ErAs allows for continuous overgrowth with defect-free GaAs, because of the available GaAs surface where growth can continue. The electrical performance is comparable to that of LTG-GaAs. A break-down voltage of 200-500 kV/cm has been reported [34],[61]. The dark resistance is about 100 times lower than LTG-GaAs [24], however, still high enough in order to produce useful photoconductors with a dark resistance in the several MΩ range [24]. The comparable electrical properties and life times result in comparable performance as LTG-GaAs photoconductors. Interestingly, a special growth mode of ErAs:GaAs allows for noticeable absorption at 1550 nm, allowing for implementation of ErAs:GaAs photomixers at telecom wavelengths. This will be discussed in the next section.

2.2.5.2 Photoconductor concepts at 1550 nm

1550 nm compatible photomixers benefit from the huge variety and low cost of telecom components. A wavelength difference of 8 nm is required for a difference frequency of 1 THz. CW systems often consist of two DFB diodes that are yet commercially available with a mode hop free tuning range of about 4.5 nm. Two diodes can therefore cover a frequency range of about 1.2 THz. For a larger tuning range, one of the DFBs can be replaced with a grating tuned source. In both cases, the laser linewidth is in the low MHz range. DFB diodes are also very stable (on the same scale as the linewidth, see Chapter 7). If more power is required, Erbium doped fiber amplifiers (EDFA) are used. The systems are often completely fiber based (with polarization maintaining fibers), allowing for simple handling and very little alignment effort. Only the free space THz path needs alignment. In 1550 nm CW systems, photoconductors are mainly used as coherent detectors. Although they can also generate THz radiation, p-i-n diode based mixers are typically more efficient.

Pulsed systems frequently use 1550 nm fiber lasers. Due to dispersion, the fiber laser length, *l*, is usually kept fairly short, resulting in high repetition rates in the range of $\nu_{rep}=c/2l$~70 MHz. Photoconductors are both used as sources and coherent detectors. If coherent detection by electro-optic sampling (EOS) is desired, the 1550 nm signal can be frequency-doubled such that EOS crystals with phase-matching at ~800 nm (ZnTe, e.g.) can be used.

In contrast to well established 800 nm photomixers, devices for 1550 nm operation suffer intrinsically by the ~2 times lower band gap (~0.74 eV). It is very challenging to obtain deep traps and high dark resistances while maintaining a sufficiently high carrier mobility and absorption coefficient. Low temperature grown $In_{0.53}Ga_{0.47}As$, for instance, is strongly n-type [66], in contrast to LTG-GaAs. Further, the break-down voltage, E_B, is lower. From semiconductor physics, the break-down field tends to vary with band-gap energy superlinearly and studies have yielded universal empirical relationships such as E_B [V/cm]= $1.73\text{x}10^5$ $(U_G\ [eV])^{2.5}$ for low-doped direct-band-gap materials [67]. Hence, the difference between the GaAs E_B (U_G = 1.42 eV) and E_B of InGaAs is predicted to be a factor of 4.9, which is rather close to the observed difference in the maximum bias voltage between homogeneous GaAs and InGaAs ultrafast PC devices. Several strategies have been demonstrated to fulfil the needs and to overcome the discussed problems of telecom-compatible photomixers.

(a) Extrinsic photoconductivity at 1550 and 1030 nm of ErAs:GaAs

(E.R. Brown)

A promising alternative to InGaAs is to use GaAs with 1030 or 1550 nm drive lasers and utilize sub-band-gap photon absorption mechanisms via the high concentration of defect- or impurity-levels that ultrafast materials generally have. In pulsed-mode, for example, attempts have been made to utilize two-photon absorption and sub-ps recombination via the mid-gap states associated with As-precipitates in LTG GaAs [68],[69]. This was then used to demonstrate a PC switch, but the resulting photoconductivity was found to be impractically weak compared to the intrinsic cross-gap effect. In CW mode, attempts have been made to overcome the weak 1550 nm absorption by embedding the LTG GaAs in a dielectric-waveguide, distributed p-i-n photodiode [70]. But the waveguide length required for strong absorption reduces the electrical bandwidth because of difficulties

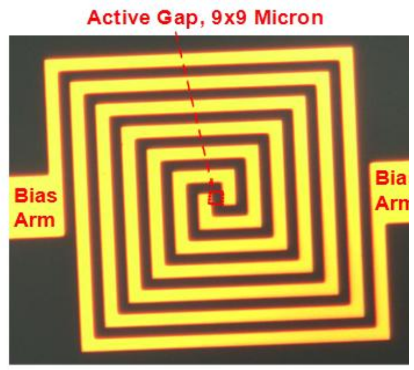

Fig. 2.15: ErAs:GaAs self-complementary square-spiral photo-conductive switch

in velocity matching the photonic and RF waves.

To date, the most attractive extrinsic photoconductive material has been co-doped (homogeneous) Er:GaAs. Test structures such as the PC switch in Fig. 2.15 have yielded valuable data pertaining to DC photoconductive and THz performance [71]. First, the DC photoconductivity was characterized at 1550 and 1030 nm with up to P_0 =140 mW of average laser power at each wavelength. This limitation is necessary on one hand to guard against damaging the PC switch, and on the other hand for consistency between the 1550 nm and 1030 nm measurements since this was the maximum power available from the 1550 nm laser but not the 1030-nm laser. The 1550 nm laser was an EDFA mode-locked laser with a repetition frequency of ν_{rep}=36.7 MHz and pulse with of τ_{pls}~300 fs. The 1030 nm laser was a YDFA mode-locked laser with a repetition frequency of ν_{rep}=31.1 MHz and pulse with of τ_{pls} ~190 fs. Laser power measurements were taken with a commercial thermopile-type detector. The laser beam at both wavelengths was focused into the active (central) gap of the PC switch in Fig. 2.15 with a standard 10x microscope objective. The bias voltage was fixed at 77 V – a value found low enough to provide reliable operation at the maximum 140 mW laser power level. The DC photoconductivity results are plotted in Fig. 2.16 (a) and (b) for 1550 and 1030 nm light, respectively. The two curves are substantially different at low P_0, but similar at high P_0 in that they both approach a linear asymptote. This is in contrast to the continuous quadratic-up behavior displayed by LTG-GaAs switches with 1550 nm drive [69]. At low P_0, Fig. 2.16 (a) and (b) also show nonlinear behavior, but concave down in Fig. 2.16 (a) and concave-up in Fig. 2.16 (b), which is not yet understood. At the low end of the linear asymptotic region of Fig. 2.16 (a), the current responsivity is $\Re \approx 5$ µA/mW, and at the high end it is $\Re \approx 1.0$ µA/mW. The former is about 4-times less than the $\Re$ from an identical type of PC switch (same ErAs:GaAs material) measured at the same U_{DC} with a 780 nm sub-ps pulsed laser.

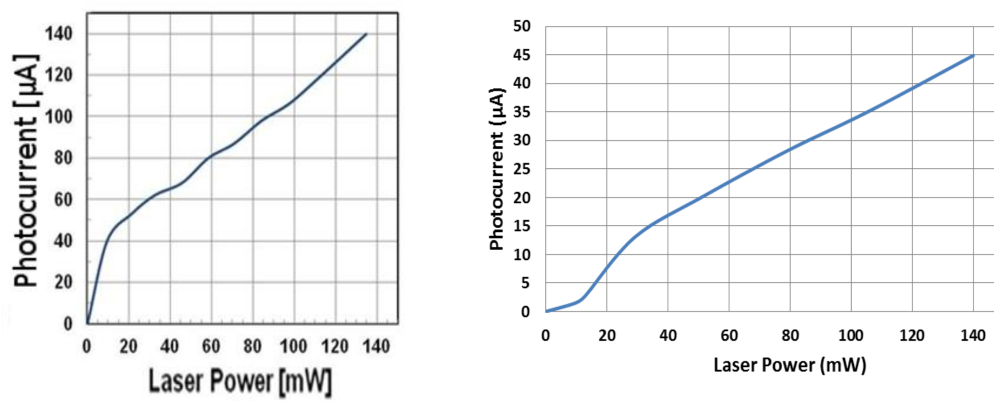

Fig. 2.16: (a) DC photocurrent vs average 1550 nm laser power at 77 V bias. (b) Same as (a) except with 1030 nm laser.

In contrast, the photocurrent for the 1030 nm laser in Fig. 2.16 (b) reaches a maximum value of 44.9 µA, corresponding to $\Re \approx 0.32$ µA/mW, which is about 3-times less than the 1550 nm result.

However, it still supports our interpretation of the new effect as extrinsic photoconductivity rather than two-photon absorption. This is because 1030 nm photons would not match the energy-momentum conservation criteria for two-photon transitions across the GaAs band gap, so would experience far weaker absorption coefficient than 1550-nm photons. The promising 1550 nm photocurrent suggests that this PC switch should produce measurable THz power, assuming of course that the photocarrier lifetime associated with the new photoconductive mechanism is

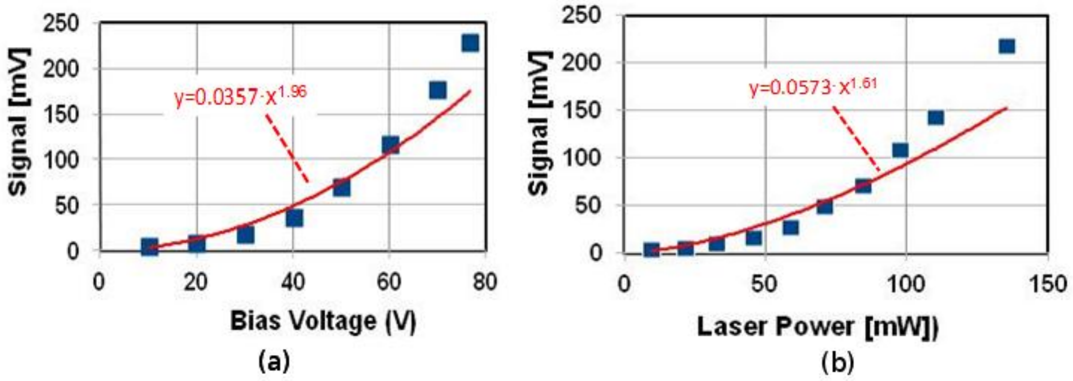

Fig. 2.17: (a) RMS output from THz pyroelectric detector vs. bias voltage with a constant 1550-nm laser power of 140 mW. (b) RMS output from THz pyroelectric detector vs. 1550-nm average laser power at a constant bias of 77 V.

comparable to that of the traditional intrinsic, cross-gap effect (typically << 1 ps). The THz output power was first measured with a broadband, calibrated pyroelectric detector having a crude low-pass filter (0.010-inch-thick black polyethylene) to block the mid-IR-to-visible radiation. Its resulting THz responsivity is roughly 5000 V/W. The pyroelectric signal vs. bias, U_{DC} , (Fig. 2.17 (a)) was measured at a fixed 1550 nm laser power of 140 mW, and the signal vs. P_0 (Fig. 2.17 (b)) was measured at a fixed bias voltage of 77 V. The vertical scale in both plots is rms lock-in amplifier reading; when adjusted for this, the maximum reading in both Fig. 2.17 (a) and (b) corresponds to a peak-to-peak reading of approximately 520 mV (confirmed on an oscilloscope). Hence the maximum power measured from the switch is ≈105 μW [71]. In stark contrast, no THz power was measured from the same PC switch driven by the 1030 pulsed laser under the same operating conditions. This suggests that the photocarrier lifetime associated with the extrinsic photoconductivity is quite sensitive to laser drive wavelength, but for reasons that are not yet understood.

Inspection of Fig. 2.17 (a) and (b) provides an interesting contrast to the operating characteristics usually displayed by intrinsic photoconductive switches driven at 780 nm [72]. The nearly quadratic dependence on bias voltage in Fig. 2.17 (a) is stronger than at 780 nm, whereas the sub-quadratic [$P_{THz} \approx (P_0)^{1.6}$] dependence on drive power in Fig. 2.17 (b) is weaker than at 780 nm [73]. The maximum 1550 nm-driven THz power is comparable to the broadband THz power measured from an identical type of switch (same ErAs:GaAs material) at the same U_{DC}, but driven with 25 mW of average 780-nm power. Hence, the new 1550-nm-driven photoconductive mechanism is about 5-times less efficient in terms of THz-to-laser power conversion. An obvious way to improve this efficiency would be to increase the thickness of the active epitaxial layer, which is approximately 1.0 micron in all the devices tested to date.To estimate the power spectrum and bandwidth of the 1550 nm-driven PC switch, we carried out spot-frequency power measurements using a set of Schottky-diode zero-bias rectifiers mounted in rectangular waveguide and operating in three distinct bands centered around 100 (W-band), 300 and 500 GHz, as shown in Fig. 2.18 (a) [71]. These rectifiers act as band-limited filters with very sharp low-frequency turn-on (waveguide cutoff) and more gradual high-frequency roll-off. This enables a discrete estimate of the THz switch power spectrum knowing the external responsivity of the rectifiers and their noise equivalent bandwidth. The resulting data is plotted in Fig. 2.18 (b), normalized to the signal from the 100-GHz rectifier. The bandwidth is obtained by fitting the discrete spectrum to a single-pole Lorentzian function, $S(f)=A/[1+(2\pi f\tau)^2]^{-1}$, where A is a constant and τ is the photocarrier lifetime. This has been found to be a good fit to the THz power spectrum of PC switches whose photocarrier lifetime is significantly longer than the RC electrical time constant – a likely condition in the present case since the gap capacitance of the switch is << 1 fF. For the experimental data in Fig. 2.18 (b), the best fit to the data occurs when A = 1.08 and τ = 0.45 ps, This corresponds to a -3-dB frequency-domain bandwidth of $B = (2\pi\tau)^{-1}$ = 354 GHz, which is comparable to the bandwidth deduced from 780-nm time-domain measurements for the identical type of switch (same ErAs:GaAs material and antenna) with a 780-

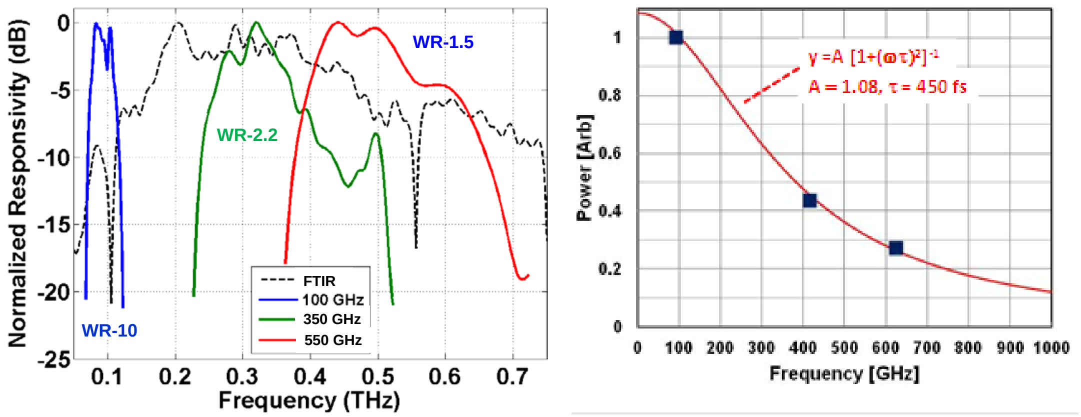

Fig. 2.18: (a) Broadband spectrum from 780-nm-driven PC switch, and responsivity spectra of three waveguide Schottky rectifiers used for spot-frequency measurements. (b) Spot-frequency spectrum from 1550-nm-driven PC switch and curve fit.

nm femtosecond laser [72]. However the laser pulse in the present experiments (300 fs) is considerably longer than that used at 780 nm, so that the lifetime-limited bandwidth of extrinsic PC switch could be even higher than 354 GHz.

(b) ErAs:InAlAs/InGaAs devices

(S.Preu)

The fairly low absorption of ErAs:GaAs at 1550 nm can only be overcome if the inter-band transition is used for absorption: for $In_{0.53}Ga_{0.47}As$, the absorption coefficients are in the range of 8000/cm. However, the typical problems for InGaAs-based photoconductors have to be faced: the Fermi energy of semi-metallic ErAs in InGaAs is close to (or even above) the conduction band edge [75]. Although carriers are still trapped by the semi-metal, the high density of states of ErAs result in a strong n-type background that has to be compensated with a p-dopant. Typically, either Beryllium or Carbon is used. The large p-doping (of the order of 10^{20}/cm³) and scattering by the ErAs particles results in rather low mobilities in the range of 900 cm²/Vs [76] for material with sufficiently low lifetime, getting lower with higher Er concentration and stronger doping. In most cases, the n-background cannot be completely compensated, leading to fairly low resistances in the range of 10 -100 Ωcm (100 kΩ/square for a 1 μm thick sample) [77]. In ref. [78] a resistivity of 343 Ωcm was specified, however, without a specifying the mobility. Furthermore, exact compensation is difficult: a small error in the doping concentration around the point of perfect compensation can push the Fermi-energy from the center of the band gap right o the conduction- or valence band edge if no deep traps are present that pin the Fermi energy. In contrast to ErAs:GaAs, a compromise between short carrier life time (requiring high ErAs concentration), low dark conductivity (low ErAs concentration and high p compensation doping beneficial) and mobility (low ErAs concentration and low p-doping) has to be found. The problem of low break-down voltage cannot be overcome. Still, functional photomixers have been fabricated from ErAs:InGaAs with lifetimes in the range of 200-300 fs [78],[79]. Low temperature operation can help to freeze out carriers for overcoming thermal heating limitations [80] by excess dark conductance.

In order to reduce the large n-background, a superlattice of InGaAs-ErAs:InAlAs has been implemented as illustrated in 2.**Error! Reference source not found.** a) and b) [81]. ErAs is a deep trap in InAlAs. If the InAlAs layer is chosen only a few nm thick, carriers can tunnel into the ErAs states in InAlAs and are efficiently trapped. Some p-doping is still necessary in order to compensate for the n-background by carriers tunnelling out of the ErAs states. Since carriers have to tunnel into the ErAs states (with limited tunnel probability), the carrier-lifetime can be quite long. However, it is already sufficient to grow the ErAs between an InAlAs and an InGaAs layer (Fig 2.19 b), as a compromise between lifetime and resistance. Generally, the resistance of such a structure can be much higher than that of the ErAs:InGaAs material. The absorption takes place in the adjacent InGaAs layers between the InAlAs layers. The band structures shown in **Error! Reference source not found.** a) and b) resemble quantum wells. Shifts of the absorption edge towards longer wavelengths due to quantization effects remain small if the InGaAs layer is chosen fairly wide, with thicknesses in the range of 15 nm. The absorption coefficient is just slightly lowered at 1550 nm as compared to bulk InGaAs. Besides the higher resistance, another advantage is the much higher carrier mobility due to the absence of ErAs in the absorber material and less p-background doping. Since carriers first have to drift towards the InAlAs barriers and then have to tunnel into the ErAs trap states, the carrier life time is longer than that of ErAs:InGaAs. The layer thicknesses of both the InAlAs tunnel barriers and the InGaAs absorber layers are a compromise between high resistance, absorption, and low life time. Typical values are 2.5 nm for the p-doped InAlAs both above and below the ErAs layer, followed by a 15 nm InGaAs layer. In order to achieve an absorber thickness in the range of 1 μm, a sequence of N=70 superlattice periods has been used, resulting in a total thickness of 1400 nm. Such InGaAs-ErAs:InAlAs photomixers have been used for pulsed measurements [81]. A representative measurement with a large area emitter is shown in **Error! Reference source not found.** *c)*. The material showed a resistivity of 670 Ωcm, a mobility of 1120 cm²/Vs and a carrier lifetime of 2.8 ps.

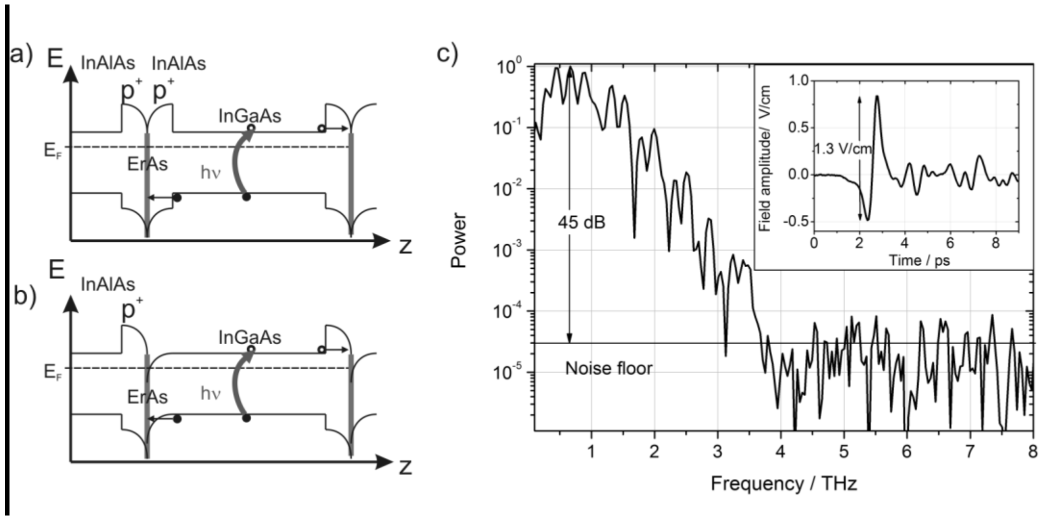

Fig 2.19: a) InGaAs-ErAs:InAlAs photomixer ideal band diagram. The ErA-layer is sandwiched between InAlAs tunnel barriers in order to increase the dark resistance of the material b) Device with only one tunnel barrier. The sheet resistance is still strongly increased. c) Typical power spectrum obtained with an InGaAs-ErAs:InAlAs large area emitter (design as in b) under pulsed operation (laser wavelength 1550 nm, 100 mW average power, pulse duration 100 fs, repetition rate 78 MHz). Electro-optic sampling with ZnTe was used for detection. This results in the stronger roll-off above 3 THz where the detection crystal absorbs. The inset shows the time domain pulse. The ringing is due to reflections by an attached heat spreader.

(c) LTG-InAlAs:InGaAs devices

(T. Göbel)

A further concept for the realization of suitable photoconductors for the operation at 1.5µm optical wavelength is a low-temperature-grown (LTG) InGaAs/InAlAs multilayer structure, which is additionally doped with Beryllium. Grown at temperatures below 200 °C, excess arsenic is incorporated as point defects on Ga lattice sites (antisite defect, As_{Ga}), which form deep donor levels in the material. In LTG-GaAs these defects are mid-bandgap, whereas As_{Ga} defects in LTG-InGaAs lie energetically close to the conduction band (CB) edge with activation energies around 30–40 meV. The reduction of the electron lifetime in LTG material compared to standard temperature grown (STG) semiconductors is attributed to electron capture by ionized arsenic antisites (As_{Ga}^{+}). In LTG-GaAs the arsenic antisites are ionized by Ga vacancies, whereas ionization in LTG-InGaAs is mainly thermal due to the low activation energy of the defect. This shift of the Fermi level towards the conduction band leads to highly n-conductive material at room temperature. To increase the resistivity of the material, the InGaAs-layers are sandwiched between InAlAs-layers barriers which trap the residual carriers. These layers are high bandgap and therefore transparent for the incident optical signal. By using the p-dopant Beryllium, the resistivity is further increased.

The structure illustrated in Fig. 2.20 (i.e. 12 nm InGaAs, 8 nm InAlAs), typically features a Hall mobililty of 600 cm^2/Vs, a resistivity of 300 Ωcm and a carrier lifetime of 500 fs for a Be-doping concentration of $2x10^{18}$ cm^{-3}. This multilayer photoconductor successfully combined the required material properties for THz generation at 1.5µm optical wavelength for the first time and enabled the first fully fiber-coupled pulsed THz-system in 2008, featuring a bandwidth of roughly 3 THz and a DNR of 30 dB [82].

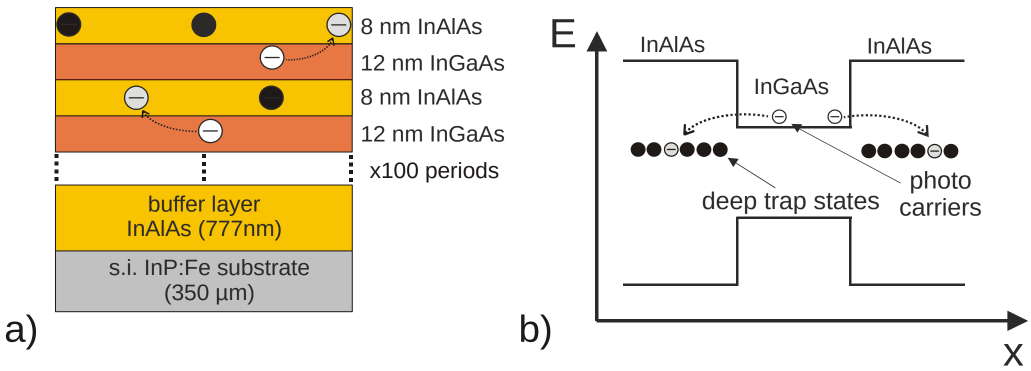

Fig. 2.20: Schematic of InGaAs/InAlAs heterostructure, with 100 periods of a 12 nm InGaAs layer followed by a 8 nm InAlAs layer with cluster-induced defects acting as electron traps. b) Schematic of the respective band-diagram in real space with deep cluster-induced defect states.

A general disadvantage of photoconductive antennas with on-top metal contacts results from the decreasing in-plane electrical field component in the depth of the photoconductor. In the depicted multilayer structure, this problem is enhanced due to the many interfaces at the intermediate InAlAs layers with higher bandgap. The interaction of photocarriers with the electric field is reduced, which results in a low mobilty limiting the obtainable THz power. This problem was solved by mesa-type structures with electrical side contacts. Here, the electrical field is directly applied even to deeper layers, and the current in the receiver does not need to cross heterostructure barriers. As compared to their planar counterpart, the mesa-type photoconductor increased the peak-peak amplitude of the THz-pulse by a factor of 28 and the bandwidth of the system exceeded 4 THz [83].

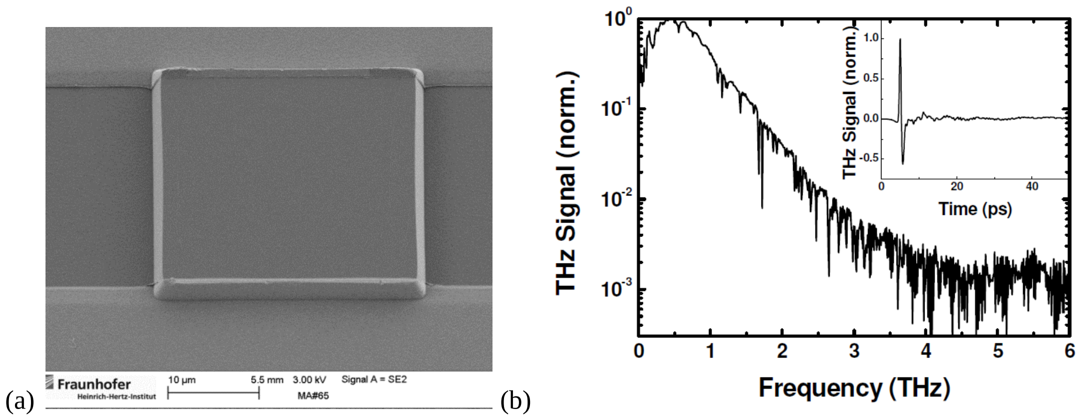

Fig. 2.21: Mesa-structures InGaAs/InAlAs photoconductor (a) and corresponding THz-Spectrum (b). The photoconductor features a stripline geometry with 25µm gap, which was biased with 5V and illuminated with 10 mW optical power.

A quick comparison of the mobility of the multilayer-structure (600 cm^2/Vs) and the mobility of bulk InGaAs (10 000 cm^2/Vs) reveals that, the photoconductor does not profit from the high InGaAs mobility, which limits the obtainable THz power. This is due to the high defect concentration of the material causing a strongly reduced carrier mobility due to elastic and inelastic (i.e. trapping) scattering of carriers at defect sites. A device which better matches the mentioned requirements can be realized by MBE growth of InGaAs/InAlAs multilayer heterostructures by utilizing a special characteristic of MBE growth of InAlAs. Within a substrate temperature range between T_S = 300 - 500 °C the growth of InAlAs shows strong alloy clustering effects with InAs-like and AlAs-like regions featuring clusters sizes of several nanometers, with a maximum cluster density for $T_S \approx 400$ °C.

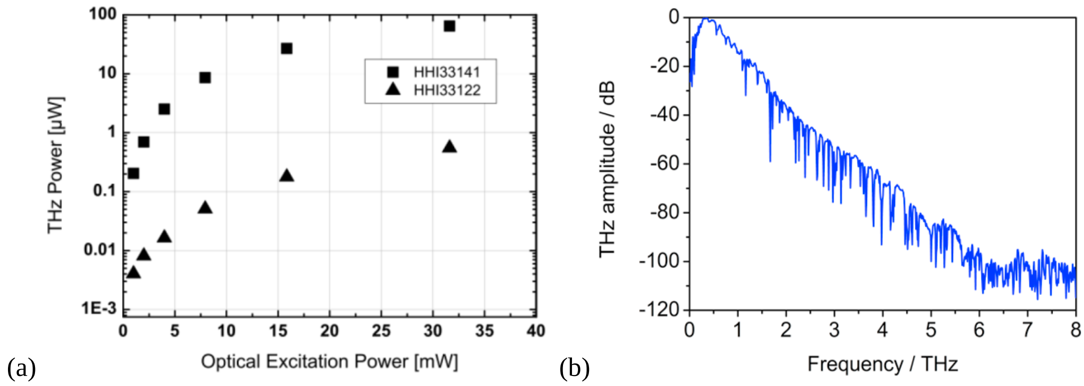

Fig. 2.22: Emitted THz power of a 100 µm strip-line antenna from a sample grown at 400 °C (HHI33141) and 200 °C (HHI33122) in dependence on the optical excitation power at a bias field of 15 kV/cm. In combination with an optimized receiver, a dynamic range of 100 dB was obtained, with a bandwidth of 6 THz.

The activation energies of these cluster defects have been measured to be in the region of E_A = 0.6-0.7 eV, which leads to semi-isolating InAlAs . By exploiting the above characteristics it is possible to obtain InAlAs/InGaAs photoconductors with low defect density and high mobility InGaAs layers adjacent to InAlAs layers with high defect densities at the same growth temperature for efficient carrier trapping. In such a way, the mobility of the material can be increased up to 5000 cm^2/Vs with a resistivity of 300 Ωcm. With this highly mobile material, THz power up to 64 µW have been obtained for an optical illumination power of 32 mW [84] (cf. Fig. 2.22).

In addition, photoconductors are also excellent detectors for CW THz systems operating with 1550 nm drive lasers. These detector applications will be discussed in detail in Chapter 7.

(d) Ion-implanted photoconductors

Another option to generate deep traps in InGaAs is by means of ion damage. Ions with energies in the high keV to MeV range irradiated onto a semiconductor create many defect states by penetrating through the lattice, e.g. by kicking out atoms or pushing atoms into interstitials. This results in a variety of trap states of different flavors, finally reducing the carrier mobility. A variety of ions has been used such as Br [85], Fe [86],[87], H, Au [88] and others. The optimum dose strongly depends on the implanted ions (weight) and implantation energy. For Be at 11 MeV, a dose around 10^{11}-10^{12} /cm³ was used [89]. The type of ion is secondary: In most cases, ion energies are chosen high enough to ensure that most of the ions come to rest far below the THz-active zone (~1-2 µm below the surface, defined by the absorption depth of the laser light). As-irradiated material is usually so strongly distorted that it cannot be used for THz applications; the carrier mobility is extremely low. An annealing step at temperatures between 500 °C and 800 °C [86],[87] is required to partially restore the lattice and allow for accumulation of trap centers. Mobilities up to 3600 cm²/Vs with life-times of 0.3 ps have been reported [90]. An average THz power of 0.8 μW was obtained under pulsed operation [90]. A spectrum is shown in Fig. 2.23 b). The break-down field increased to $E_B \approx$ 7.5 kV/cm [89] by about a factor of 4 compared to unimplanted samples. The resistivity of that specific device was not reported. In ref. [91], the same group reported on a value of ~5 Ωcm only. The authors pointed out that the residual carrier density is fairly invariant with respect to the ion dose. Some compensation doping would be required to reduce the dark conductivity. For further reading on ion-implanted materials, we refer to ref. [89].

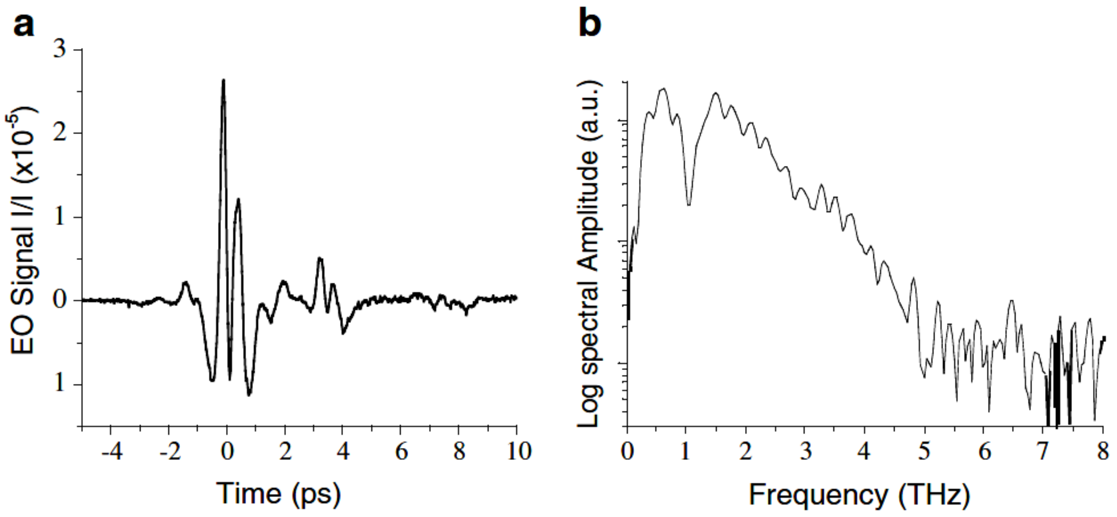

Fig. 2.23: a) THz pulse generated by Be^+ ion-damaged InGaAs excited with a τ_{pls} = 80 fs 1550 nm laser and recorded with a DAST crystal; b) Fourier spectrum. The dip at 1 THz is due to absorption of DAST. [Request copyright for Fig 11 of [Mangeney2011]]

2.2.5.3 Plasmonic enhancement for photoconductors

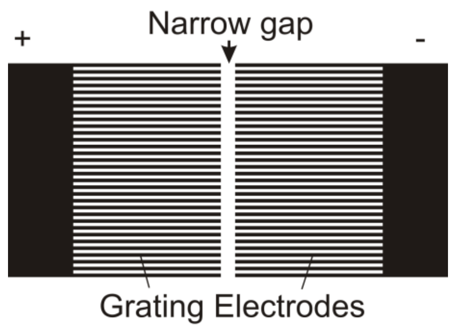

Fig. 2.24: Nano-gap elecrode structure as reported by Tanoto et al. [93]. A THz antenna is connected to the electrode.

Plasmonic effects have recently been explored for improving the performance of photoconductors [92],[93],[94]. There exist two types of plasmonic enhancements that have been implemented: 1.) Optical absorption enhanced structures: Well designed, nanometer-sized, metallic objects can feature plasmonic resonances that are excited by the incident laser power. The plasmons strongly increase the absorption close to the metallic obstacle. This allows for much shorter penetration depths of the laser light, where the DC field by the electrodes is fairly strong. Further, the reduced absorption depth allows for thinner InGaAs layers with low thermal conductance. Often, the nanometer-sized plasmonic structures are implemented in the electrodes. One carrier type (typically the electron) has very short transit lengths, resulting in high quantum efficiency. 2.) THz field enhanced structures:

Due to sharp tips or nanometer-sized gaps and structures, the THz field is locally strongly enhanced. This improves, for instance, the performance of a photoconductive detector where the enhancement factor due to plasmonics is directly proportional to the detected photocurrent. In the following, we will briefly discuss some examples for plasmonic enhancement of photoconductors from the literature. Plasmonic enhancement for other THz generation concepts will be discussed in detail in Section 2.3.5.

Park et al. [94] reported on a photoconductive gap that was modified with silver nanoparticles with a diameter of ~170 nm. The lasers induced a plasmonic response, resulting in enhanced absorption close to the nano-particles. This increased the THz power by a factor of two for the same excitation conditions. However, the authors pointed out that the break-down DC voltage may be reduced by the particles, leading to lower maximum THz power.

Tanoto et al. [93] have designed a nano-gap electrode structure as illustrated in Fig. 2.24, which benefits from both aforementioned effects. The strong field enhancement at each electrode tip (particularly in the gap) results in efficient carrier extraction. Further, the capacitance of the structure is fairly small since it obstains interdigitated electrodes. Although the active area (i.e. the nano-gap area) is small, a strong improvement of the emitted THz power of up to a factor of ~100 as compared to a standard design, was reported. Another approach by Berry et. al [92],[95] that applies both types of plasmonic enhancements uses plasmonic grating contact electrodes as illustrated in Fig. 2.25. The lasers illuminate the gratings that are attached to the antenna arms. A fairly large gap is used that is not illuminated. Typical parameters for the grating are gold electrodes with 200 nm pitch, 100 nm spacing, and 50 nm height. In order to improve coupling to the plasmons in the electrodes, an ARC coating with 150 nm SiO_2 is deposited on top of the grating. The thickness is optimized for maximizing the plasmonic resonance for 800 nm. Due to the small grating spacing of only 100 nm and due to plasmonically enhanced absorption close to the electrodes, electrons feature a very short transit-time resulting in a large gain for electrodes. Holes, however, are either trapped or have to move several microns to the opposite electrode . They produce a space charge background and do not contribute to the THz response. The large distance of the electrodes results in a low capacitance and a high DC resistance. The small electron transit-time results in a fast response. A 30 times improvement of the THz detection sensitivity has been reported [95].

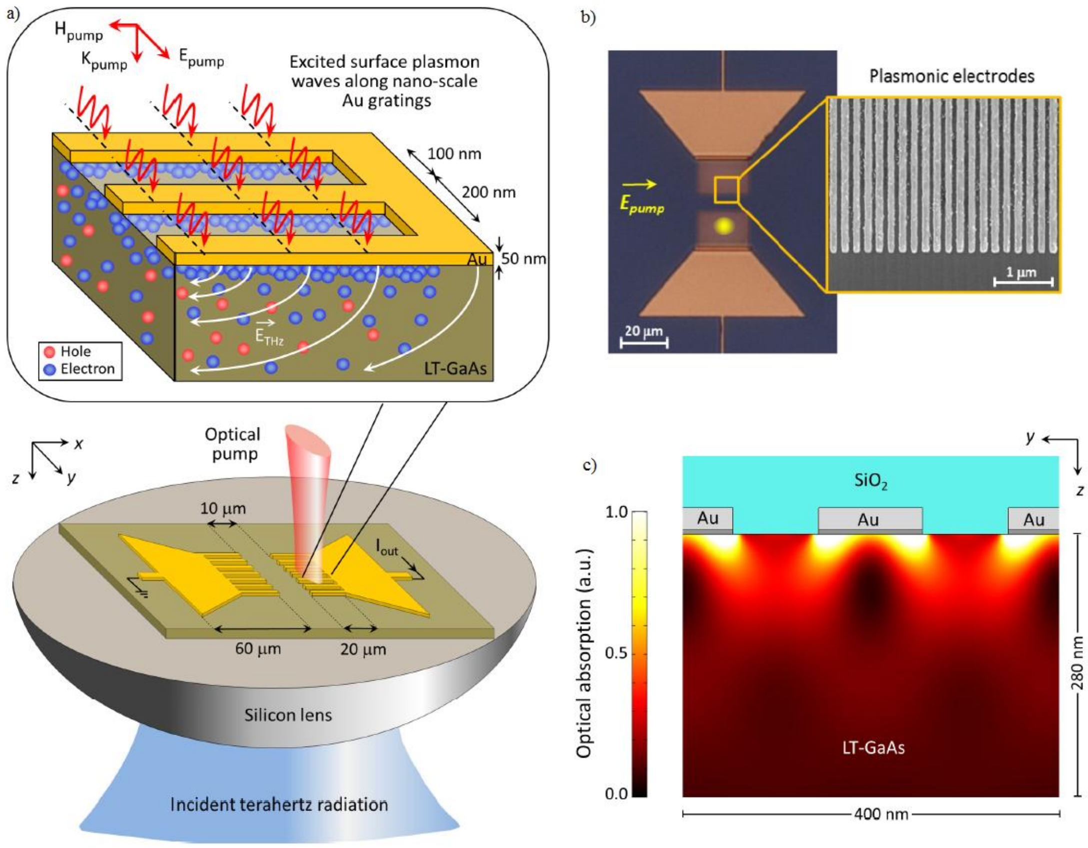

Fig. 2.25: a) Schematic of the plasmonic structure and the antenna-integrated device. b) Micrograph of the structure. c) Simulated optical absorption. [Fig1b, Fig 2b & Fig 3b von Mona Jarrahi Optics express 2013 [request copyrights]]

2.2.6. Device Layouts of p-i-n Diode Based Emitters

There are very few examples for p-i-n diodes at 850 nm in the literature. Most results are for 1550 nm based operation using InGaAs/InP-based devices.

2.2.6.1 UTC diodes

Uni-travelling carrier (UTC) diodes are up to now the most successful p-i-n diode based photomixers for CW operation. They have been invented by researchers at Nippon Telegraph and Telephone (NTT, Japan). A typical band structure is depicted in Fig. 2.7. In UTC-diodes, the p^--doped absorber layer is attached to the p-contact. The transport and current is mainly due to electrons with at least partial ballistic transport. This is achieved by using a transport or collection layer with a larger band gap as compared to the absorption layer. A few groups have reported on ~830 nm UTC diodes based on (Al)GaAs [96]. The majority of UTC diodes, however, is designed for 1550 nm operation with InGaAs absorbers, followed by 2-3 transition steps with InGaAsP layers to the InP transport (or collection) layer. Typical lengths for the absorber and transport layers are 100 nm and 300 nm, respectively [32],[37]. Besides telecom compatibility, InGaAs/InP UTC diodes also benefit from the larger inter-valley energy of InGaAs ($E_{\Gamma L}$ =0.46 eV) and InP ($E_{\Gamma L}$= 0.59 eV) as compared to GaAs ($E_{\Gamma L}$ =0.29 eV). The electrons can gain much higher energy before being scattered which allows for larger ballistic transport lengths. An increase of the average transport velocity of a factor of 3 as compared to the saturation velocity, v_{sat}, has been reported in [97], indicating partially ballistic transport .

The original design by NTT, Japan (Ito et al., [32]) features an output power of 2.6 μW at 1.04 THz with a wide band logarithmic-periodic antenna and even 10.9 μW with a resonant antenna. The device cross section was 13 μm², with photocurrent densities in the range of 100 kA/cm² (i.e. photocurrents of 13 mA). The photocurrent responsivity was 0.02-0.03 A/W, the transit-time 3 dB frequency was 170 GHz, the RC 3 dB frequency of the device with broadband antenna 210 GHz. With a design optimized for 100 GHz, 20 mW of output power has been reported [48].

Other designs, including backside illumination and side illumination by a waveguide design have been realized [37],[39]. In [37], Renaud et al. have designed a travelling wave UTC diode with a resonant antenna, delivering 24 μW at 914 GHz (at 100 mW optical power). The optical responsivity was in the range from 0.14-0.36 A/W. The absorber layer was 70 nm and the transport layer was 330 nm long.

Beck et al. [33] have designed a TEM-horn-coupled UTC diode with a diameter of only 2 μm allowing for high RC 3 dB frequencies. The transport layer was also chosen short (only 137 μm) in order to increase the transit-time 3 dB frequency. With a photocurrent of only 2.75 mA (optical power 50 mW) they achieved 1.1 μW at 940 GHz.

Waveguide coupled 1550 nm UTC diodes by the Heinrich-Hertz Institute, Germany, so-called Waveguide INtegrated PhotoDiodes with a THz Antenna (WIN-PDA), are yet commercially available. An output power of 5 μW at 500 GHz has been achieved at an optical power of only 25 mW [98].

2.2.6.2 Triple transit time diodes

(A. Stöhr)

The UTC diode has been demonstrated with highest performances within the THz frequency range as reported in the sections above. In contrast to the conventional p-i-n diodes, where both types of the photogenerated carriers contribute to the overall photocurrent, there is only electron drift in the UTC diode, which is a key feature for high-frequency operation and for overcoming saturation effects such as the space charge effect. In a conventional UTC diode, this is achieved by using an undepleted p-type absorber instead of a depleted non-intentionally-doped (n.i.d.) absorber as it is the case in the p-i-n diode. Thus, one can assume hole relaxation and neglect hole diffusion in the absorption region of the UTC diode. However, the transit time limited bandwidth of a UTC diode still suffers from the slow electron diffusion in the highly p-doped (InGaAs) absorber layer. This drawback has been tackled by further inventions that have led e.g. to the development of the so-called modified UTC (MUTC) diodes which also greatly overcome the saturation effects [99],[100]. In contrast to the original UTC diode, the absorption region of a MUTC does not only consist of an undepleted p-doped absorption region but also of an additional depleted InGaAs absorption layer.

This, however, implicates that there is a substantial hole drift in the depleted absorber of MUTC-PDs, which is somewhat in contradiction to the expression “uni-travelling-carrier”.

To overcome the limiting low electron diffusion occurring in UTC and also in MUTC diodes, a new structure entitled Triple Transit Region (TTR) photodiode was invented and reported in [101] by Rymanov et al. A schematic view of developed TTR diodes, the band diagram and the entire TTR diode layer structure including a monolithically integrated lower InGaAsP/InP passive optical waveguide (POW) grown on a semi-insulating (s.i.) InP substrate (thinned to 125 nm) is shown in Fig. 2.26. The key innovation of the TTR diode manifests in the active waveguide section of the diode.

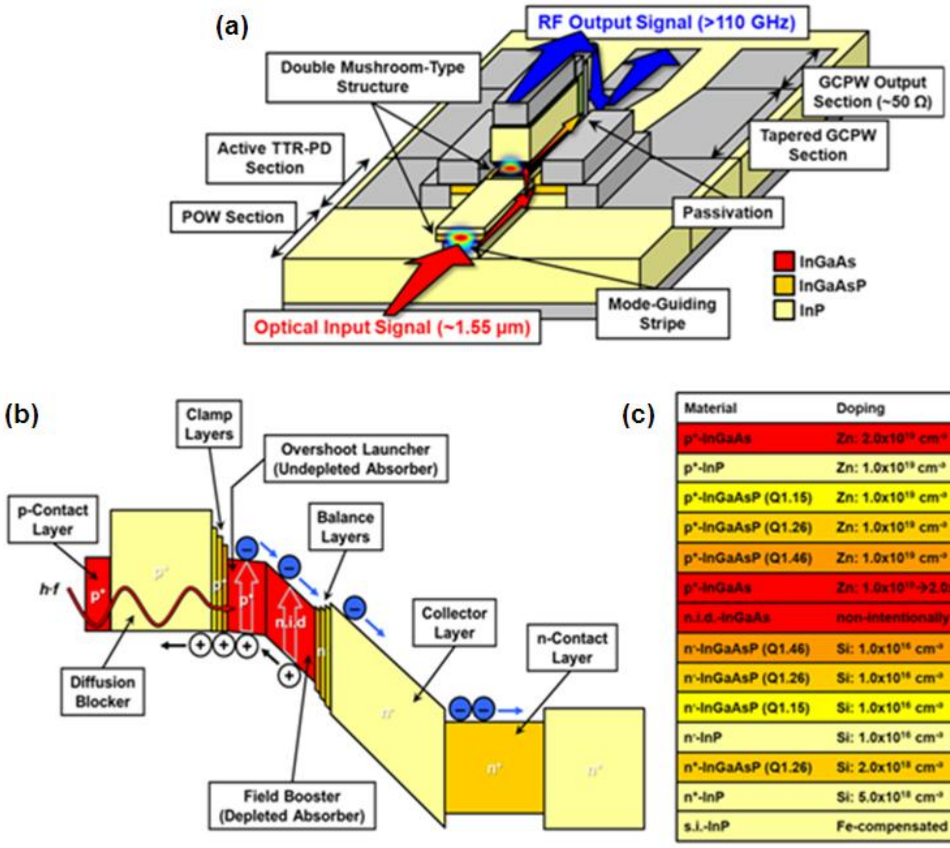

(c)

Material	Doping	Thickness
p^+-InGaAs	Zn: 2.0×10^{19} cm^{-3}	30 nm
p^+-InP	Zn: 1.0×10^{19} cm^{-3}	800 nm
p^+-InGaAsP (Q1.15)	Zn: 1.0×10^{19} cm^{-3}	10 nm
p^+-InGaAsP (Q1.26)	Zn: 1.0×10^{19} cm^{-3}	10 nm
p^+-InGaAsP (Q1.46)	Zn: 1.0×10^{19} cm^{-3}	10 nm
p^+-InGaAs	Zn: $1.0 \times 10^{19} \rightarrow 2.0 \times 10^{17}$ cm^{-3}	40 nm
n.i.d.-InGaAs	non-intentionally doped	70 nm
n^--InGaAsP (Q1.46)	Si: 1.0×10^{16} cm^{-3}	10 nm
n^--InGaAsP (Q1.26)	Si: 1.0×10^{16} cm^{-3}	10 nm
n^--InGaAsP (Q1.15)	Si: 1.0×10^{16} cm^{-3}	10 nm
n^--InP	Si: 1.0×10^{16} cm^{-3}	280 nm
n^+-InGaAsP (Q1.26)	Si: 2.0×10^{18} cm^{-3}	290 nm
n^+-InP	Si: 5.0×10^{18} cm^{-3}	1500 nm
s.i.-InP	Fe-compensated	125 µm

Fig. 2.26: Schematic view of the developed TTR-PD (a) with band diagram (b) and layer structure (c) [requests copyrights].

Top-down, it consists of a highly p-doped InP upper cladding layer (800 nm) which also serves as a diffusion blocker for electrons. This is followed by three 10 nm thick highly p-doped electric field clamp layers, which were introduced between the upper InP cladding layer and an undepleted InGaAs absorber (40 nm). Furthermore, there is a 70 nm thick depleted InGaAs absorber that acts as electric field booster for the graded p-doped absorber. This is to ensure that the electric field in the graded p-doped absorption layer is always higher than the critical electric field. Thus, electron drift in the p-doped absorber determines the transit time rather than slow electron diffusion as it is the case in UTC and MUTC diodes. Thanks to the three clamp layers between the upper InP cladding and the undepleted InGaAs absorber, strong electric fields beyond the critical electric field and thus overshoot velocity is maintained even for high optical input intensities. In addition, the clamp layers also reduce carrier trapping at the InP/InGaAs interface [102], which further enhances the overall transit time. Below the 70 nm thick depleted InGaAs absorber, three 10 nm thick slightly n-doped InGaAsP layers functioning as electric field balancing layers between the InGaAs field booster layer and the slightly n-doped InP collector layer (280 nm). Furthermore, these bridging InGaAsP layers are used for handling the band discontinuity [102].

As discussed above and as can be derived from the name "triple transit region", there are three transit sections contributing to the drift motion of electrons for enhancing the transit time limited bandwidth. In contrast to MUTC-PDs [99] and UTC-PDs [103], there are strong electric fields even in the undepleted absorption layer (overshoot launcher) of the TTR diode, which exceed the critical electric field in InGaAs of 3 kV/cm [104]. Thus, drift motion at overshoot velocity of about 6.1×10^6 cm/s instead of electron diffusion distinguishes the overshoot launcher of the TTR structure from the doped absorber in MUTC or UTC diodes. [100],[103].

For a theoretical study of the electric fields and velocities in the different layers of the TTR diode, numerical simulations based upon the drift-diffusion-model (DDM) were performed [101]. Fig. 2.27 shows the electric field and the resulting carrier velocities across the TTR diode at a reverse bias of 8 V.

As can be seen in Fig 2.26 b), the three InGaAsP clamp layers ensure that the electric field strength in the absorber always exceeds the critical electric field even at high optical excitation. Thus, even for very high optical intensities up to 500 kW/cm^2, the electron velocity remains in the regime of ballistic transport (> $6.1 \cdot 10^6$ cm/s). Also in the intrinsic and quasi-intrinsic InGaAs and InP regions, electrons drift at the saturation velocity of $5.4 \cdot 10^6$ cm/s and $7.5 \cdot 10^6$ cm/s, respectively [105]. For the holes, relaxation can be assumed for the undepleted absorption layer, whereas in the depleted absorber, holes will drift at a somewhat slower velocity of ~$4.8 \cdot 10^6$ cm/s. Only at optical intensity levels exceeding 500 kW/cm^2 and due to the resulting accumulation of holes and electrons in the depleted absorber, the electric field will fall below the critical electric field level leading to saturation effects.

Experimentally, TTR diodes achieved broadband operation with a 3 dB bandwidth beyond 110 GHz as well as output power levels exceeding 0 dBm. Related output RF power measurements at 110 GHz are plotted in Fig. 2.28 and were reported in [101].

Furthermore, TTR diodes were integrated on-chip with planar semicircular bow-tie antennas (SCBTAs) as reported in [105]. Here, a wireless operation within 200-300 GHz, along with a 6 dB bandwidth, was demonstrated for the SCBTA-integrated TTR diodes as shown in Fig. 2.29.

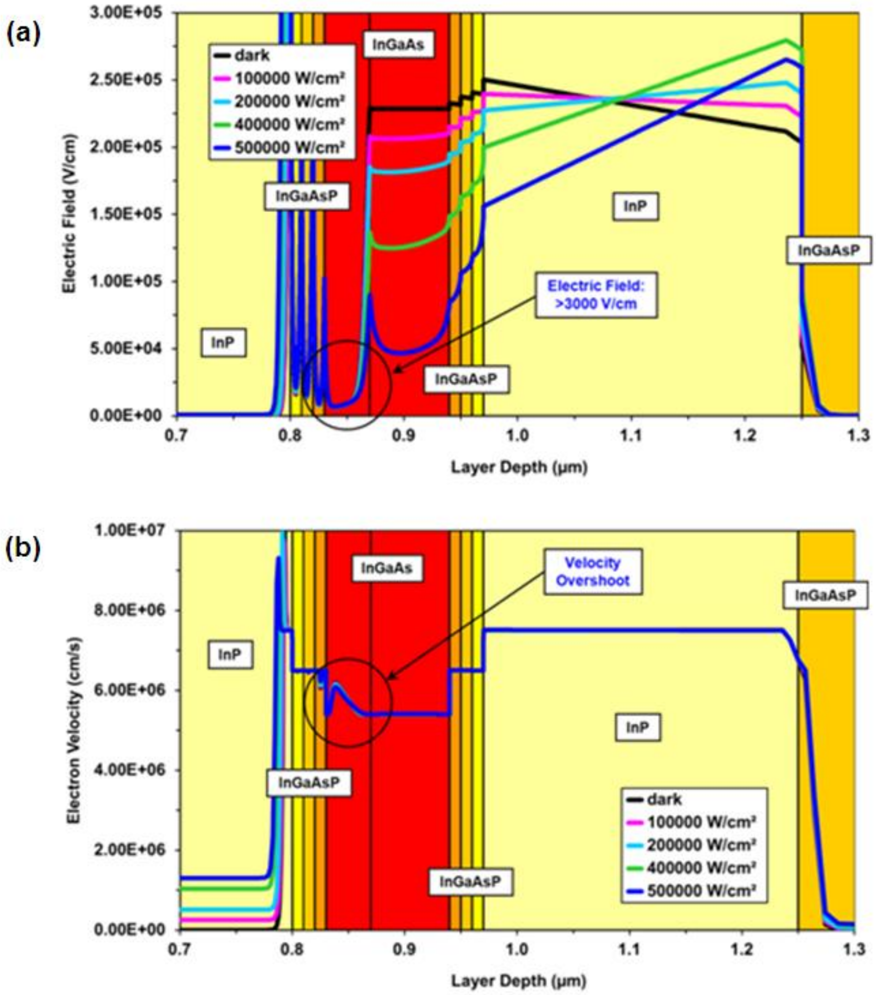

Fig.2.27: Electric field (a) and electron velocity (b) across the TTR diode at different optical intensity levels for a reverse bias of 8 V [requires copyright]

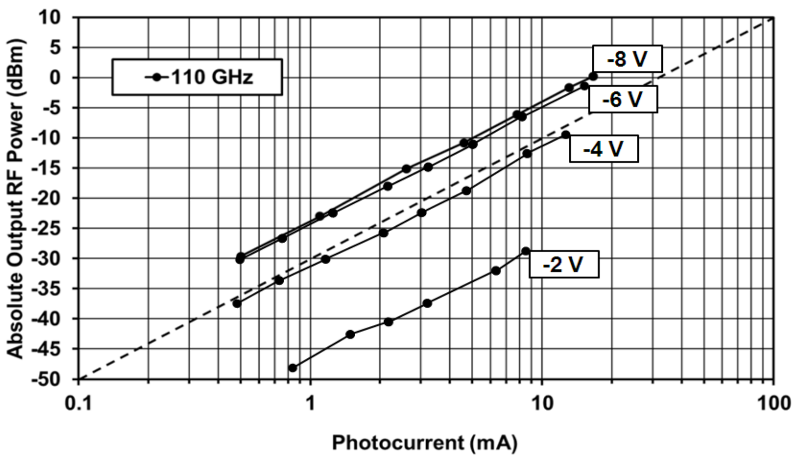

Fig. 2.28: Output RF power at 110GHz versus the photocurrent measured for different drive voltages [requires copyright].

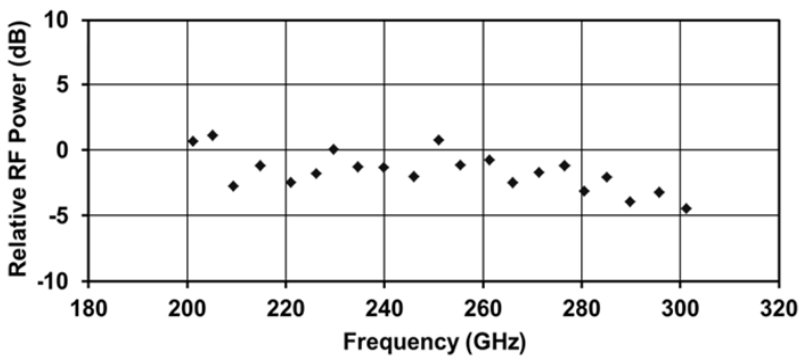

Fig. 2.29: 200-300 GHz operation of TTR diodes with integrated planar semicircular bow-tie antennas [requires copyright].

2.2.6.3 N-i-pn-i-p superlattice diodes

The previous designs of p-i-n diode based photomixers are optimized for high THz powers at lower THz frequencies. The n-i-pn-i-p superlattice diodes, in contrast are explicitly optimized for transit-time free operation up to 1 THz. For operation above a few 100 GHz, all previous concepts have a trade-off between transit-time and RC limitation: The transit-time is given by the transport layer length divided by the average transport velocity $\tau_{tr} = d_i / \bar{v}$. The transit-time can be reduced by making use of ballistic transport, allowing for peak velocities of the order of 10^8 cm/s and average velocities in the range of $5x10^7$ cm/s for InGaAs.Therefore, a maximum intrinsic layer length of 250 nm can be used for $\upsilon_{tr}^{3dB} = 1/(2\tau_{tr}) = 1$ THz. At the same time, the RC roll-off 3 dB frequency, scales with $(d_i)^{-1}$. For $\upsilon_{RC}^{3dB} = 1/(2\pi RC_{pin}) =$ 1 THz, and $C_{pin} = \varepsilon_0 \varepsilon_r A / d_i$, a device with a cross section of 50 µm² and an antenna resistance of only 27 Ω (resonant half wave dipole on InP-air interface), an intrinsic layer length of d_i=975 nm would be required. This is in conflict with the previous value of 250 nm for the transit-time 3 dB frequency. Smaller device cross sections, A, would allow to reduce the capacitance, and, hence, increase the RC 3 dB frequency accordingly, however, at the cost of maximum current, $I_{max}=j_{max}A$, and therefore THz power. A way out of this dilemma is the n-i-pn-i-p superlattice photomixer concept: The capacitance can be reduced without affecting the intrinsic layer length and the device cross section by connecting a number N of p-i-n diodes in series. The capacitance decreases as $C_{SL}=C_{pin}/N$. Only N=4 periods are required in order to shift the RC 3 dB frequency above 1 THz for the same device parameters as above. The serial connection is obtained by stacking N p-i-n diodes during growth. A band diagram is depicted in Fig. 2.30.

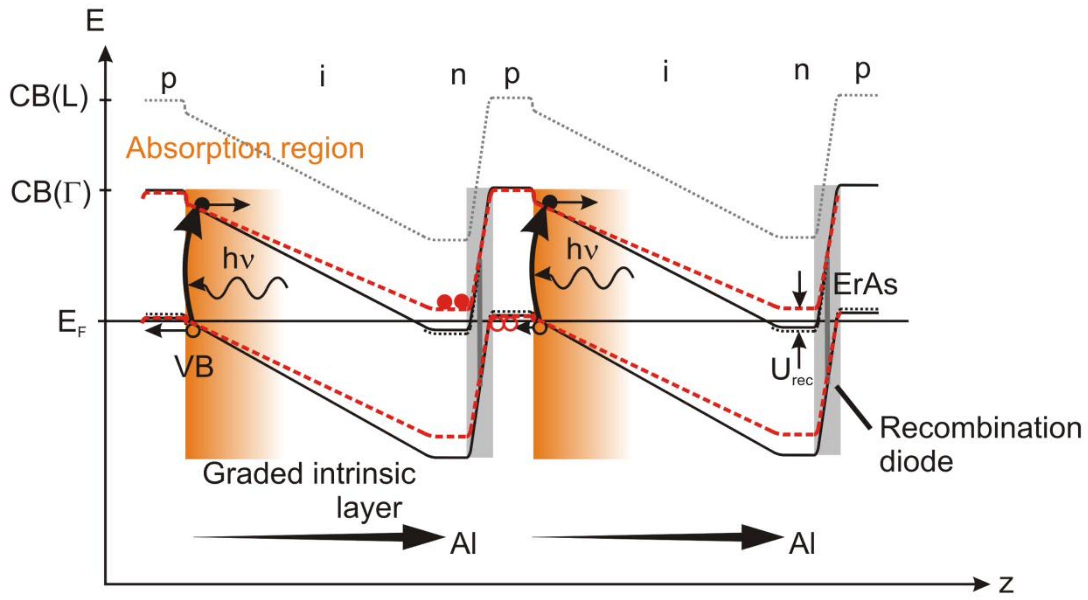

Fig. 2.30: Band diagram of a n-i-pn-i-p superlattice photomixer (N=2). Conduction band, valence band and L-sidevalley (dotted) are shown. The dashed line depicts the band diagram under illumination. A small forward bias, U_{rec}, evolves at the recombination diodes due to charge accumulation. The bias is only a fraction of the bandgap voltage.

Between the p-i-n diodes, an np junction is formed. Both optically generated electrons and holes accumulate left and right of the resulting barrier. In order to prevent a flat band situation by charge accumulation, the np junction is designed as a highly efficient recombination diode that allows for recombination of electrons and holes. High recombination current densities at low forward bias (~tens of kA/cm² at a fraction of the band gap voltage for InAlGaAs based devices [107]) are achieved by implementing 1-2 monolayers of semi-metallic ErAs between the highly doped n and p layer. In order to supply the same optical power to each p-i-n diode, *N* times higher optical power is required for the same photocurrent as in a single p-i-n diode. However, optical power at 1550 nm is usually not a problem due to the availability of high power laser diodes and EDFAs.

The n-i-pn-i-p superlattice photomixing concept has been demonstrated both for 850 nm operation (AlGaAs-based devices [23]) and 1550 nm operation (InAlGaAs based device [108]). The about twice larger band gap in AlGaAs-based devices, however, reduces the current density of the recombination diodes exponentially. Still, sufficiently high recombination currents in the range of 6 kA/cm² at 1 V bias could be demonstrated [109]. Further, the n-i-pn-i-p superlattice makes full use of ballistic enhancement. Due to the larger inter-valley energy, InGaAs-based devices are more successful than GaAs devices. In order to prevent scattering, no transitions from InGaAs to InP are implemented, the whole structure consists of In(Al)GaAs. The absorption region is confined to the p-side by smoothly increasing the Aluminum content of the InAlGaAs intrinsic (transport) layer. The maximum Aluminum concentration is kept below ~10% since the inter valley energy (and therefore the maximum ballistic velocity) decreases with increasing Al-content. For a transport length of 200 nm, a transit-time 3 dB frequency of 0.85 ± 0.15 THz has been determined.

The quarternary compound, however, features a fairly small thermal conductance ($\lambda_{InAlGaAs} < \lambda_{InGaAs} = 0.05$ W/Kcm), limiting the current density to about 15 kA/cm². The n-i-pn-i-p superlattice photomixer therefore produces less output power at frequencies below the transit-time 3 dB frequency of UTC diodes (typically of the order of $\upsilon_{tr,UTC}^{3dB} \sim 200$ GHz) but is an excellent emitter at frequencies a few times above $\upsilon_{tr,UTC}^{3dB}$ where the smaller current density is compensated by the excellent transit-time performance. With a self-complementary broadband logarithmic spiral, a THz power of 0.65 μW at a photocurrent of 9.5 mA has been obtained with a N=3 period device. Under extreme operation conditions in thermal and electrical saturation, the power could be increased to 0.8 μW (17 mA photocurrent), as illustrated in Fig. 2.31. With a resonant antenna, more than 3 μW can be estimated. At low frequencies (~75 GHz), a larger device with a broadband logarithmic-periodic antenna produced about 0.2 mW without any specific optimization.

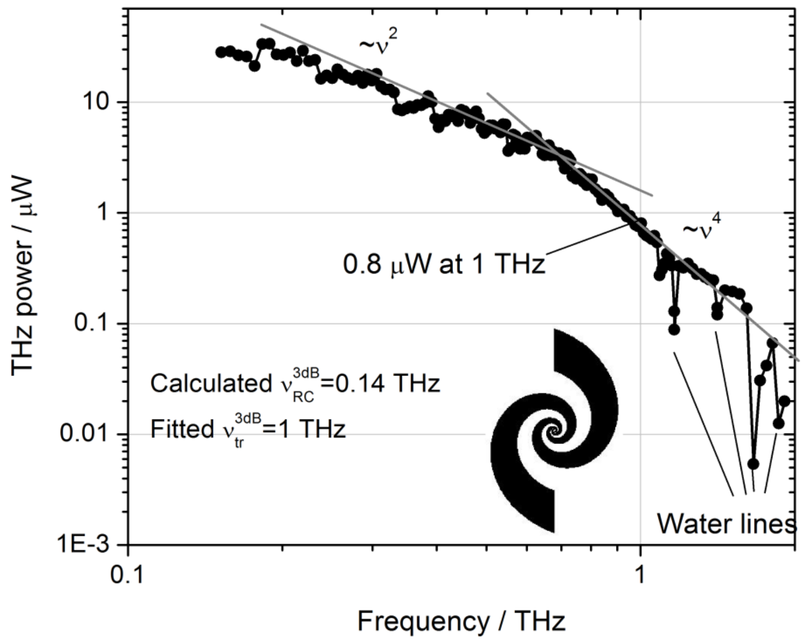

Fig. 2.31: Power spectrum emitted by a logarithmic spiral by a 3 period n-i-pn-i-p superlattice photomixer. A fairly large device with a cross section of 82 μm² was used, resulting in an RC 3 dB frequency of 140 GHz. The represented values are corrected for 30% reflection of the silicon lens. The inset shows a schematic of the spiral antenna.

2.3. Principles of Electronic THz Generation

(M. Feiginov)

Generation of radiation by electronic means is a fairly advanced and well studied topic, however, with still a lot of active research, particularly in engineering. Electric and electronic generation of electromagnetic radiation dates back to the early experiments by Heinrich Hertz who succeeded to transmit electromagnetic signals for the first time. In the mean time, a rich spectrum of electronic sources and detectors has been developed, yet covering frequencies up to the THz range. In the microwave range, a large variety of powerful oscillators and amplifiers have been developed, with W-level output powers [110],[111]. Oscillators include Gunn diodes, impact ionization avalanche transit time (IMPATT) diodes, or tunnel-injection transit-time (TUNNETT) devices with still mW power levels at 300 GHz [112]. Monolithic millimeter wave integrated circuits (MMICs) can be realized with transistor-based oscillators and amplifiers; the active elements are, for instance, high electron mobility transistors (HEMTs; based on III-V semiconductors), heterojunction-bipolar transistors (HBTs; SiGe or III-V devices), and field effect transistors (FETs). There are efforts to shift the operation frequency of these devices towards Terahertz frequencies. In the European DOTFIVE project [113], the development of SiGe HBTs with a maximum frequency of 0.5 THz was successfully demonstrated [114]. Its follow up, DOTSEVEN [115] aims for SiGeC HBT development with an f_{max}=0.7 THz. Also III-V-based transistors are able to reach similar frequencies. Maximum frequencies f_{max}=0.8 THz and 1.1 THz have been reported in refs. [116] and [117]. The improvement of these devices is mainly incremental by trying to overcome technological limits such as minimum structure size, reduction of access resistance and unwanted capacitances and inductances etc. The main design issues and concepts are already covered by other books [118]. Some scaling laws are presented in [119]. In the following, we will give a brief overview over other room temperature operating approaches that are used for Terahertz systems. Details on the systems follow in Chapters xxx and xxx.

2.3.1 Oscillators with Negative-Differential-Conductance

Let us assume that we have a resonant circuit consisting of an inductor (L) and capacitor (C) connected in parallel, see Fig.2.32.a. In the ideal case, such a resonant circuit is lossless and, if we excite some oscillations in the circuit, the circuit will oscillate forever, see Fig.2.32.b. In reality of course, all resonant circuits have losses. We can represent the losses by a resistor R connected in parallel to the circuit, see Fig.2.32.c. Due to the resistor, the oscillations in the resonant circuit will attenuate with time, see Fig.2.32.d. However, if we have a magic device, a negative resistor (R_D), we can use it to compensate for the losses in the resonant circuit, see Fig.2.32.e. If the negative resistor R_D has sufficiently low value (sufficiently high negative conductance), then the total combined value (R') of the resistors R and R_D will be negative, see conditions in Fig.2.32.e. The amplitude of the oscillations excited in the resonant circuit will be growing with time in this case. Small-amplitude initial seed oscillations are always present in the electronic circuits, particularly noise could be the source of such oscillations. The seed oscillations are then amplified by the negative resistor and, following transient oscillations, the circuit comes to a regime with stable large-amplitude oscillations. In such a way, a negative resistor can turn a simple lossy resonant circuit into an oscillator.

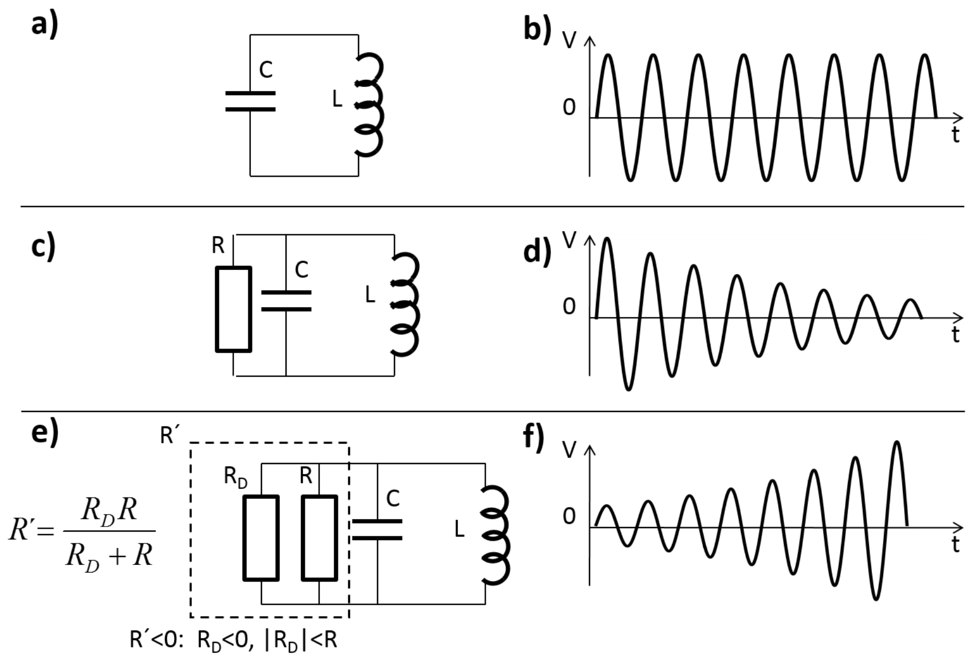

Fig.2.32: Ideal (a,b) and lossy (c,d) LC resonant circuits. (e,f) Resonant circuit with a negative resistor.

Such resonant circuits with negative resistors are, probably, the simplest existing oscillators. The simplicity of the oscillators allows to reduce its dimensions and to use the concept at very high and in meanwhile even THz frequencies. Instead of LC resonant circuit with lumped-element inductor and capacitor, one usually uses resonators based on hollow waveguides or planar resonant antennas, like slot, patch and other types of antennas. At high and particularly THz frequencies, the resonators have to be miniaturised, their characteristic length scale is roughly determined by the wavelength at the given oscillation frequency. The free-space half wavelength at 1 THz is 150 µm. If the resonator is immersed into a dielectric media or the device with the negative resistor has a high inherent capacitance, then the characteristic dimensions of the THz oscillators should be reduced and they are usually on the scale of several tens of micrometres. Since such oscillators include all the necessary elements within their resonators, the oscillators are one of the most compact, if not the most compact, type of THz sources.

To make such oscillators, we need to be able to realise the magic devices with negative resistance in practise. Luckily, this is possible. There are few tunnel semiconductor devices with very particular I-V curves, sketched in Fig.2.33. The I-V curves have regions with negative differential conductance (NDC). If we apply a dc bias to such devices, so that they are biased in the NDC region, then their small-signal AC resistance will be negative and they could be used to make oscillators.

Resonant-tunnelling diodes (RTDs) [120], [121] are double-barrier tunnel semiconductor structures. Their two barriers are very close one to another so that the barriers form a quantum well (QW) between them, see Fig.2.33.a. The mechanism of the electron transport through the barriers is resonant tunnelling through the quantised subbands in the QW. As a consequence, their I-V curve has an N-type shape with NDC region, see Fig.2.33.b. RTDs will be discussed in detail in Chapter 6.

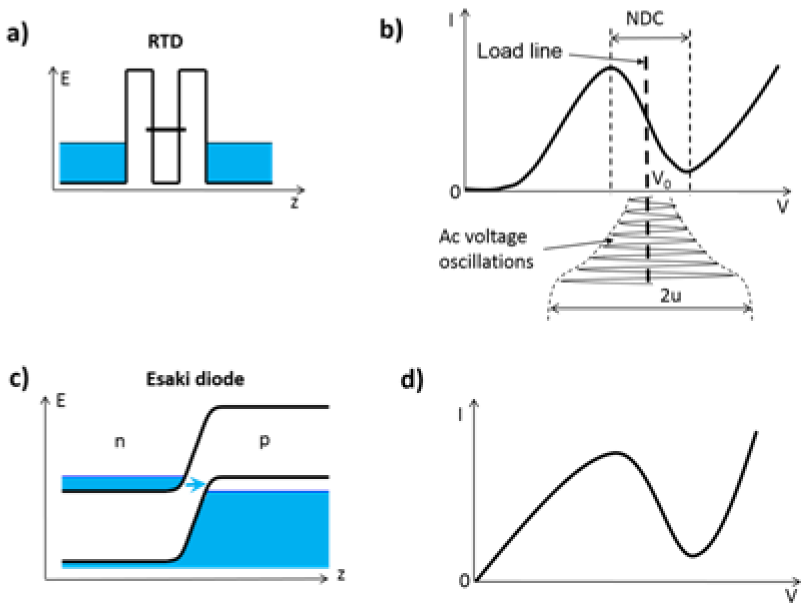

Fig.2.33. Band diagrams (a,c) and typical I-V curves (b,d) of RTDs (a,b) and Esaki (c,d) diodes.

Another type of devices with NDC is the Esaki diode [122]. The diode includes a p-n junction with very high doping level in the adjacent p and n regions, see Fig. 2.33.c. The electrons can tunnel between p and n regions due to inter-band tunnelling, since the transition layer between p and n regions is very thin in such diodes. At low biases, the electrons can tunnel from n region into the empty states in the p region above the quasi-Fermi level there. The tunnel current grows with increase of bias in this regime, see Fig. 2.33.d. At higher biases, the bottom of the conduction band in the n region gets higher than the top of the valence band in the p region. The elastic inter-band tunnelling becomes impossible in this regime and the current drops. This leads to appearance of the NDC region in the I-V curve. With further increase of bias, the electrons can flow from the n region to the p-region due to thermal excitation and the diode current starts to grow again. That explains the particular form of the diode's I-V curve sketched in Fig. 2.33.d.

The above devices rely on the tunnel mechanism of electron transport. Tunnelling can be, in principle, an extremely fast process. Therefore the devices should be able to operate at very high frequencies. Indeed, the oscillators with RTDs are working at THz frequencies nowadays and RTDs are the highest-frequency active electronic devices which exist presently [124][125].

When the amplitude of the initial oscillations in an RTD (or Esaki diode) is growing with time, the AC voltage oscillation amplitude becomes larger than the NDC region, indicated in Fig.2.33.b by the dashed lines. The voltage swing extends into positive-differential-conductance regions of the RTD I-V curve. The resulting averaged AC differential conductance of an RTD becomes less negative and the amplitude of the oscillations grows slower and eventually stabilises at a certain level. The behaviour of RTDs is essentially non-linear in the regime of stable oscillations.

There are not many known tunnel devices with NDC, apart from RTDs and Esaki diodes. Superlattices [126] is the best known example of other structures, although superlattice oscillators can operate only at sub-THz frequencies so far. There are also few other novel concepts, like tunnelling between two graphene layers [127], tunnel Schottky structures with 2-dimensional channel [128] and few other, although applicability of the structures for sub-THz or THz generation still remains to be proven.

Another example for negative differential conductance devices are Gunn diodes and impact ionization avalanche transit time (IMPATT) diodes. These devices perform excellently in the microwave range where they are frequently used as power sources. However, they are typically not used as fundamental oscillators above 100 -150 GHz.

2.3.2. Multipliers (Schottky Diodes, Hetero-Barrier Varactors)

In the last years and due to the increasing number of applications in the THz band, the needs of power sources operating at high frequencies is becoming crucial for the success of such applications. Up to ~150 GHz this need can be satisfied with fundamental all-solid-state local sources such as Gunn or IMPATT oscillators. Output powers in the order of several hundreds of mWatts to a few W can be achieved with these devices. Nevertheless when frequency increases up to several THz, these solid state fundamental oscillators are not able to provide power and therefore other alternatives have to be implemented.

In this case, frequency multipliers are one of the best options. Frequency multipliers are non-linear devices that generate a specific harmonic of an input signal. In principle, any nonlinear impedance can be used to generate such frequency harmonics; however, variable capacitance or varactor diodes present better efficiency and power handling capabilities than variable resistance or varistor diodes. An input and output matching network is required at the desired harmonic to maximize the transferred power from the input signal. This requirement becomes difficult to comply with when the order of the harmonic is high; in fact, rarely over four or five times the source frequency [129].

The nonlinear behavior is achieved through the use of non-symmetrical devices like Schottky diodes [130], or symmetrical devices like heterostructure barrier varactors (HBVs) [131]. Note that Schottky structures are usually not used for multiplication factors higher than N=4. In both cases, a nonlinear capacitance or varactor is used to generate the higher harmonics. These multipliers generally take the form of doublers (x2) or triplers (x3). Nevertheless when higher frequencies are needed, the solution is a combination of several of them (cascades of multipliers) to achieve higher multiplication factors.

Schottky diodes are the preferred device for building frequency multipliers mainly due to the simplicity in the fabrication process. In fact, when the operating frequency increases it is possible to reduce the size of the active area of the diode during fabrication process in order to improve its main parameters, such as the junction capacitance, parasitic capacitances and series resistance. The value of these parameters needs to be reduced to operate at THz frequencies.

On the other hand, hetero barrier varactor (HBV) structures present current-voltage symmetry which simplifies the circuit topology since only odd harmonics ($(2n+1)f_c$) are produced and no bias is needed [132]. Nevertheless, HBV diodes require a complex material engineering process to reduce the active area and therefore achieve good performances at THz frequencies.

In general, there is an important drawback in the THz multiplier systems; with each multiplication step, the output power is much less than the input power due to the very low conversion efficiency (typically 0.5-30% [133]). This efficiency is reduced as the operational frequency is increased. Furthermore, the matching requirements between different multiplier stages limit the operational bandwidth of the multiplier chain. A possible solution to short out the low efficiency problem is the use of balanced doublers that share the input power between several diodes. This configuration is able to provide efficiencies in the order of 50% [134]. On the other hand, HBV diodes, due to the cancelling of even harmonics, allow to work with higher harmonics, such as the 5th and 7th. Besides, HBV devices provide the handling of higher input powers when compared with Schottky diode technology, which is an important advantage in order to achieve higher output powers.

In general, two types of multipliers have to be distinguished; broadband and narrow band. The first ones are able to cover a complete waveguide band, as WR10, WR8, etc, meanwhile the second ones operate in a narrow frequency band. Anyway, narrow band multipliers always offer a higher efficiency and output power levels than broadband configurations.

In Table 1 and 2, the current state of the art of multipliers made of planar GaAs Schottky diode technology (the most typical used in current applications) for output power levels and efficiency values is described; in Table 1 for the case of narrow band multipliers and in Table 2 for the case of broadband multipliers. Note that Table 2 values are for multipliers based on triplers. Fabrication techniques for Schottky diodes will be discussed in Chapter 6.5.

HBVs technology is not yet able to operate at frequencies around 1 THz. Some reported results in literature are 180 mW output power at the W-band (90-110GHz) with efficiencies of 23% [135] or 1 mW at 450 GHz with efficiencies below 2% [136].

TABLE 1
STATUS OF MULTIPLIERS: NARROW BAND OPERATION

Frequency	Output Power	Efficiency	Typical 3dB bandwidth
250GHz	80-100mW	20-25%	≅8%
400GHz	≅10mW	<10%	≅4%
500GHz	<70mW	<7%	<4%

TABLE 2
STATUS OF MULTIPLIERS: BROADBAND OPERATION

Frequency	Output Power	Efficiency
260-400GHz	<5mW	<4%
400-600GHz	<3mW	<4%
600-900GHz	<300μW	<5%
750-1100GHz	<200μW	<2%
1100-1700GHz	<80μW	<1%
1400-2200GHz	<50μW	<0.6%

RF multipliers are known and being developed for a long time, with a manifold of excellent books on this topic. We refer to ref. [137] for further reading.

2.3.3. MMIC THz Sources

2.3.4. Gunn Diodes

2.3.5 Plasmonic Sources

(R. Gonzalo)

In Section 2.2.5.3 we have already shown examples where plasmons are used to enhance the efficiency of photoconductors. In the following, we will discuss more general applications of plasmons for THz generation.

2.3.5.1 Plasmons

Plasmonics refers to a variety of techniques to generate, control and detect electromagnetic radiation using metals [138]-[140]. The term plasmonics derives from plasmon waves, more commonly called surface plasmons (SPs), which, from a microscopic viewpoint, can be understood as collective electron oscillations that appear at a metal-dielectric interface under external p-polarized electromagnetic illumination.

Alternatively, plasmons can be identified as transversal magnetic (TM) surface waves (bounded modes) that propagate along the interface of two media with opposite signs of the real part of the permittivity. Imposing this boundary condition and forcing bounded surface waves (i.e. evanescent decay towards both media) plasmons can be directly derived from Maxwell's equations obtaining their dispersion relation as well as complex propagation constants (the reader is referred to [141] for a simple and elegant explanation). With this macroscopic perspective, plasmons are classical waves, a member of the more general family of complex waves, which also encompasses leaky waves, surface waves, and, closely related with plasmons, Zenneck waves.

Although plasmonics is a time-honoured topic (the first studies can be found in the works of Zenneck – more than 100 years ago - about electromagnetic propagation on imperfectly conducting planes [142]) it has been revisited in the last decades due to the exciting properties and promising applications envisioned with them, leading to the so-called surface plasmon resurrection [143]. A key property of surface plasmons is that they are confined to the metal-dielectric interface and thus wave-matter interaction is enhanced. Besides, the wavelength of plasmons is smaller than the free-space wavelength beating the diffraction limit, a property that makes plasmons valuable for light manipulation at the nanoscale. In fact, plasmons have been proposed as prominent candidates for merging photonics and electronics, which could enable the long-desired all optics processing in plasmonic chips. All these features make them ideally suited for a variety of applications in fields like biology, optics, material science, nanoelectronics and nanophotonics and recently terahertz (THz) waves [140]. In fact, placed between microwaves and infrared, THz is the natural playground where ideas from both regimes can be successfully applied.

One of the main actors in the resurgence of plasmonics research was the discovery of Extraordinary Optical Transmission (EOT) through subwavelength hole arrays by Ebbesen *et al.* in 1998 [144] and other periodic structures on metals [145], where the explanation for the enhanced transmission was put in terms of light-plasmon coupling. Soon after, similar phenomena were found in other regions of the electromagnetic spectrum such as microwaves/millimeter waves [146],[147] where metals are classically modelled as highly conductive, with a non-dispersive conductivity, rather than plasmonic, which implies a dispersive permittivity modeled with a Drude equation, demonstrating the generality of the phenomenon. Under the high-frequency plasmonic perspective, this was interpreted as a generalization and extension of plasmons to lower frequencies, called “spoof plasmons”, in diluted (i.e. perforated) metals, where periodicity of the array served to tune the plasma frequency [148]. Alternatively, evolving from low frequency concepts EOT was explained in terms of leaky waves excited by the periodic structure [149]. Both explanations are complementary and describe the same phenomenon. The Drude model at low frequency is practically equivalent to a finite conductivity model [150]. On the other hand, a leaky wave excited by a periodic structure becomes a leaky plasmon at sufficiently high frequencies [151]. No matter which explanation is preferred, the important conclusion is that, aside from subtle differences mainly related with the exact metallic model, plasmonics research can benefit from mature techniques borrowed from optics or microwaves to obtain interesting technological realizations [150].

Another important actor in the resurge of plasmonics is the advance in nanofabrication, both bottom-up and top-down processes [152]. Current nanofabrication techniques allow realizing not only texturized surfaces supporting propagating surface plasmons, but also particles of almost any shape with sub-nanometer precision. The latter support localized surface plasmons (LSPs), i.e., collective oscillation of conduction electrons experiencing a restoring force due to the induced surface charges at the boundaries of the particle. Localized surface plasmons hold promise for similar applications as surface plasmons, but specifically, they are becoming key for single molecule spectroscopy [153], local heat generation [154] and nonlinearities [155] as a result of their high field enhancement in sub-wavelength volumes.

A variety of techniques have been proposed for the generation of THz waves where plasmons play a prominent role: nonlinear THz generation based on optical techniques where the use of metals allows relaxing the constraint of phase matching; THz generation based on photoconductive materials benefits from plasmonic resonances and their strong field concentration to enhance the absorption and conversion of photons into electrons as already discussed in Section 2.2.5.3; in modern Quantum Cascade Lasers (QCLs) plasmons play a key role for the performance at THz, both for waveguiding and also beaming capabilities. In the following sections, we will review the main contributions of plasmons in the topic of THz generation.

2.3.5.2. Plasmonic THz generation based on optical nonlinear effects

One of the most popular methods for THz radiation generation is the excitation of nonlinearities employing a pulsed laser of higher frequency, usually in the near infrared (NIR). Two main mechanisms have been identified in the nonlinear process: optical rectification (OR) and multiphoton photoelectron emission (MPE), which have many common aspects but subtle differences as well. OR is a second order nonlinear effect in which broadband THz radiation is generated in a material with second order susceptibility owing to the difference-frequency mechanism among the frequencies components contained in the femtosecond pulse. Consequently, the THz fluence generated depends on the square of the incident laser pump intensity. If the material with second order susceptibility is illuminated with two frequency-offset continuous wave lasers, the difference-frequency mechanism leads to a continuous wave THz radiation as discussed in Section 2.2.1. On the other hand, within the MPE framework, the dependence is of higher order (third-, fourth-, or even higher-order). In this case, THz radiation is mainly linked with multiphoton ionization and ponderomotive[1] acceleration of electrons. Although the debate is not yet closed, it seems that both mechanisms are usually present in the nonlinear-pulsed THz generation, with the main difference being the incident power and/or the repetition rate of the source which can mask either of the mechanisms [156], [157], as will be elucidated at the end of this section.

Historically, the first evidence of THz emission based on OR was reported in the seminal paper of Yang *et al.* in 1971 [158] where a picosecond pulsed laser was used to illuminate a $LiNb0_3$ slab used as the non-linear material to produce THz radiation. Afterwards, the accuracy of the method was enhanced by Auston *et al.* in [159] by using a femtosecond pulsed laser and Lithium Tantalate as the electro-optic medium and was extended later to THz generation using the depletion layer of semiconductors [160]. More efficient techniques such as coherent detection (i.e. amplitude and phase) of the THz radiation [161] using a variety of electro-optic crystals [161], [162] were proposed afterwards, launching definitely the THz generation based on OR. The efficiency of OR and electro-optic detection decisively depends on the so-called phase matching, which currently is achieved by coincidental, birefringent, and non-collinear schemes. Recently OR in organic salt crystals has been explored for extremely intense THz pulses (in the order of MV/cm) covering the full THz gap (0.1 – 10 THz) [163].

[1] A ponderomotive force is a non-linear force exerted by an inhomogeneous oscillating electromagnetic field on a charged particle.

More recently, with the explosion of plasmonics, metals have been also proposed as candidates for non-linear THz generation, in which the constraint of phase matching is relaxed. The first realization of OR employing metals was reported by Kadlec *et al.* [164] with flat silver and gold slabs illuminated by a near infrared pulsed femtosecond laser, obtaining a peak electric field of 200 V/cm and paving the way for the investigation of nonlinearities in metals [165] and the development of novel THz emitters, potentially more compact than previous solutions. In their experiments a second order dependence between the emitted THz fluence and the incident laser pump intensity was obtained and thus OR was identified as the underlying mechanism in THz generation.

In [166] a gold grating instead of a flat metallic surface was investigated. A ZnTe slab was illuminated with a high power pulsed laser source to excite nonlinearities. Experiments at different angles were done and it was observed that maximum THz-pulse fluence appeared near the angle where SPs were excited by the periodic structure under p-polarized illumination, demonstrating the importance of SPs in the efficiency of the nonlinear process. Interestingly, a third-, fourth- or even higher-order dependence of the emitted THz fluence on the incident light was noticed, in sharp contrast with the results of [165]. Therefore, MPE was invoked as the underlying mechanism. It was argued that nanoscale structures are able to interact strongly with light, strengthening the field concentration in very small volumes and enhancing nonlinearities. The study was extended in [167] where it was again explicitly mentioned the involvement of surface plasmons as well as evanescent-wave acceleration of photoelectrons in the THz emission. The coupling of incident photons to SPs causes a high confinement of electromagnetic energy in a very small (subwavelength) area, accompanied by a strong field confinement (i.e. high gradient) at the metal-dielectric interface favoring the MPE process [168].

The strategy of structuring metals was extended in the analytical and numerical study of [169]. There, the performances of several nanostructured metallic surfaces were compared: flat gold films, metal gratings, single nanoparticle and nanoparticle arrays with circular (disks), coaxial and pyramidal shapes. The study demonstrated that THz emission can be optimized by judiciously choosing the nanoparticle parameters, i.e. by tuning the SP resonance of the array. An experimental proof was presented in [170] by comparing semicontinuous (percolated) silver films and ordered arrangements of silver nanoparticles, arrayed as a honeycomb of triangular particles. The SP role in the THz emission was investigated here by modifying the thickness of the silver deposited, which shifts the plasmon resonance demonstrating that the excitation of the plasmon resonance is directly related with an enhancement of the THz emission process. The dependence of THz emission on pump laser intensity was found to be between second and sixth order. Thus MPE was proposed as the underlying mechanism.

However, in [171] percolated silver films were analyzed and a clear second-order dependence was found, giving evidence of OR. Even more intriguing, for a flat metal surface, no THz emission was observed, seemingly contradicting the results of [165]. The answer to these apparent inconsistencies were finally resolved in [156], [157]: when low peak-power laser pulses are used as sources, high-order nonlinearities are faintly excited. However, with a high repetition rate a sensitive lock-in detection of relatively weak signals is possible, and thus second-order nonlinear optical processes, like OR can be detected. On the other hand, high peak power amplified lasers can excite high-order nonlinearities to generate THz pulses. However, these high-power sources usually have a low repetition rate which makes it difficult to detect weak THz pulses from a second-order nonlinear process. In general, both OR and MPE will be present but depending of the characteristics of the sources one of them will dominate in the THz generation process.

Very recently, metamaterials have been proposed for the generation of broadband THz radiation from 0.1 to 4 THz [172]. Screens of split-ring resonators (SRRs) [173] are illuminated with infrared radiation and THz emission emerges through the excitation of the magnetic resonance (SRRs).

2.3.5.3 Applications of plasmonics in quantum cascade lasers

Since their first experimental demonstration at 70 THz [174] by Faist *et al.*, QCLs have become by their own merits one of the most promising sources in THz technology. At difference with the sources discussed in the previous section, QCLs provide direct and powerful CW THz generation.

The fundamentals of QCLs can be found in theoretical works of Kazarinov and Suris in 1971 [175]. The operation principle relies on the emission of THz waves by relaxation of electrons between subbands of quantum wells. The first experimental realization had to wait for more than 20 years [174] and, after formidable efforts, the operation frequency could be finally reduced to 4.4 THz [176] in 2002 by Köhler *et al.*, more than 40 years after the first theoretical study. Since then, research on QCL has evolved spectacularly [177].

A severe hurdle in THz-QCLs is the guidance and confinement of the THz signal. Although metallic waveguides operate with relatively low loss in microwaves and millimeter-waves, it is a fact that metallic losses increase with frequency, deterring its use at THz frequencies [178]. Similarly, dielectric waveguides usually present high loss, since many polymers have absorption bands at these frequencies [178]. An alternative to circumvent these issues is to take advantage of plasmonic concepts developing plasmonic waveguides. The key idea is that by highly doping of semiconductors a negative permittivity can be synthesized. This way, doped semiconductors behave like metals at infrared but with a plasma frequency in the mid- or far-infrared instead of ultraviolet. In fact in the seminal paper of Köhler *et al.* [176], a plasmonic waveguide with superior characteristics than previous designs was synthesized by doping a GaAs semiconductor layer surrounded by an undoped GaAs substrate. Soon after, it was proposed a distributed feedback (DFB) QCL design [179], to improve the single mode operation of the source. This was accomplished by introducing a grating into the doped GaAs layer, imitating infrared lasers, where corrugations are etched on metals. In [180] a different topology for DFB-QCL is analyzed, with a metal-metal ridge waveguide. Moreover, in [181] a periodic array of thin slits etched on a metallic slab is used as a grating for surface plasmons. This is further extended in [182] where the semiconductor is also removed from the slit to avoid coupling of the surface plasmon inside the slit. Further developments of THz-QCL relying on surface plasmons guiding can be found in [183].

Plasmons are also employed to enhance the directivity (beaming) of QCL sources. In [184] a corrugated structure was placed at the output of a mid-infrared QCL, imitating antennas initially developed in microwaves [185], [186] and later evolved at THz frequencies [187]. A similar design was implemented in [188] where a double periodicity structure was proposed: a surface waveguide was designed using a small period corrugated structure; to enhance radiation through leaky waves [151], a larger periodicity was superimposed.

References

[1] FELIX2, Nijmegen, Netherlands, http://www.differ.nl/en/felix/specifications
[2] FELBE, Helmholtz-Zentrum Dresden-Rossendorf, Germany, https://www.hzdr.de/db/Cms?pNid=205
[3] UCSB-FEL, Univeristy of California, Santa Barbara, USA, http://sbfel3.ucsb.edu/
[4] J.M.J. Madey, “Stimulated emission of Bremsstrahlung in a periodic magnetic field”, *J. Appl. Phys.* **42**, p. 1906 (1971)
[5] G. Ramian, “The new UCSB free-electron laser," *Nucl. Instrum & Methods in Phys. Research Section A* **318**, p. 225 (1992)
[6] RPC Istok, Fryazino, Russia, http://www.istokmw.ru/vakuumnie-generatori-maloy-moshnosti/
[7] S. Jacobsson, “Optically pumped far infrared lasers,” *Infrared Phys.* **29**, p. 853 (1989)
[8] G. Dodel, “On the history of far-infrared (FIR) gas lasers: Thirty-five years of research and application,” *Infrared. Phys. & Technol.* **40**, p. 127 (1999)
[9] E. Bründerman, A.M. Linhart, L. Reichertz, H.P. Röser, O.D. Dubon, W.L. Hansen, and E.E. Haller, “Double acceptor doped Ge: A new medium for inter-valence-band lasers,” *Appl. Phys. Lett.* **68**, p. 3075 (1996)
[10] P. Pfeiffer, W. Zawadzki, K. Unterrainer, E. Gornik, C. Kremser, C. Wurzer, B. Murdin, and C.R. Pidgeon, “p-type Ge cyclotron-resonance laser: Theory and experiment,” *Phys. Rev. B* **47**, p. 4522 (1993)
[11] A.V. Muravjov, E.W. Nelson, R.E. Peale, V.N. Shastin, and C.J. Fredrickson, “Far-infrared p-Ge laser with variable length cavity,” *Infrared Physics & Technol.* **44**, p. 75 (2003)
[12] B. S. Williams, S. Kumar, and Q. Hu, “Operation of terahertz quantum-cascade lasers at 164 K in pulsed mode and at 117 K in continuous-wave mode,” *Opt. Express* **13**, p. 3331 (2005)
[13] L. Ajili, G. Scalari, J. Faist, H. Beere, E. Linfield, D. Ritchie, and G. Davies, “High power quantum cascade lasers operating at λ=87 and 130 μm,” *Appl. Phys. Lett.* **85**, p. 3986 (2004)
[14] G. Scalari, C. Walther, M. Fischer, R. Terazzi, H. Beere, D.Ritchie, and J. Faist, “THz and sub-THz quantum cascade lasers,” *Laser & Photonics Reviews* **3**, p. 45 (2009)
[15] K. L. Vodopyanov, “Optical generation of narrow-band terahertz packets in periodically-inverted electro-optic crystals: conversion efficiency and optimal laser pulse format*,” Opt. Express* **14**, p. 2263 (2006)
[16] H. Minamide, S. Hayashi, K. Nawata, T. Taira, J.-I. Shikata, and K. Kawase, “Kilowatt-peak Terahertz-wave generation and sub-femtojoule Terahertz-wave pulse detection based on nonlinear optical wavelength-conversion at room temperature,” *J. Infrared Milli Terahz Waves* **35**, p. 25 (2014)
[17] S. Pine, R. D. Suenram, E. R. Brown, and K. A. McIntosh, “A Terahertz Photomixing Spectrometer: Application to SO2 Self Broadening,” *J. Mol. Spectroscopy* **175**, p. 37 (1996)
[18] S. Preu, G. H. Döhler, S. Malzer, L.J. Wang, and A. C. Gossard, “Tunable, continuous-wave Terahertz photomixer sources and applications,“ *J. Appl. Phys.* **109**, p. 061301 (2011)
[19] Materials parameters for various semiconductors taken from www.ioffe.ru\SVA\NSM\Semicond\index.html and references thereof
[20] Y. A. Goldberg and N.M. Schmidt *Handbook Series on Semiconductor Parameters*. 2nd ed., M. Levinshtein, S. Rumyantsev and M. Shur, ed., London: World Scientific, 1999, p. 62
[21] S. Adachi, *GaAs and Related Materials.* Singapore: World Scientific, 1994
[22] S. Adachi, *Physical properties of III-V semiconductor compounds.* New York: John Wiley & Sons, 1992

[23] G. H. Döhler, F. Renner, O. Klar, M. Eckardt, A. Schwanhäußer, S. Malzer, D. Driscoll, M. Hanson, A. C. Gossard, G. Loata, T. Löffler, and H. Roskos, "THz-photomixer based on quasi-ballistic transport," *Semicond. Sci. Technol.* **20**, p. 178 (2005)
[24] E.R. Brown, "THz Generation by Photomixing in Ultrafast Photoconductors*," Int. J. High Speed Electron. and Systems* **13**, 497 (2003)
[25] P. Benicewicz, J.P. Roberts, and A.J. Taylor, "Scaling of terahertz radiation from large-aperture biased photoconductors," *J. Opt. Soc. Am. B* **11**, p. 2533 (1994)
[26] P.U. Jepsen, D. G: Cooke, and M. Koch, "Terahertz spectroscopy and imaging-modern techniques and applications," *Laser Photonics Rev.* **5**, p. 124 (2011)
[27] M. Ashida, "Ultra-broadband Terahertz wave detection using photoconductive antenna," *Jpn. J. Appl. Phys.* **47**, p.8221 (2008)
[28] S. Preu, *"A unified derivation of the Terahertz spectra generated by photoconductors and diodes,"* submitted to J. Infrared Milli THz Waves (2014)
[29] C. A. Balanis, *Antenna Theory: Analysis and Design*, 3rd ed., John Wiley & Sons, New Jersey (2005)
[30] P. Bhattacharya, Ed., *Properties of Lattice-Matched and Strained Indium Gallium Arseni*de. New York: Inspec, 1993
[31] S. Verghese, K. A. McIntosh, and E. R. Brown, "Optical and terahertz power limits in the low-temperature-grown GaAs photomixers," *Appl. Phys. Lett.* **71**, p. 2743 (1997).
[32] H.Ito, F. Nakajima, T. Futura, and T. Ishibashi, "Continuous THz-wave generation using antenna-integrated uni-travelling-carrier photodiodes," *Semicond. Sci. Technol.* **20**, p. 191 (2005).
[33] A. Beck, G. Ducournau, M. Zaknoune, E. Peytavit, T. Akalin, J.F. lampin, F. Mollot, F. Hindle, C.Yang, and G. Mouret, "High-efficiency uni-travelling-carrier photomixer at 1.55 μm and spectroscopy application up to 1.4 THz," *Electron. Lett.* **44**, p. 1320 (2008)
[34] J. E. Bjarnason, T. L. J. Chan, A. W. M. Lee, E. R. Brown, D. C. Driscoll, M. Hanson, A. C. Gossard, and R. E. Muller, *"*ErAs:GaAs photomixer with two-decade tunability and 12 W peak output power," *Appl. Phys. Lett.* **85**, p. 3983 (2004)
[35] P. Latzel, E. Peytavit, E. Dogheche, and J.-F. Lampin, "Improving properties of THz photoconduetors by bonding to a high thermal conductivity substrate," *36th International Conference on Infrared, Millimeter and Terahertz Waves (IRMMW-THz)*, p. 1 (2011)
[36] S. Preu, F. H. Renner, S. Malzer, G. H. Döhler, L. J.Wang, T. L. J. Wilkinson, E. R. Brown, M. Hanson, and A. C. Gossard, "Efficient Terahertz emission from ballistic transport enhanced n-i-p-n-i-p superlattice photomixers," *Appl. Phys. Lett*. **90**, p. 212115 (2007)
[37] E. Rouvalis, C. C. Renaud, D. G. Moodie, M. J. Robertson, and A. J. Seeds, "Traveling-wave uni-traveling carrier photodiodes for continuous wave THz generation," *Opt. Express* **18**, p. 11105 (2010)
[38] T. Ishibashi, T. Furuta, H. Fushimi, S. Kodama, H. Ito, T. Nagatsuma, N. Shimizu, and Y. Miyamoto, "InP/InGaAs uni-traveling-carrier photodiodes*," IEICE Trans. Electron.* **E83-C**, p. 938 (2000)
[39] D. Stanze, H.-G. Bach, R. Kunkel, D. Schmidt, H. Roehle, M. Schlak, M. Schell, and B. Sartorius, "Coherent CW Terahertz Systems Employing Photodiode Emitters," *34th International Conference on Infrared, Millimeter, and Terahertz Waves, IRMMW-THz 2009*, p. 1 (2009)
[40] J. T. Darrow, X.-C. Zhang, D. H. Auston , J.D. Morse "Saturation Properties of large-aperture photoconducting antennas," *IEEE J. Quant. Electron.* **28**, p. 1607 (1992)
[41] P. U. Jepsen, D. G. Cooke, and M. Koch, "Terahertz spectroscopy and imaging – Modern techniques and applications," *Laser Photonics Rev.* **5**, p. 124 (2011)

[42] G. C. Loata, T. Löffler, and H. G. Roskos, “Evidence for long-living charge carriers in electrically biased low-temperature-grown GaAs photoconductive switches,”*Appl. Phys. Lett.* **90**, p. 052101 (2007)
[43] G. Segschneider, F. Jacob, T. Löffler, H. G. Roskos, S. Tautz, P. Kiesel, and G. H. Döhler, “Free-carrier dynamics in low-temperature-grown GaAs at high excitation densities investigated by time-domain terahertz spectroscopy,” *Phys. Rev. B* **65**, p. 125205 (2002)
[44] D. S. Kim and D. S. Citrin, “Coulomb and radiation screening in photoconductive terahertz sources,” *Applied Physics Letters* **88**, p. 161117 (2006)
[45] M. Awad, M. Nagel, H. Kurz, J. Herfort, and K. Ploog, “Characterization of low temperature GaAs antenna array terahertz emitters ,” *Appl. Phys. Lett.* **91**, 181124 (2007).
[46] M. Tani, S. Matsuura, K. Sakai, and S.-I.Nakashima, “Emission characteristics of photoconductive antennas based on low-temperature-grown GaAs and semi-insulating GaAs,“ *Appl. Opt.* **36**, p. 7853 (1997)
[47] C. W. Berry and M. Jarrahi ,”Principles of impedance matching in photoconductive antennas,“ *J. Infrared Milli Terahz Waves* **33**, p. 1182 (2012)
[48] H. Ito, T. Nagatsuma, A. Hirata, T. Minotani, A. Sasaki,Y. Hirota, and T. Ishibashi, “High-power photonic millimetre wave generation at 100 GHz using matching-circuit integrated uni-travelling-carrier photodiodes,” *IEE Proc. Optoelectron.* **150**, p. 138 (2003).
[49] E. Peytavit, P. Latzel, F. Pavanello, G. Ducournau, and J.-F. Lampin, “CW Source Based on Photomixing With Output Power Reaching 1.8 mW at 250 GHz,“ IEEE *Electron. Dev. Lett.* **34**, p. 1277 (2013)
[50] J. Liu, S. Zou, Z. Yang, K. Wang K. Ye, “Wave shape recovery for terahertz pulse field detection via photoconductive antenna,” *Opt. Lett.* **38**, p. 2268 (2013)
[51] G.C. Loata, M. D. Thomson, T. Löffler, and H. G. Roskos, ”Radiation field screening in photoconductive antennae studied via pulsed terahertz emission spectroscopy,” *Appl. Phys. Lett.* **91**, 232506 (2007)
[52] T. Hattori, K. Tukuamoto, and H. Nakatsuka, “Time-resolved study of intense Terahertz pulses generated by a large-aperture photoconductive antenna,“ *Jpn. J. Appl. Phys.* **40**, p. 4907 (2001)
[53] G. Rodriguez and A. J. Taylor,”Screening of the bias field in terahertz generation from photoconductors,” *Opt. Lett.* **21**, p. 1046 (1996)
[54] M. Beck, H. Schäfer, G. Klatt, J. Demsar, S. Winnerl, M. Helm and T. Dekorsy, ”Impulsive terahertz radiation with high electric fields from an amplifier-driven large-area photoconductive antenna,” *Opt. Express* **18**, p. 9252 (2010)
[55] D.L. Rogers,“Integrated Optical Receivers using MSM Detectors,“ *J. Lightw. Technol* **9**, p. 1635 (1991)
[56] I.S. Gregory, C. Baker, W. R. Tribe, M.J. evans, H.E. Beere, E.H. Linfield, A.G. Davies, and M. Missous, “High resistivity annealed low-temperature GaAs with 100 fs lifetimes,” *Appl. Phys. Lett.* **83,** p. 4199 (2003)
[57] E. R. Brown, K. A. McIntosh, K. B. Nichols, and C. L. Dennis, “Photomixing up to 3.8 THz in low-temperature-grown GaAs,” *Appl. Phys. Lett.* **66**, p. 285 (1995)
[58] S. Hisatake, G. Kitahara, K. Ajito, Y. Fukada, N. Yoshimoto, and T. Nagatsuma, „Phase-Sensitive Terahertz Self-Heterodyne System Based on Photodiode and Low Temperature-Grown GaAs Photoconductor at 1.55 μm,” *IEEE Sensors* **13**, p. 31 (2013)
[59] M. Tani, K.-S. Lee, and X.-C. Zhang, “Detection of terahertz radiation with low-temperature-grown GaAs-based photoconductive antenna using 1.55μm probe,”*Applied Physics Letters* **77**, p. 1396 (2000)
[60] C. Kadow, J. A. Johnson, K. Kolstad, J. P. Ibbetson, and A. C. Gossard, “Growth and microstructure of self-assembled ErAs islands in GaAs,” *J. Vac. Sci. Technol. B* **18**, p. 2197 (2000)

[61] C. Kadow, A. W. Jackson, A. C. Gossard, S. Matsuura and G. A. Blake, "Self-assembled ErAs islands in GaAs for optical-heterodyne THz generation," *Appl. Phys. Lett.* **76**, p. 3510 (2000)
[62] M. A. Scarpulla,J.M. O. Zide, J. M. LeBeau, C. G. Van de Walle, A. C. Gossard, and K. T. Delaney, "Near-infrared absorption and semimetal-semiconductor transition in 2 nm ErAs nanoparticles embedded in GaAs and AlAs," *Appl. Phys. Lett.* **92**, 173116 (2008)
[63] C. Kadow, J. A. Johnson, K. Kolstad, and A. C. Gossard, "Growth-temperature dependence of the microstructure of ErAs islands in GaAs," *J. Vac. Sci. Technol. B* **21**, p. 29 (2003)
[64] C. Kadow, S. B. Fleischer, J. P. Ibbetson, J. E. Bowers, A. C. Gossard, J. W. Dong, and C. J. Palmstrøm, "Self-assembled ErAs islands in GaAs: Growth and subpicosecond carrier dynamics," *Appl. Phys. Lett.* **75**, p. 3548 (1999)
[65] M. Griebel, J.H. Smet,D.C. Driscoll, J. Kuhl, C.A. Diez, N. Freytag, C. Kadow, A.C: Gossard, and K. von Klitzing, "Tunable subpicosecond optoelectronic transduction in superlattices of selfassembled ErAs nanoislands," *Nature Mat.* **2**, 122 (2003)
[66] R.A. Metzger, A.S. Brown, L.G. McCray, J.A. Henige, "Structural and electrical properties of low temperature GaInAs," *J. Vac. Sci. Technol. B* **11**, p. 798 (1993)
[67] J.L. Hudgins, G.S. Simin, E. Santi, and M.S. Khan, "An Assesment of Wide Bandgap Semiconductors for Power Devices," *IEEE Trans. Power Electron* **18**, 907 (2003).
[68] P. Grenier and J.F. Whitaker, "Subband gap carrier dynamics in low-temperature-grown GaAs," *Appl. Phys. Lett.* **70**, p. 1998 (1997).
[69] H. Erlig, S. Wang, T. Azfar, A. Udupa, H.R. Fetterman, and D.C. Streit, "LT-GaAs detector with 451 fs response at 1.55-micron via two-photon absorption," *Electron. Lett.* **35**, p. 173 (1999).
[70] Y.-J. Chiu, S.Z. Zhang, S.B. Fleischer, J.E. Bowers and U.K. Mishra, "GaAs-based 1.55-μm high speed, high saturation power, low-temperature grown GaAs pin photodetector," *Electron Lett.* **34**, p. 1253 (1998)
[71] J.R. Middendorf, E. R. Brown, "THz pulse generation using extrinsic photoconductivity at 1550 nm," *Optics Express* **20**, p. 16504 (2012).
[72] Z. D. Taylor, E. R. Brown, J. E. Bjarnason, M. P. Hanson, and A. C. Gossard , "Resonant-optical-cavity photoconductive switch with 0.5% conversion efficiency and 1.0W peak power," *Optics Letters* **31**, p. 1729 (2006)
[73] J. Y. Suen, W. Li, Z. D. Taylor, and E.R. Brown, "Characterization and Modeling of a THz Photoconductive Switch," *Appl. Phys. Lett.* **96**, 141103 (2010)
[74] R.A. Metzger, A.S. Brown, L.G. McCray, J.A. Henige, "Structural and electrical properties of low temperature GaInAs," *J. Vac. Sci. Technol. B* **11**, 798 (1993)
[75] D. C. Driscoll, M. Hanson, C. Kadow, and A. C. Gossard, "Electronic structure and conduction in a metal–semiconductor digital composite: ErAs:InGaAs," *Appl. Phys. Lett.* **78**, p. 1703 (2001)
[76] D. C. Driscoll, M. P. Hanson, A. C. Gossard, and E. R. Brown, "Ultrafast photoresponse at 1.55 μm in InGaAs with embedded semimetallic ErAs nanoparticles," *Appl. Phys. Lett.* **86**, 051908 (2005)
[77] M. Sukhotin, E. R. Brown, A. C. Gossard, D. Driscoll, M. Hanson, P. Maker and R. Muller, "Photomixing and photoconductor measurements on ErAs/InGaAs at 1.55 μm ," *Appl. Phys. Lett.* **82**, p. 3116 (2003)
[78] F. Ospald, D. Maryenko, K. von Klitzing, D.C. Driscoll, M.P. Hanson, H. Lu, A.C. Gossard, and J.H. Smet, "1.55 μm ultrafast photoconductive switches based on ErAs:InGaAs," *Appl. Phys. Lett.* **92**, 131117 (2008)
[79] E. R. Brown, D. C. Driscoll, and A. C. Gossard, "State-of-the-art in 1.55 μm ultrafast InGaAs photoconductors, and the use of signal-processing techniques to extract the photocarrier lifetime," *Semicond. Sci. Technol.* **20, p.** 199 (2005)

[80] K.K. Williams, Z. D. Taylor, J. Y. Suen, Hong Lu, R. S. Singh, A. C. Gossard, and E. R. Brown, “Toward a 1550 nm InGaAs photoconductive switch for terahertz generation,” *Optics Lett.* **34**, p. 3068 (2009)
[81] S. Preu, M. Mittendorff, H. Lu, H.B. Weber, S. Winnerl, and A.C. Gossard, “1550 nm ErAs:In(Al)GaAs large area photoconductive emitters,“ *Appl. Phys. Lett.* **101**, 101105 (2012)
[82] B. Sartorius, H. Roehle, H. Künzel, J. Böttcher, M. Schlak, D. Stanze, H. Venghaus, and M. Schell, “All-fiber terahertz time-domain spectrometer operating at 1.5 μm telecom wavelengths,“ *Opt. Express* **16**, p. 9565 (2008)
[83] H. Roehle, R. J. B. Dietz, H. J. Hensel, J. Böttcher, H. Künzel, D. Stanze, M. Schell, and B. Sartorius, “Next generation 1.5 μm terahertz antennas: mesa-structuring of InGaAs/InAlAs photoconductive layers”, *Optics Express* **18**, p. 2296 (2010)
[84] R. J. B. Dietz, B. Globisch, M. Gerhard, A. Velauthapillai, D. Stanze, H. Roehle, M. Koch, T. Göbel, and M. Schell: “64 μW pulsed terahertz emission from growth optimized InGaAs/InAlAs heterostructures with separated photoconductive and trapping regions,“ *Appl. Phys. Lett.* **103**, 061103 (2013)
[85] J. C. Delagnes, P. Mounaix, H. Nemec, L. Fekete, F. Kadlec, P. Kuzel, M. Martin, and J Mangeney, “High photocarrier mobility in ultrafast ion-irradiated $In_{0.53}Ga_{0.47}As$ for terahertz applications,” *J. Phys. D: Appl. Phys*. **42**, 195103 (2009)
[86] C. Carmody, H. H. Tan, C. Jagadish, A. Gaarder, and S. Marcinkevicius, “Ion-implanted In0.53Ga0.47As for ultrafast optoelectronic applications,” *Appl. Phys. Lett.* **82**, p. 3913 (2003)
[87] M. Suzuki and M. Tonouchi, “Fe-implanted InGaAs terahertz emitters for 1.56 m wavelength excitation,” *Appl. Phys. Lett.* **86**, 051104 (2005)
[88] B. C. Tousley, S. M. Mehta, A. I. Lobad, P. J. Rodney, P. M. Fauchet, and P. Cooke, “Femtosecond optical response of low temperature grown $In_{0.53}Ga_{0.47}As$*,” Journal of Electronic Materials* **22**, p. 1477 (2003)
[89] J. Mangeney, „THz photoconductive antennas made from ion-bombarded semiconductors,” *J. Infrared Milli Terahz Waves* **33**, p. 455 (2012)
[90] J. Mangeney, N. Chimot, L. Meignien, N. Zerounian, P. Crozat, K. Blary, J.F. Lampin, P.Mounaix, “Emission characteristics of ion-irradiated $In_{0.53}Ga_{0.47}As$ based photoconductive antennas excited at 1.55 μm,” *Opt. Express* **15**, p. 8943 (2007)
[91] J. Mangeney, P. Crozat , ”Ion-irradiated $In_{0.53}Ga_{0.47}As$ photoconductive antennas for THz generation and detection at 1.55 μm wavelength,” *C. R. Physique* **9,** p. 142 (2008)
[92] C.W. Berry, N. Wang, M.R. Hashemi, M. Unlu, and M. Jarrahi, “Significant performance enhancement in photoconductive terahertz optoelectronics by incorporating plasmonic contact electrodes,” *Nature Commun.* **4**, p. 1622 (2013)
[93] H. Tanoto, J. H. Teng, Q. Y.Wu,M. Sun, Z. N. Chen, S. A. Maier, B. Wang, C. C. Chum, G. Y. Si, A. J. Danner, and S. J. Chua, “Nano-antenna in a photoconductive photomixer for highly efficient continuous wave terahertz emission,” *Scientific Rep.* **3**, p. 2824 (2013)
[94] S.-G. Park,Y. Choi, Y.-J. Oh, and K.-H. Jeong, “Terahertz photoconductive antenna with metal nanoislands,” Opt. Express **20**, p. 25530 (2012)
[95] N. Wang, M. R. Hashemi, and M. Jarrahi, “Plasmonic photoconductive detectors for enhanced terahertz detection sensitivity,” *Opt. Express* **21**, p. 17221 (2013)
[96] J.-W. Shi, Y.-T. Li, C.-L. Pan, M. L. Lin, Y. S. Wu, W. S. Liu and J.-I. Chyi, “Bandwidth enhancement phenomenon of a high-speed GaAs–AlGaAs based unitraveling carrier photodiode with an optimally designed absorption layer at an 830nm wavelength,” *Appl. Phys. Lett.* **89**, 053512 (2006)
[97] H. Ito, S. Kodama, Y. Muramoto, T. Furuta, T. Nagatsuma, *IEEE*, and T. Ishibashi, “High-speed and high-output InP–InGaAs uni-traveling-carrier photodiodes,” *IEEE J. Sel. Top. Quant. Electron.* **10**, p. 709 (2004)

[98] D. Stanze, H. Roehle, R.J.B. Dietz, H.J. Hensel, D. Schmidt, H.-G. Bach, M. Schell, and B. Sartorius, "Improving Photoconductive Receivers for 1.5 μm CW THz Systems," *35th International Conference on Infrared Millimeter and Terahertz Waves (IRMMW-THz) 2010*, 1 (2010)

[99] M. Chtioui, F. Lelarge, A. Enard, F. Pommereau, D. Carpentier, A. Marceaux, F. Van Dijk, and M. Achouche, "High responsivity and high power UTC and MUTC GaInAs-InP photodiodes," *IEEE Photon. Technol. Lett.* **24**, p. 318 (2012).

[100] H. Pan, A. Beling, H. Chen, and J. C. Campbell, "Characterization and optimization of high-power InGaAs/InP photodiodes," *Opt. Quant. Electron.* **40**, p. 41 (2008).

[101] V. Rymanov, A. Stöhr, S. Dülme, and T. Tekin, *"Triple transit region photodiodes (TTR-PDs) providing high millimeter wave output power", Optics Express* **22**, p. 7550 (2014)

[102] Y.-G. Wey, K. Giboney, J. Bowers, M. Rodwell, P. Silvestre, P. Thiagarajan, and G. Robinson, "110-GHz GaInAs/InP double heterostructure p-i-n photodetectors," *J. Lightw. Technol.* **13**, p. 1490 (1995).

[103] D. Pasalic and R. Vahldieck, "Hybrid drift-diffusion-TLM analysis of high-speed and high-output UTC traveling-wave photodetectors," *Int. J. Numer. Model. El.* **21**, p. 61 (2008).

[104] P. S. Menon, K. Kandiah, A. A. Ehsan, and S. Shaari, "Concentration-dependent minority carrier lifetime in an In0.53Ga0.47As interdigitated lateral PIN photodiode model based on spin-on chemical fabrication methodology," *Int. J. Numer. Model. El.* **24**, p. 465 (2011)

[105] K. J. Williams, "Comparisons between dual-depletion-region and uni-travelling-carrier p-i-n photodetectors," *IEE Proc. Optoelectron.* **149**, p. 131 (2002)

[106] V. Rymanov, S. Dülme, S. Babiel, and A. Stöhr, "Compact Photonic Millimeter Wave (200-300 GHz) Transmitters Based On Semicircular Bow-Tie Antenna-Integrated 1.55 μm Triple Transit Region Photodiodes," *German Microwave Conference (GeMiC 2014), Aachen, Germany*, p. 1 (2014)

[107] S Preu, S Malzer, G H Döhler, H Lu, A C Gossard, and L J Wang, "Efficient III–V tunneling diodes with ErAs recombination centers," *Semicond. Sci. Technol.* **25**, 115004 (2010)

[108] S. Preu, F. H. Renner, S. Malzer, G. H. Döhler, L. J.Wang, T. L. J. Wilkinson, E. R. Brown, M. Hanson, and A. C. Gossard, "Efficient Terahertz emission from ballistic transport enhanced n-i-p-n-i-p superlattice photomixers," *Appl. Phys. Lett.* **90**, 212115 (2007)

[109] P. Pohl, F. H. Renner, M. Eckardt, A. Schwanhäußer, A. Friedrich, Ö. Yüksekdag, S. Malzer, G. H. Döhler, P. Kiesel, D. Driscoll, M. Hanson, and A. C. Gossard, "Enhanced recombination tunneling in GaAs pn junctions containing low-temperature-grown-GaAs and ErAs layers," *Appl. Phys. Lett.* **83**, p. 4035 (2003)

[110] Thomas B. Mader, Eric W. Bryerton, Milica Markovi, Michael Forman, and Zoya Popovi, "Switched-mode high-efficiency microwave power amplifiers in a free-space power-combiner array, " *IEEE Trans. Microw. Theory Techniques* **46**, p. 1391 (1998)

[111] M. Micovic, A. Kurdoghlian, A. Margomenos, D.F. Brown, K. Shinohara, S. Burnham, I. Milosavljevic, R. Bowen, A.J. Williams, P. Hashimoto, R. Grabar, C. Butler, A. Schmitz, P.J. Willadsen, and D.H. Chow, "92–96 GHz GaN power amplifiers," *IEEE MTT-S International Microwave Symposium Digest (MTT) 2012*, p.1 (2012)

[112] H. Eisele, "State of the art and future of electronic sources at terahertz frequencies," *Electron. Lett.* **46**, p. 8 (2010)

[113] http://www.dotfive.eu/

[114] B. Heinemann, R. Barth, D. Bolze, J. Drews, G.G. Fischer, A. Fox, O. Fursenko, T. Grabolla, U. Haak, D. Knoll,R. Kurps, M. Lisker, S. Marschmeyer, H. Ru□cker, D. Schmidt, J. Schmidt, M.A. Schubert, B. Tillack, C. Wipf, D. Wolansky, and Y. Yamamoto, "SiGe HBT technology with fT/fmax of 300GHz/500GHz and 2.0 ps CML gate delay," *IEEE International Electron Devices Meeting (IEDM) 2010*, p.30.5.1 (2010)

[115] http://www.dotseven.eu/

[116] V. Jain, E. Lobisser, A. Baraskar, B.J. Thibeault, M. J.W. Rodwell, M. Urteaga, D. Loubychev, A. Snyder, Y. Wu, J.M. Fastenau, and W.K. Liu, "InGaAs/InP DHBTs in a dry-etched refractory metal emitter process demonstrating simultaneous f_{τ}/f_{max}~430/800 GHz," *IEEE Electron. Device Lett.* **32**, p. 24 (2011)
[117] M. Urteaga, R. Pierson, P. Rowell, V. Jain, E. Lobissor, and M. J. W. Rodwell, "130nm InP DHBTs with f_{τ} >0.52THz and f_{max} >1.1THz," *in Proceedings of the 69th IEEE Device Research Conference*, p.281 (2011)
[118] M. J. W. Rodwell: *High-speed Integrated Circuit Technology: Towards 100 GHz Logic.* Singapore: World Scientific Publishing 2001.
[119] Mark Rodwell, E. Lind, Z. Griffith, A. M. Crook, S. R. Bank, U. Singisetti, M. Wistey, G. Burek, and A.C. Gossard, "On the Feasibility of few-THz Bipolar Transistors," *IEEE Bipolar/BiCMOS Circuits and Technology Meeting 2007*, p. 17 (2007)
[120] R. Tsu, and L. Esaki. "Tunneling in a finite superlattice". *Appl. Phys. Lett.* **22**, p. 562 (1973).
[121] L. L. Chang, L. Esaki, and R. Tsu. "Resonant tunneling in semiconductor double barriers". *Appl. Phys. Lett.* **24**, p. 593 (1974).
[122] L. Esaki. "New Phenomenon in Narrow Germanium p-n Junctions". *Phys. Rev.* **109**, p. 603 (1958).
[123] M. Feiginov, H. Kanaya, S. Suzuki, and M. Asada, "Operation of resonant-tunneling diodes with strong back injection from the collector at frequencies up to 1.46 THz," *Appl. Phys. Lett.* **104**, p. 243509 (2014)
[124] H. Kanaya, R. Sogabe, T. Maekawa, S. Suzuki, and M. Asada. "Fundamental Oscillation up to 1.42 THz in Resonant Tunneling Diodes by Optimized Collector Spacer Thickness". *J. Infrared Milli. Terahz. Waves* **35**, p. 425 (2014).
[125] M. Feiginov, C. Sydlo, O. Cojocari, and P. Meissner. "Resonant-tunnelling-diode oscillators operating at frequencies above 1.1 THz". *Appl. Phys. Lett.* **99**, 233506 (2011).
[126] E. Schomburg, M. Henini, J. M. Chamberlain, D. P. Steenson, S. Brandl, K. Hofbeck, K. F. Renk. and W. Wegscheider. "Self-sustained current oscillation above 100 GHz in a GaAs/AlAs superlattice," *Appl. Phys. Lett.* **74**, 2179 (1999).
[127] L. Britnell, R. V. Gorbachev, A. K. Geim, L. A. Ponomarenko, A. Mishchenko, M. T. Greenaway, T. M. Fromhold, K. S. Novoselov, and L. Eaves. "Resonant tunnelling and negative differential conductance in graphene transistors," *Nature Comm.* **4**, 1794 (2013).
[128] M. Feiginov and I. N. Kotelnikov. "Evidence for attainability of negative differential conductance in tunnel Schottky structures with two-dimensional channels," *Appl. Phys. Lett.* **91**, 083510 (2007).
[129] A. Maestrini, B. Thomas, H. Wang, C. Jung, J. Treuttel, Y. Jin, G. Chattopadhyay, I. Mehdi, G. Beaudin, "Schottky diode based terahertz frequency multipliers and mixers," *Comptes Rendus Physique* **11**, pp. 480 (2010)
[130] Th.W. Crowe, "GaAs Schottky barrier diodes for the frequency range 1-10 THz," *Int. J. Infrared and Millimeter Waves* **10**, 765 (1989)
[131] L. Kollberg and A. Rydberg, "Quantum-barrier-varactor diode for high efficiency millimeter-wave multipliers", *IEEE Electronic Letters* **25**, p. 1696 (1989)
[132] L. Dillner, M. Ingvarson, E. Kollberg, J. Stake "High Efficiency HBV multipliers for millimeter wave generation, Terahertz Sources and Systems," *NATO Science Series* **27**, p. 27 (2001)
[133] A. V. Raisanen, "Frequency multiplier for millimeter and sub millimeter wavelengths", *Proc. IEEE* **80**, p. 1842 (1992)
[134] D. Poterfield, J. Hesler ; C. Thomas ; B. William and D. Woolard, "Integrated Terahertz Transmit/Receive Modules", *European Microwave Conference, Munich, Germany 2003*, p. 1319 (2003)

[135] A. Malko, T. Bryllert, J. Vukusic, "Silicon Integrated InGaAs/InAlAs/AlAs HBV Frequency Tripler," *IEEE Electron Device Letters* **34**, p. 843 (2013).
[136] M. Schumann, K. Duwe, C. Domoto, A. Megej, M. Rodriguez-Girones, J. Muller, R. Judaschke, and H. Hartnagel, "High-performance 450-GHz GaAs-based heterostructure barrier varactor tripler," *IEEE Electron Device Letters* **24**, p. 138 (2003)
[137] M.T. Faber, J. Chramiec, and M. E. Adamski, *Microwave and Millimeter-wave Diode Frequency Multipliers*, Norwood, MA: Artech House, 1995.
[138] S. A. Maier, *Plasmonics: Fundamentals and Applications*. New York: Springer, 2007.
[139] E. Ozbay, "Plasmonics: merging photonics and electronics at nanoscale dimensions.," *Science* **311**,pp. 189 (2006)
[140] M. Dragoman and D. Dragoman, "Plasmonics: Applications to nanoscale terahertz and optical devices," *Prog. Quantum Electron.* **32**, p. 1 (2008)
[141] A. Ishimaru, *Electromagnetic Wave Propagation, Radiation, and Scattering*. Englewood Cliffs, New Jersey: Prentice Hall, Inc., 1991.
[142] J. Zenneck, "Über die Fortpflanzung ebener elektromagnetischer Wellen längs einer ebenen Leiterfläche und ihre Beziehung zur drahtlosen Telegraphie," *Ann. Phys.* **328**, p. 846 (1907)
[143] Editorial, "Surface Plasmon Resurrection," *Nat. Photonics* **6**, p. 707 (2012)
[144] T. W. Ebbesen, H. J. Lezec, H. F. Ghaemi, T. Thio, and P. A. Wolff, "Extraordinary optical transmission through sub-wavelength hole arrays," *Nature* **391**, p. 667 (1998)
[145] H. J. Lezec, A. Degiron, E. Devaux, R. A. Linke, L. Martin-Moreno, F. J. Garcia-Vidal, and T. W. Ebbesen, "Beaming light from a subwavelength aperture.," *Science* **297**, p. 820 (2002)
[146] M. Beruete, M. Sorolla, I. Campillo, J. S. Dolado, L. Martín-Moreno, J. Bravo-Abad, and F. J. García-Vidal, "Enhanced millimeter-wave transmission through subwavelength hole arrays," *Opt. Lett.* **29**, p. 2500 (2004)
[147] M. Beruete, I. Campillo, J. S. Dolado, J. E. Rodríguez-Seco, E. Perea, and M. Sorolla, "Enhanced microwave transmission and beaming using a subwavelength slot in corrugated plate," *IEEE Antennas Wirel. Propag. Lett*. **3**, p. 328 (2004)
[148] J. B. Pendry, L. Martín-Moreno, and F. J. Garcia-Vidal, "Mimicking surface plasmons with structured surfaces.," *Science* **305**, p. 847 (2004)
[149] V. Lomakin and E. Michielssen, "Enhanced transmission through metallic plates perforated by arrays of subwavelength holes and sandwiched between dielectric slabs," *Phys. Rev. B*, **71**, p. 235117 (2005)
[150] V. Torres, R. Ortuño, P. Rodríguez-Ulibarri, A. Griol, A. Martínez, M. Navarro-Cía, M. Beruete, and M. Sorolla, "Mid-infrared plasmonic inductors: Enhancing inductance with meandering lines.," *Sci. Rep.* **4**, p. 1 (2014)
[151] D. R. Jackson, A. A. Oliner, T. Zhao, and J. T. Williams, "Beaming of light at broadside through a subwavelength hole: Leaky wave model and open stopband effect," *Radio Sci.* **40**, p. 1 (2005)
[152] W. Zheng, H. C. Chiamori, G. L. Liu, L. Lin, and F. F. Chen, "Nanofabricated plasmonic nano-bio hybrid structures in biomedical detection," *Nanotechnol. Rev.* **1**, p. 213 (2012)
[153] J. R. Lakowicz and Y. Fu, "Modification of single molecule fluorescence near metallic nanostructures," *Laser Photon. Rev.* **3**, p. 221 (2009)
[154] G. Baffou and R. Quidant, "Thermo-plasmonics: using metallic nanostructures as nano-sources of heat," *Laser Photon. Rev.* **7**, p. 171 (2013)
[155] H. Aouani, M. Rahmani, M. Navarro-Cía, and S. a. Maier, "Third-harmonic-upconversion enhancement from a single semiconductor nanoparticle coupled to a plasmonic antenna.," *Nat. Nanotechnol.* **9**, p. 290 (2014)
[156] G. Ramakrishnan, N. Kumar, P. C. M. Planken, D. Tanaka, and K. Kajikawa, "Surface plasmon-enhanced terahertz emission from a hemicyanine self-assembled monolayer," *Opt. Express* **20**, p. 4067 (2012)

[157] D. K. Polyushkin, I. Márton, P. Rácz, P. Dombi, E. Hendry, and W. L. Barnes, “Mechanisms of THz generation from silver nanoparticle and nanohole arrays illuminated by 100 fs pulses of infrared light,” *Phys. Rev. B* **89**, p. 125426 (2014)
[158] K. H. Yang, P. L. Richards, and Y. R. Shen, “Generation of Far-Infrared Radiation by Picosecond Light Pulses in LiNbO3,” *Appl. Phys. Lett.*, **19**, p. 320 (1971)
[159] D. Auston, K. Cheung, J. Valdmanis, and D. Kleinman, “Cherenkov Radiation from Femtosecond Optical Pulses in Electro-Optic Media,” *Phys. Rev. Lett.* **53**, p. 1555 (1984)
[160] X.-C. Zhang, B. B. Hu, J. T. Darrow, and D. H. Auston, “Generation of femtosecond electromagnetic pulses from semiconductor surfaces,” *Appl. Phys. Lett.* **56**, p. 1011 (1990)
[161] X.-C. Zhang, Y. Jin, and X. F. Ma, “Coherent measurement of THz optical rectification from electro-optic crystals,” *Appl. Phys. Lett.* **61**, p. 2764 (1992)
[162] A. Rice, Y. Jin, X. F. Ma, X.-C. Zhang, D. Bliss, J. Larkin, and M. Alexander, “Terahertz optical rectification from ⟨110⟩ zinc-blende crystals,” *Appl. Phys. Lett.* **64**, p. 1324 (1994)
[163] C. Vicario, C. Ruchert, and C. P. P. Hauri, “High field broadband THz generation in organic materials,” *J. Mod. Opt.* **39**, p. 2660 (2013)
[164] F. Kadlec, P. Kuzel, and J.-L. Coutaz, “Optical rectification at metal surfaces.,” *Opt. Lett.* **29**, p. 2674 (2004)
[165] F. Kadlec, P. Kuzel, and J.-L. Coutaz, “Study of terahertz radiation generated by optical rectification on thin gold films.,” *Opt. Lett.* **30**, p. 1402 (2005)
[166] G. Welsh, N. Hunt, and K. Wynne, “Terahertz-Pulse Emission Through Laser Excitation of Surface Plasmons in a Metal Grating,” *Phys. Rev. Lett.* **98**, p. 026803 (2007)
[167] G. H. Welsh and K. Wynne, “Generation of ultrafast terahertz radiation pulses on metallic nanostructured surfaces.,” *Opt. Express* **17**, p. 2470 (2009)
[168] M. Aeschlimann, C. A. Schmuttenmaer, H. E. Elsayed-Ali, R. J. D. Miller, J. Cao, Y. Gao, and D. A. Mantell, “Observation of surface enhanced multiphoton photoemission from metal surfaces in the short pulse limit,” *J. Chem. Phys.* **102**, p. 8606 (1995)
[169] Y. Gao, M.-K. Chen, C.-E. Yang, Y.-C. Chang, S. Yin, R. Hui, P. Ruffin, C. Brantley, E. Edwards, and C. Luo, “Analysis of terahertz generation via nanostructure enhanced plasmonic excitations,” *J. Appl. Phys.* **106**, p. 074302 (2009)
[170] D. K. Polyushkin, E. Hendry, E. K. Stone, and W. L. Barnes, “THz generation from plasmonic nanoparticle arrays.,” *Nano Lett.* **11**, p. 4718 (2011)
[171] G. Ramakrishnan and P. C. M. Planken, “Percolation-enhanced generation of terahertz pulses by optical rectification on ultrathin gold films.,” *Opt. Lett.* **36**, p. 2572(2011)
[172] L. Luo, I. Chatzakis, J. Wang, F. B. P. Niesler, M. Wegener, T. Koschny, and C. M. Soukoulis, “Broadband terahertz generation from metamaterials.,” *Nat. Commun.* **5**, p. 3055, (2014)
[173] R. Marqués, J. D. Baena, M. Beruete, F. Falcone, T. Lopetegi, M. Sorolla, F. Martín, and J. García-García, “Ab initio analysis of frequency selective surfaces based on conventional and complementary split ring resonators,” *J. Opt. A Pure Appl. Opt.* **7**, p. 38 (2005)
[174] J. Faist, F. Capasso, D. L. Sivco, C. Sirtori, A. L. Hutchinson, and A. Y. Cho, “Quantum cascade laser.,” *Science* **264**, p. 553 (1994)
[175] F. Kazarinov and R. A. Suris, “Possibility of the amplification of electromagnetic waves in a semiconductor with a superlattice,” *Sov. Phys. - Semicond.* **5**, p. 707 (1971)
[176] R. Köhler, A. Tredicucci, F. Beltram, H. E. Beere, E. H. Linfield, A. G. Davies, D. A. Ritchie, R. C. Iotti, and F. Rossi, “Terahertz semiconductor-heterostructure laser.,” *Nature* **417**, p. 156 (2002)
[177] S. Kumar, “Recent progress in terahertz quantum cascade lasers,” *IEEE J. Sel. Top. Quantum Electron.* **17**, p. 38 (2011)

[178] O. Mitrofanov, R. James, F. A. Fernandez, T. K. Mavrogordatos, and J. A. Harrington, “Reducing Transmission Losses in Hollow THz Waveguides,” *IEEE Trans. Terahertz Sci. Technol.* **1**, p. 124 (2011)
[179] L. Mahler, R. Ko□hler, A. Tredicucci, F. Beltram, H. E. Beere, E. H. Linfield, D. a. Ritchie, and a. G. Davies, “Single-mode operation of terahertz quantum cascade lasers with distributed feedback resonators,” *Appl. Phys. Lett.* **84**, p. 5446 (2004)
[180] B. Williams, S. Kumar, Q. Hu, and J. Reno, “Distributed-feedback terahertz quantum-cascade lasers with laterally corrugated metal waveguides,” *Opt. Lett.* **30**, p. 2909 (2005)
[181] L. Mahler, A. Tredicucci, R. Ko□hler, F. Beltram, H. E. Beere, E. H. Linfield, and D. a. Ritchie, “High-performance operation of single-mode terahertz quantum cascade lasers with metallic gratings,” *Appl. Phys. Lett.* **87**, p. 181101 (2005)
[182] O. Demichel, L. Mahler, and T. Losco, “Surface plasmon photonic structures in terahertz quantum cascade lasers,” *Opt. Express* **14**, p. 5335 (2006)
[183] H. Tanvir, B. M. A. Rahman, N. Kejalakshmy, A. Agrawal, and K. T. V Grattan, “Evolution of Highly Confined Surface Plasmon Modes in Terahertz Quantum Cascade Laser Waveguides,” *J. Light. Technol.* **29**, p. 2116 (2011)
[184] N. Yu, J. Fan, Q. J. Wang, C. Pflügl, L. Diehl, T. Edamura, M. Yamanishi, H. Kan, and F. Capasso, “Small-divergence semiconductor lasers by plasmonic collimation,” *Nat. Photonics* **2**, p. 564 (2008)
[185] M. Díaz and I. Campillo, “Dual-band low-profile corrugated feeder antenna,” *IEEE Trans Antennas and Progag.* **54**, p. 340 (2006)
[186] M. Beruete, I. Campillo, J. S. Dolado, J. E. Rodriguez-Seco, E. Perea, F. Falcone, and M. Sorolla, “Very Low-Profile ‘Bull’s Eye’ Feeder Antenna,” *Antennas Wirel. Propag. Lett.* **4**,p. 365 (2005)
[187] M. Beruete, U. Beaskoetxea, M. Zehar, A. Agrawal, S. Liu, K. Blary, A. Chahadih, X.-L. Han, M. Navarro-Cia, D. Etayo Salinas, A. Nahata, T. Akalin, and M. Sorolla Ayza, “Terahertz Corrugated and Bull’s-Eye Antennas,” *IEEE Trans. Terahertz Sci. Technol.* **3**, p. 740 (2013)
[188] N. Yu, Q. J. Wang, M. a Kats, J. a Fan, S. P. Khanna, L. Li, a G. Davies, E. H. Linfield, and F. Capasso, “Designer spoof surface plasmon structures collimate terahertz laser beams.,” *Nat. Mater.* **9**, p. 730 (2010)